IRIDIUM OXIDE SUPPORTED ON GRAPHITIZED CARBON FOR USE AS REVERSAL TOLERANT ANODES IN PEM FUEL CELLS

Prepared by:

Tita N. Labi

Dissertation submitted in fulfilment of the University of Cape Town

in partial fulfilment of the requirements

for the degree of

Master of Science in Chemical Engineering

Hydrogen South Africa (HySA)

Catalysis Institute

Department of Chemical Engineering

University of Cape Town

October 2019

Synopsis

One way in which potential reversal occurs in Proton Exchange Membrane Fuel Cells (PEMFCs) is when the H_2 supply is insufficient to meet the load requirements of the cell. During cell voltage reversal, carbon oxidation and water electrolysis occur at the anode to maintain the supply of protons and electrons to the cathode. These reactions are non-spontaneous and consume energy from the membrane electrode assembly (MEA), causing irreversible damage through carbon corrosion. A material-based approach to prevent or reduce damage to the anode during cell reversal is to include an oxygen evolution reaction (OER) catalyst which will decrease the overpotential for water electrolysis. The addition of the OER catalyst to generate a reversal tolerant anode (RTA) will therefore decrease the occurrence of the carbon corrosion at cell potentials below -1.2 V.

Due to the harsh conditions of fuel cell operation, the OER catalyst needs to provide both high activity and durability. Studies have shown that among the noble metal electrocatalysts, iridium (Ir) in its oxide form is among the highest for OER activity in acidic media. McCrory et al., (2013) also found that of all their tested metal oxide systems, IrO_x was the most stable in acidic solutions. IrO_x is an efficient catalyst for the OER but the use of pure IrO_x is limited due to high costs and low surface area in its crystalline form. Several studies have therefore focused on supporting the IrO_x on various materials to increase surface area and stability. Ideal catalyst supports used in electrochemical cells need to have a porous nanostructure and high electronic conductivity for electron transfer through the external circuit.

Carbon remains the preferred commercial support due to its low costs, however, it undergoes corrosion under certain conditions during operation. Graphitized carbon supports have been gaining more attention due to their corrosion resistance and superior electrical conductivity.

The aim of this study is therefore to use graphitized carbon supported iridium oxide to generate reversal tolerant anodes in an MEA.

The IrO_x supported graphitized carbon catalyst was synthesized using a microwave assisted polyol deposition technique. The supported catalyst was characterized using XRD, TEM, TGA, XPS and EDX analysis. The nanoparticles were well dispersed over the graphitised support and in the range of 4-10 nm. XPS analysis showed that the main oxidation states of Iridium were Ir^{3+} and Ir^{4+} which are proven to be the main states responsible for the OER. After comparison

with commercial catalysts, it was found to have a good balance between activity and durability having an activity of 0.141 A/mg Ir towards the OER.

The supported IrO_x was included in the anode of an MEA at two different loadings (0.1 mg Ir /cm^2 (1:1 Pt/Ir) and 0.06 mg Ir/cm^2 (1:0.06 Pt/Ir)). The results showed that the addition of the OER did not compromise the performance of the MEA under normal operating conditions. Furthermore, the MEAs generated proved reversal tolerant capabilities by withstanding multiple, prolonged periods of fuel starvation by maintaining the cell potential in the water electrolysis potential range. The effects of fuel starvation were found to increase the ohmic resistance of the cell, possibly due to membrane dehydration and ionomer degradation. After testing, the MEAs were also characterised using XPS, SEM, cyclic voltammetry to determine the physical changes that occur during these events.

Acknowledgements

First and foremost, I would like to express my gratitude to the Catalysis department and HySA for granting me the opportunity to undertake my masters project in such a highly relevant field as fuel cell technology.

I would like to especially thank my supervisors, Dr. Jessica Chamier and François Van Schalkwyk, for their guidance and creating an environment conducive for growth and development. This project would also not have been possible without the support of the technical development team – Firdaus Hendricks, Joe Itota, Ursyla Nyambi and Bettina Kaine.

Thank you to Mohamed Jaffer, Miranda Waldron and Nasheeta Hanief in the Electron Microscopy unit for their assistance and proficiency in analysing my countless samples.

I would also like to extend my appreciation to our collaborators Prof. Shuang Ma Andersen in Southern Denmark University and Prof. Ray Sekhar at UNISA, for XPS analysis, as well as Darija Susac for her expertise in analysing the XPS data.

Finally, I would like to thank my friends and family for their continued support and encouragement, with whom this project would not have been possible.

Plagiarism Declaration

I hereby declare that I am fully aware of the meaning of plagiarism and that all work in this document, except for that which has been acknowledged, is my own. This thesis has also been submitted to the Turnitin module (or equivalent similarity and originality checking software) and I confirm that my supervisor has seen the report and any concerns revealed have been resolved.

Signed by candidate

Tita N. Labi

Electronically signed

1st October 2019

Table of Contents

List of Figures

List of Tables

Nomenclature and Abbreviations

The following is a list of symbols and abbreviations that are present in the document

Symbol	Description
%	Percentage
°C	Degrees Celsius
A	Active Area
BET	Brunauer-Emmett-Teller
BoL	Beginning of Life
CCM	Catalyst coated membrane
D.L.	Double Layer Capacitance
D_{O_2}	Oxygen diffusion coefficient
ECSA	Electrochemical Active Surface Area
EDX	Energy Dispersive X-ray Spectroscopy
EIS	Electrochemical Impedance Spectroscopy
EoL	End of Life
F	Faraday's constant
g	grams
GDL	Gas diffusion layer
GV	Graphitized Vulcan
HOR	Hydrogen Oxidation Reaction
H_s	Strongly adsorbed Hydrogen
H_w	Weakly adsorbed Hydrogen
H_{upd}	Hydrogen Underpotential Deposition
I_{lim}	Limiting current density
I	Current
IrO_x	Iridium Oxide
J_{O_2}	Oxygen permeation rate
C_{O_2}	Oxygen concentrations
MEA	Membrane Electrode Assembly
mm	Millimetre

nm	Nanometre
N	Molar flow of hydrogen
OER	Oxygen Evolution Reaction
ORR	Oxygen Reduction Reaction
OCV	Open-Circuit Voltage
O_{upd}	Oxygen Underpotential Deposition
PEMFC	Polymer Electrolyte Membrane Fuel cell
PTFE	Polytetrafluoroethylene
RH	Relative humidity
RTA	Reversal Tolerant Anode
SEM	Scanning Electron Microscopy
TEM	Transmission Electron Microscopy
XRD	X-Ray Diffraction
XPS	X-ray Photoelectric Spectroscopy
z	Membrane thickness

1. Introduction

1.1. Background

As the effects of climate change become more apparent due to our heavy dependence on fossil fuels, the need to find more efficient and environmentally friendly means of energy generation is becoming more imperative. Currently, our efforts are focused at optimizing current processes to reduce emission as well as developing new technologies to replace our fossil fuel dependence and meet the ever-growing energy demands. Several alternative technologies such as solar power, wind turbines and tidal energy are being researched and developed for stationary energy generation while others such as biofuels, batteries and hydrogen energy also provide mobile energy production. All these technologies have their respective advantages and disadvantages based on factors such as geography, cost and environmental conditions, and therefore to have a society completely independent of fossil fuels, not just one but a combination of these methods will be necessary.

Fuel cells are one of the technologies which is gaining headway in tackling this issue for both mobile and stationary energy applications. Fuel cells and batteries both work through chemical reactions, however, they differ in that batteries store energy generated from an external source. Batteries therefore need to be recharged while fuel cells generate electrical energy by converting an external fuel source (Sedighizadeh and Rezazadeh, 2007). Therefore, fuel cells have huge potential for use in remote areas where access to conventional power grids is unavailable. Most fuel cells only use oxygen and a fuel source for operations. The fuel source can be for example hydrogen or methanol obtained from an electrolysis or biomass process respectively.

Currently there are several types of fuel cells but the polymer electrolyte membrane fuel cell (PEMFC) offers high power density with lower weight and volume compared to the other fuel cell types (US Department of Energy., n.d.). These PEMFCs convert chemical potential energy in hydrogen and oxygen directly into electrical energy, water and heat. The two main reactions that take place in the PEM fuel cell are the hydrogen oxidation reaction (HOR), which splits hydrogen molecules into protons and electrons, and the oxygen reduction reaction (ORR) which combines oxygen, protons and electrons to form water (Qin *et al.*, 2016). These reactions occur at the anode and cathode respectively. As the only by-product

is water, they already have a huge advantage over coal power station, nuclear power plants and internal combustion engines, all of which produce harmful substances as by-products.

In addition to reduced emissions, fuel cells have no moving parts and therefore avoid the conversion of chemical potential energy into mechanical energy thereby making them inherently more efficient than traditional combustion engines since they are not limited by the Carnot cycle.

1.2. Context

Despite its huge potential for cleaner energy generation, fuel cell technology still has several hurdles to cross regarding its durability and cost which limit widespread commercialization. The chart below shows the current status of fuel cell system development across critical system specifications as well as targets set by the US DOE to realise commercialization of automotive fuel cell systems.

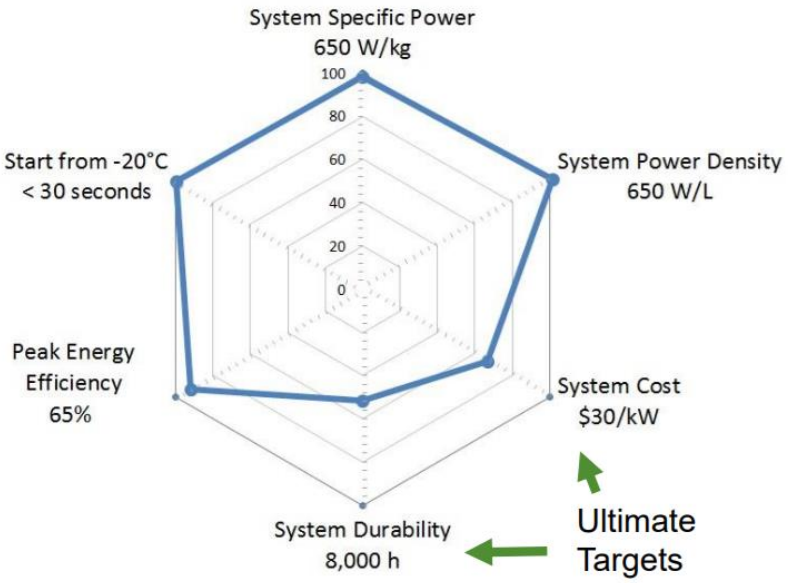

Figure 1 - Fuel cell targets by US Department of Energy (2019).

One of the durability challenges is a phenomenon called potential reversal which causes fast and irreversible damage to the catalyst layers when there is a disruption in the fuel supply or when the load being drawn from the cell changes rapidly. Damage to the catalyst layer causes a reduction in performance and the only way to undo said degradation is to replace the entire catalyst containing membrane electrode assembly (MEA).

During potential reversal, two main reactions take place; carbon oxidation and water oxidation (or oxygen evolution reaction (OER)). Conventional catalyst layers are supported on carbon, carbon oxidation therefore has detrimental effects on PEMFC durability. A material-based mitigation strategy is to add a catalyst that selectively promotes the OER over carbon oxidation. Iridium oxide (IrO_x) has been found to be the best catalyst for this reaction which will then maintain the integrity of the catalyst layer during potential reversal.

To reduce costs and increase surface area, IrO_x can be supported. Carbon blacks remain the ideal support due to their low costs, however, they undergo corrosion under certain conditions during operation. Graphitized carbon supports have been gaining more attention due to its increased corrosion resistance and superior electrical conductivity (Sadhasivam *et al.*, 2016). Although it has the ideal properties for electrochemical uses, no studies have been conducted using graphitized carbon as a support material for OER catalyst to generate RTA in a membrane electrode assembly (MEA).

1.3. Scope

To increase the durability of MEA during potential reversal, a reversal tolerant anode was developed. The project made graphited Vulcan supported IrO_2 using microwave assisted polyol deposition. Thereafter, the synthesized catalyst was evaluated ex-situ via electrochemical analysis to determine its activity towards the OER and durability. The catalyst was then sprayed onto the MEA and analysed in-situ. This was done on a FuelCon Elevator-C test station to assess its performance during normal operation as well as after multiple potential reversal events.

1.4. Aim of project

The aim of this thesis is to make an MEA which can withstand periods of fuel starvation while maintaining benchmark performance. Herein the durability of fuel cells for both mobile and stationary applications can be significantly increased. To achieve the aim the following objectives are set:

1. Synthesis of an IrO_x OER catalyst supported on graphitized carbon,

2. Determining the performance and durability of the supported catalyst using ex situ electrochemical analysis,
3. Design and manufacture an MEA with an anode including the synthesised supported catalyst,
4. Determine the tolerance of the designed MEA during cell reversal conditions, and their ability to maintain benchmark performance.

1.5. Hypothesis

It is hypothesized that using graphitized carbon as a support of IrO_x will increase the durability of the catalyst due to its resistance to corrosion and will enhance the activity of the OER due to its high surface area. Furthermore, the introduction of the graphitized Vulcan (GV) supported iridium oxide (IrO_x/GV) OER catalyst to the anode layer of an MEA should not greatly affect the normal operation of the MEA, as it will only become active once the cell potential is reversed during fuel starvation. The designed MEA should therefore mitigate the effects of potential reversal due to the inclusion of the OER catalyst which promotes water oxidation thereby reducing carbon oxidation.

1.6. Key questions

The following key questions will be addressed during this research project.

1. What is the performance and durability of the IrO_2/GV catalyst to the OER?
2. How does the inclusion of the OER catalyst in the anode affect the performance of the MEA under normal operating conditions?
3. How long does the OER layer prevent potential reversal before failure in PEMFC?
4. What is the loss of performance after successive fuel starvation events?

1.7. Thesis outline

Chapter 1 introduces the concepts, reasons and importance for undertaking this project as well as defines the scope and question which aim to be answered by the end of the document.

Chapter 2 details the relevant literature on the problem statement which will then be used to support the decisions made for this project. Chapter 3 presents the experimental methodology and analytical techniques used. The methodology required for analysis is also detailed. The three chapters following this (Chapters 4,5 & 6) will provide the results for the synthesis method, ex situ electrochemical analysis and MEA testing respectively. The final chapter summarises and highlights some results and makes recommendations for future work.

1.8. Research Outputs

Sections of this work has been presented at refereed international conferences and will be submitted to peer review journals.

Conference oral and poster presentations:

1. T. Labi, J. Chamier, F. Van Schalkwyk "Synthesis of carbon supported IrOx catalyst for the oxygen evolution reaction", Catalysis South Africa, Limpopo 2018
2. T. Labi, J. Chamier, F. Van Schalkwyk "Iridium oxide supported on graphitized carbon for use as reversal tolerant anodes in PEM fuel cells", International Society of Electrochemistry, South Africa, Durban 2019

2. Literature Review

Chapter 2 presents a background on Polymer Exchange Membrane (PEM) fuel cells followed by a brief discussion on the various challenges faced in PEM fuel cell technology. A detailed description of cell potential reversal and the associated mitigation strategies currently implemented is presented. Finally, this chapter concludes with the discussion on stress tests which will be used to simulate cell potential reversal and the characterization tools used to analyse the MEAs performance during these events.

2.1. Polymer Electrolyte Membrane Fuel Cells (PEMFCs)

The first known concept for fuel cells was developed by mixing hydrogen and oxygen in an electrolyte to generate electricity and water by Sir William Robert Grove in 1839 (Appleby, 1990). The term "fuel cell" was later coined by Ludwig Mond and Charles Langer who successfully built a practical device from Grove's theory that run on air and industrial coal gas (Bellis, 2019).

From the time when fuel cells were invented, there have been several variations that have been developed, each having their respective advantages and disadvantages. All variations of the fuel cell still employ the same core electrochemical principles but have different fuel requirements, operating temperature ranges and types of catalyst used. They are named according to a specific component used (e.g. type of electrolyte or membrane) or the fuel requirement.

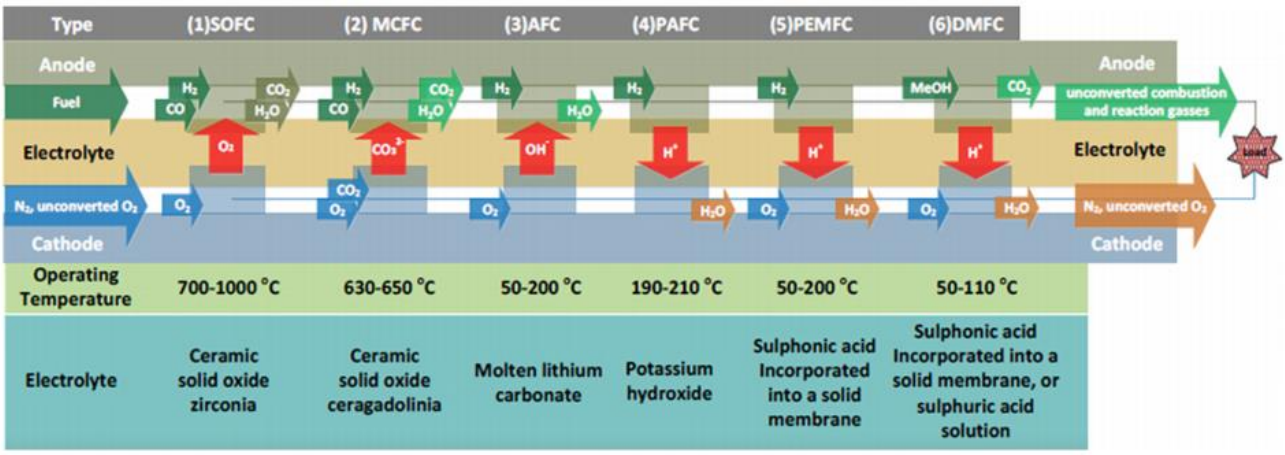

Figure 2 - Comparison of the six types of fuel cells (Vaghari et al., 2013).

Figure 2 above shows the six common types of fuel cells which include:

- Alkaline Fuel Cell (AFC)
- Molten Carbonate Fuel Cell (MCFC)
- Solid Oxide fuel Cell (SOFC)
- Phosphoric Acid Fuel Cell (POFC)
- Polymer Electrolyte Membrane Fuel Cell (PEMFC)
- Direct Methanol Fuel Cell (DMFC)

This project investigates activities associated with low temperature PEMFCs (hereafter, all mention of fuel cells in this document refer to PEMFCs). PEMFCs have higher energy conversion efficiency, higher-energy density and zero emissions. In addition to these, its relatively low temperatures also allow for quick start-ups and suitability for discontinuous operation (Wee, 2007). Using a polymer electrolyte membrane also solves some of the drawbacks related to other fuel cells with liquid electrolytes (e.g. AFC) such as the absolute need for pure fuels (Vaghari *et al.*, 2013). Moreover, they can be made light-weight and therefore the leading fuel cell technology for handling technologies (e.g. forklifts) and transportation (e.g. cars, trains etc.).

2.2. Membrane Electrode Assemblies (MEAs)

A fuel cell stack consists of multiple MEAs, where the output of the fuel cell is the combined individual output of the MEAs. The MEA is the core component of the fuel cell and is typically made up of a polymer electrolyte membrane, two catalyst layers (electrodes), a gas diffusion layer and a microporous layer as can be seen in Figure 3.

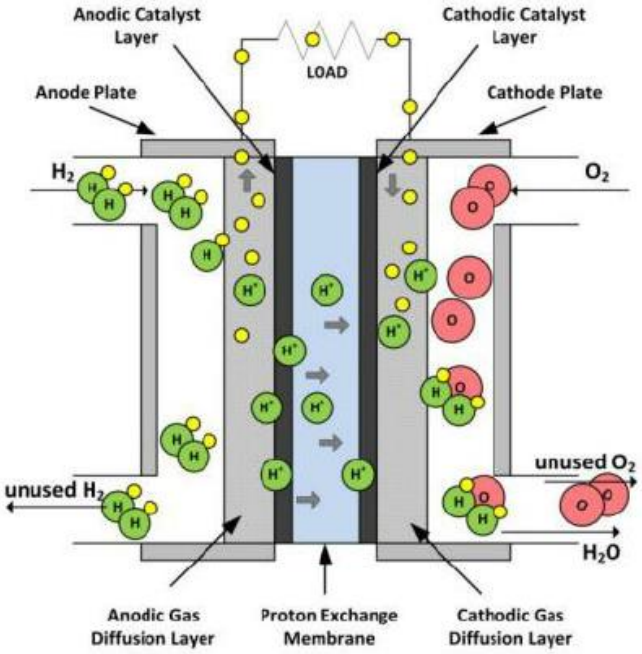

Figure 3 - Schematic diagram of a single MEA in PEM fuel cell (Abaspour, Tadrisi Parsa and Sadeghi, 2014).

The polymer electrolyte membrane is responsible for gas separation, proton conduction and charge separation whereas the gas diffusion layer and microporous layer regulate gas distribution and water transport. The two electrodes; cathode and anode, are responsible for the reduction and oxidation respectively of the reactants to facilitate the electrochemical reaction (Kunusch, Puleston and Mayosky, 2012).

Single cell MEAs are currently performing at approximately 0.8 V and a current density (i) of 1 A/cm^2, which on its own, is not sufficient for real world applications, as the requirements for fuel cell vehicles for example is above 30 kW (Herrmann and Rothfuss, 2015). By connecting several MEAs in a fuel cell stack the power can be modified to fit any possible use. This can be achieved by changing the number of single cells in the stack and the active area of each cell. For example, a stack with 100 cells (n) and an active area (A) of 100 cm^2 will have a power output of:

$$P = UI = n \cdot u \cdot A \cdot i = 100 \times 0.8 \times 100 \times 1 = 8\ kW$$

2.3. Components of an MEA

2.3.1. Membrane layer

The membrane is at the centre of an MEA and is essential as it separates the two reactions that occur on either side. The proton exchange membrane allows for protons generated at the anode to be transferred to the cathode. PEMFC membranes must maintain certain properties such as high proton conductivity, low permeability to fuel gas or liquid, zero electronic conductivity, good mechanical toughness and high resistance to the oxidative and hydrolytic conditions of the fuel cell (Vaghari *et al.*, 2013). The membrane serves to complete the circuit by selectively allowing protons through and repelling electrons forcing them through an external circuit. The membrane material is typically based on the polymer, perfluoro sulfonated acid (PFSA) (Longo *et al.*, 2017).

2.3.2. Electrode layers

The electrodes (catalyst layers) are where the chemical reactions of the fuel cell take place and usually the most expensive part of the MEA. These layers are generally very thin (about 10 – 15 μm) and consist of three phases:

- a supported metal catalyst (usually Pt on carbon) to promote the respective reactions and enhance conduction,
- an ionomer for proton conduction and
- void space for reactant and gas transport (Longo *et al.*, 2017).

The two reactions that occur are the hydrogen oxidation reaction (HOR) and the oxygen reduction reaction (ORR) and take place at the anode and cathode respectively as presented by Equation 2.1 and 2.2.

Anode: $$H_2 \rightarrow 2H^+ + 2e^-$$ (*Eq. 2.1*)

Cathode: $$O_2 + 4H^+ + 4e^- \rightarrow 2H_2O$$ (*Eq. 2.2*)

These reactions occur at a triple phase boundary where electrons, protons and reactant gases meet. To maximize this interface, the effective area of the active catalyst must be several times larger than the geometric area of the electrode (Spiegel *et al.*, 2007).

The ionomer in PEMFCs is responsible for the transport of protons from the anode to the cathode through the catalyst layers and membrane. Nafion® was one of the first perfluorosulfonic acid ionomers (PFSA) and is still very commonly used in PEMFCs. For good performance, the ionomer must cover all platinum particles to maximize catalyst utilization, be thin enough not to hinder effective gas transport (Park *et al.*, 2015), and must also be well hydrated to allow for easy proton conductivity.

The PFSA ionomers have a polytetrafluoroethylene (PTFE) backbone with sulfonic groups attached to a side chain and recently, there have been studies that showed that short-side-chain (SSC) ionomers such as Aquivion® exhibit better performance than Nafion®, which is referred to as a long-side-chain (LSC) ionomer (Siracusano *et al.*, 2014).

2.3.3. Gas diffusion layer (GDL)

The GDL lies in between the catalyst layers and the bipolar plates (or flow-field plates). They performs several important functions in the fuel cell such as transport and distribution of the reactants and products, heat conduction, electron conduction as well as provides mechanical support (Longo *et al.*, 2017). GDLs are most commonly in the form of woven carbon fabric or unwoven carbon fibre paper and its structure affects the catalyst utilization and the overall cell performance (Park, Lee and Popov, 2012). Typically, the GDL also consists of a thinner microporous layer (MPL), as seen in Figure 4, which is adjacent to the catalyst layer. MPLs are treated with PTFE to produce a hydrophobic layer, to maintain the proper water balance in the cell and prevent flooding or blocking of pore channels.

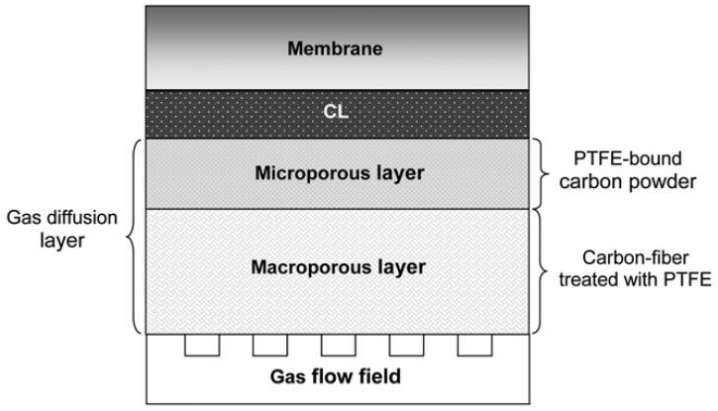

Figure 4 - Schematic cross-section of PEMFC showing the dual-layer of the GDL (Park, Lee and Popov, 2012).

2.3.4. Bipolar plates

The bipolar plates act as the electrical connections between cells and as flow-field plates to channel the feed gases over the anode and cathode of the MEA. Due to the highly oxidative conditions of the cell, the material chosen must exhibit both high resistance to corrosion and good conductivity over a wide potential range. They must also provide good mechanical stability and heat transport (Longo *et al.*, 2017). Graphite composites and metallic plates are therefore the most commonly used materials to meet these requirements.

2.4. Challenges in PEMFCs

Fuel cells convert chemical energy to electrical energy with high efficiency and are therefore considered to be a promising power source for stationary and portable energy generation (Taniguchi *et al.*, 2008). They have the advantage of low operating temperatures (50 – 100 °C), high power density (40% - 60%), nearly zero pollutants compared to conventional internal combustion engines as well as a simple structure (Qin *et al.*, 2016). They however, are prone to chemical, mechanical and the thermal degradation during its lifespan which results in a voltage and performance decline (Travassos and Rangel, 2010). Increasing the durability of the fuel cell is a major drive and a growing focus to bridge the gap between the ideal and current state of fuel cell technology (Zhang *et al.*, 2009). The lifetime goals for a fuel cell range from approximately 5000 operating hours for vehicular applications and 40,000 for stationary applications (Wilkinson and St-Pierre, 2003).

The challenges of durability and cost are the main barriers to mainstream commercialization of fuel cell technology, and some of the factors affecting these include:

2.4.1. Membrane degradation

Membrane failure not only causes a decrease in performance but also indicates the end-of-life (EoL) of the cell. The main mechanisms by which this occurs is by drying, thermal or chemical means. All three mechanisms generally result in higher permeation rates which is characterized by increased hydrogen crossover from the anode to cathode (Jourdani, Mounir and El Marjani, 2014).

2.4.2. Ionomer degradation/curing

The ionomer has long been suspected to undergo degradation, under similar conditions to the membrane, through dissolution and deactivation (Jourdani, Mounir and El Marjani, 2014). Ionomer degradation causes a decrease in ionic conductivity and reduced contact area with the catalyst particles. Unfortunately, it is very difficult to differentiate the ionomer from the Pt/C using traditional morphological techniques such as SEM which makes characterizing the ionomer degradation very challenging (Jourdani, Mounir and El Marjani, 2014).

2.4.3. Materials

Due to the finite availability of PGMs the materials used reflect in the cost of the fuel cell and in the context of commercialization, cost reduction is a major factor. The aim here is to reach the current performance with the lowest possible metal loading by increasing its utilization.

Another major materials challenge is the durability of the carbon support. Carbon corrosion of the electrodes is a known phenomenon proven to be a major cause in performance drop in a fuel cell (Perry, Patterson and Reiser, 2006). In normal operation, this degradation is not a primary cause of performance loss due to the low potential ranges (0.6 V – 0.85 V). However, during events such as start-up, shutdown and fuel starvation, the corrosion of the carbon support occurs rapidly due to higher potentials (> 1.2 V) thereby permanently damaging the catalyst layers (Yu *et al.*, 2006).

2.5. Potential reversal in PEMFCs

This thesis focusses on potential reversal in fuel cells as one of the factors that affect MEA degradation through fuel starvation. During normal operation, hydrogen and air are supplied to the anode and cathode respectively in excess to produce sufficient electrons and protons. However, there are circumstances or operating conditions, which could result in cell potential reversal. Some of these include sub-zero start-up, rapid current load changes, low catalyst performance, insufficient supply of reactants and uneven gas distribution(Qin *et al.*, 2016).

Under these conditions, hydrogen oxidation (Eq. 2.1) is not enough to maintain the current and in some cases the fuel and air can become present at the opposite electrodes; hydrogen present at the cathode and oxygen at the anode. One or more MEAs in a stack can undergo

potential reversal during operation and can be irreversibly damaged by such an incident (Taniguchi *et al.*, 2008). Once this occurs, the fuel cell will draw energy instead of suppling it. Cell reversal for even a few minutes can cause severe damage to the stack.

There are two main types of reactant starvation which occur during operation:

2.5.1. Air starvation

This can occur when there is a disruption in the air supply or when there is block on the cathode surface. For example, water converges at the cathode via three main methods; transport of humidified reactants, water generation at the cathode reaction and transport via electro-osmotic drag associated with proton transfer across the polymer electrolyte membrane (Qin *et al.*, 2016). Due to this condensed water or due to impurities present in the air, oxygen can be blocked from accessing the electrocatalyst surface.

Figure 5 shows the effects of cathode and anode potential during air starvation conditions:

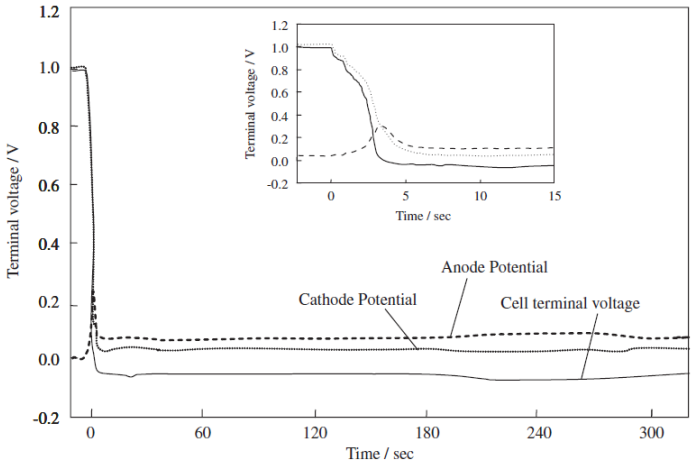

Figure 5 - Anode and cathode potentials during air starvation (Taniguchi *et al.*, 2008).

During air starvation, the cathode potential drastically drops to approximately zero and the cell voltage becomes slightly negative. There is also an initial spike in the anode potential but after a short period, the cathode, anode and cell potential all reach constant values around zero. During this phenomenon, protons and electrons produced at the anode diffuse to the cathode and hydrogen is produced. The half reactions and overall reactions are as follows:

Anode: $H_2 \rightarrow 2H^+ + 2e^-$

Cathode: $2H^+ + 2e^- \rightarrow H_2$

Overall: $H_2\ (anode) \rightarrow\ H_2\ (cathode)$

For air starvation, researchers have focused on the causes and its effects on the cell degradation. For example, Tüber *et al.*, (2003) looked at the water flooding effect on the cathode caused by water accumulation and how that promoted air starvation . Air starvation causes a reduction in performance but doesn't necessarily damage the components of the cell.

2.5.2. Fuel starvation

Compared to air starvation, the impact of fuel starvation is more far-reaching and causes more damage to the fuel cell. There are two types of fuel starvation phenomena; localized fuel starvation and complete fuel starvation. Both these conditions are similar in terms of the reactions that occur but the damage they cause and the effect to the electrodes vary.

1. Local starvation

To be precise, local starvation causes a current reversal and not necessarily a potential reversal, only when the hydrogen stoichiometry is less than 1 can the fuel cell polarity be reversed (Qin *et al.*, 2016). Local starvation happens when hydrogen occupies only part of the anode surface, and subsequently creates a high interfacial potential difference in the region where there is no hydrogen, since the cathode potential can increase up to about 1.6 V. This causes a current reversal, oxygen evolution and carbon corrosion at the cathode electrode (Reiser *et al.*, 2005; Kim *et al.*, 2008). It was found by Liang *et al.*, (2009) that the current distribution is significantly uneven during this kind of starvation. The areas where hydrogen is present will have the same potential difference as a normal fuel cell (approx. 0.8 V), while in the deprived regions, the anode potential could drop to about -0.59 V resulting in the high interfacial potential difference and then reverse current occurs (Jia *et al.*, 2016).

Reiser *et al.*, (2005) developed a one-dimensional model to simulate the change of electrode potential and corrosion current when the anode was partially filled with hydrogen during start-up (Figure 6).

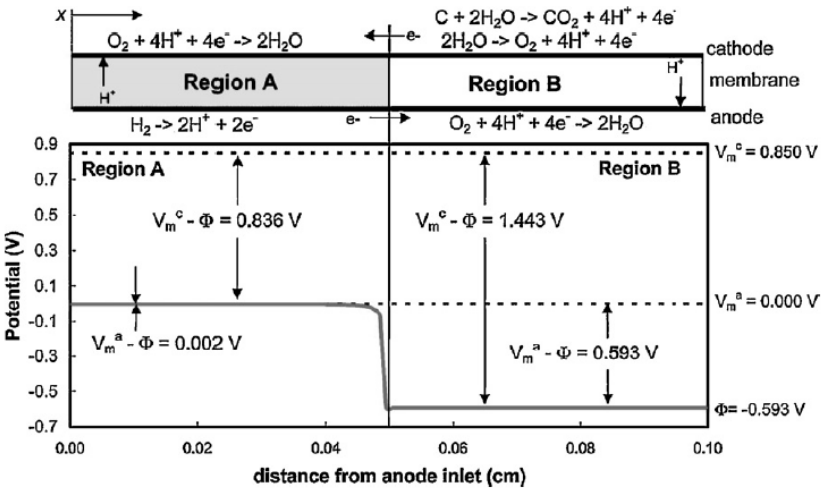

Figure 6 - Schematic showing the potential distribution along the anode flow path during current reversal (Reiser et al., 2005).

The data from Reiser *et al.* (2005) showed that this form of starvation occurred during the start-up process, but it was also proven by Patterson and Darling, (2006) that this could occur during normal operation when the hydrogen supply is interrupted. Furthermore, they found that the obstructed or starved area had to be approximately 2 mm or larger to induce significant damage to the cathode electrode.

Kim *et al.* (2008) studied anode and cathode potentials during fuel starvation using in-situ measurements. They stated that above a cathode potential of 1.2V, CO was generated electrochemically and that the rate of carbon oxidation was significantly retarded at lower temperatures. They also found that the rate of CO_2 evolution was proportional to the cathode potential above 1.0 V.

Under normal operation, all the reactants are supplied in excess to the cathode and anode resulting in an even distribution of materials to the electrode surfaces. However, localized fuel starvation can still occur during normal operation due to poor distribution, water flooding or load change. Water flooding is a phenomenon where water particles accumulate on the electrode surface therefore preventing hydrogen gas from reaching a portion of the anode and can be a result of poor water management. If irregular fuel distribution occurs, the pressure difference between the anode and cathode would also cause air or oxygen to cross the membrane from the cathode to the anode side. This creates a hydrogen/air boundary and further permits potential reversal through localized fuel starvation. The concentration

gradient across the membrane was found to be the driving force of oxygen permeation from the cathode side according Hu *et al.*, (2009), who also found that the rate of carbon corrosion at the cathode was strongly dependant on the oxygen diffusion.

Another method in which local fuel starvation occurs is during start-up and shutdown procedures. After an extended period of shut down, air fills the anode flow field due to permeation by atmospheric air from the anode exhaust or across the membrane (Yu *et al.*, 2012). When the cell is started up, air and hydrogen are pumped into the cathode and anode respectively but due to the presence of air at the anode, a hydrogen/air boundary is formed inducing localized starvation. After a period, the hydrogen flow completely dispels the air and the cell runs normally but the initial starvation can cause irreversible damage. In laboratory experiments, the cell is generally purged with nitrogen to prevent this from happening. However, in the real operation of a cell, this is not practical, resulting in the hydrogen/air boundary during start-up.

During shutdown the same situation; a hydrogen/air interface occurs. After the load has been switched off and the respective gas flows are shut off, residual gas will remain in the cell. However, due to gas concentration differences between the anode and cathode, oxygen crosses over to the anode. Figure 7 shows which reactants are present at each electrode during start-up and shutdown.

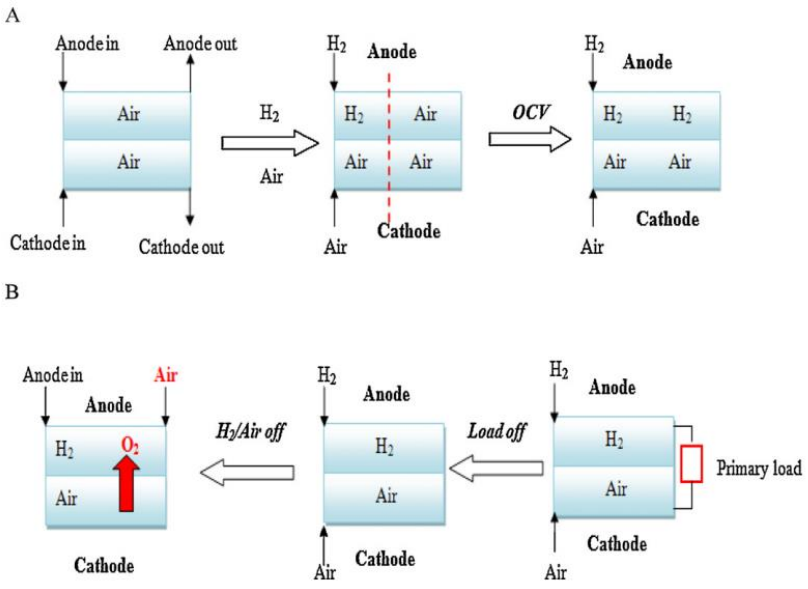

Figure 7 - Start-up (A) and shutdown (B) effect on gases present at electrodes (Yu et al., 2012).

2. Complete starvation

The other form of fuel starvation, complete starvation, occurs when the H_2 supply is insufficient to meet the load requirements of the cell or when the H_2 stoichiometry drops below 1. When this occurs, the cell drives carbon oxidation and water electrolysis reactions at the anode to maintain the supply of protons and electrons to the cathode through the following equations:

$$C + 2H_2O \rightarrow CO_2 + 4H^+ + 4e^-, \quad E° = 0.207 \text{ V vs. SHE} \qquad \text{(Eq. 2.3)}$$

$$C + H_2O \rightarrow CO + 2H^+ + 2e^-, \quad E° = 0.518 \text{ V vs. SHE} \qquad \text{(Eq. 2.4)}$$

$$2H_2O \rightarrow O_2 + 4H^+ + 4e^-, \quad E° = 1.232 \text{ V vs. SHE} \qquad \text{(Eq. 2.5)}$$

These reactions are non-spontaneous and therefore consume energy from the MEA instead of producing it. The high equilibrium potential of the water electrolysis reaction (oxygen evolution reaction: OER) increases the anode potential relative to the cathode until the cell terminal voltage reverses. Although carbon corrosion is thermodynamically favourable, water electrolysis is more kinetically favourable and therefore proceeds at a higher rate (Hong *et al.*, 2016). The high activation barriers of carbon corrosion results in sluggish kinetics which can become fast when the cell potential exceeds 1 V. Figure 8 shows the effects on cathode and anode potentials during full fuel starvation.

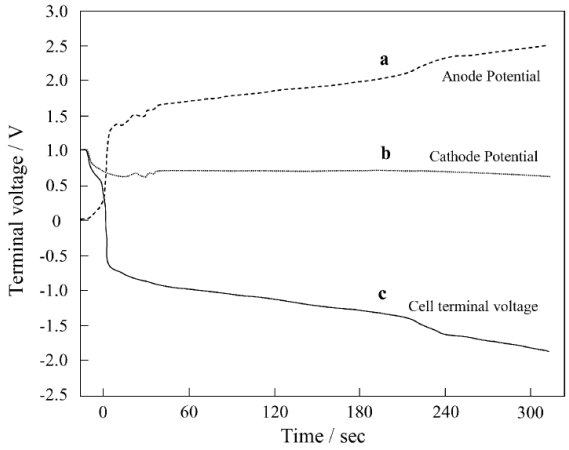

Figure 8 - Anode and cathode potentials during complete hydrogen starvation (Taniguchi *et al.*, 2004).

Fuel starvation results in cell voltage reversal reducing the power output of the stack and causing severe and irreversible damage to the cell due to carbon corrosion. If prolonged,

materials unable to withstand the high positive anode potentials will corrode if they are in contact with the flow field plates. Since the OER consumes water, the ionomer in the catalyst layer and the membrane will dehydrate (Ralph, Hudson and Wilkinson, 2006). The combined excessive heat generated from these reactions and the high potential, may also cause pin holes in the polymer electrolyte membrane. Damaged membranes will eventually lead to catastrophic failure of the cell by electrical short-circuiting.

Carbon degradation is one of the major contributors to fuel cell failure. During normal operation, carbon degradation is limited when the cell potential is within the range of 0.4V – 0.8V. The degradation is however, markedly accelerated during potential reversal at which the anode reaches potentials beyond 1.2 V (Zhang *et al.*, 2009). The effects of carbon corrosion are irreversible affecting the performance and the lifetime of the MEAs. It was found by Zhang *et al.* (2009) that the rate of carbon corrosion is highly dependent on the potential of the cell. The effects of this degradation can be seen in Figure 9.

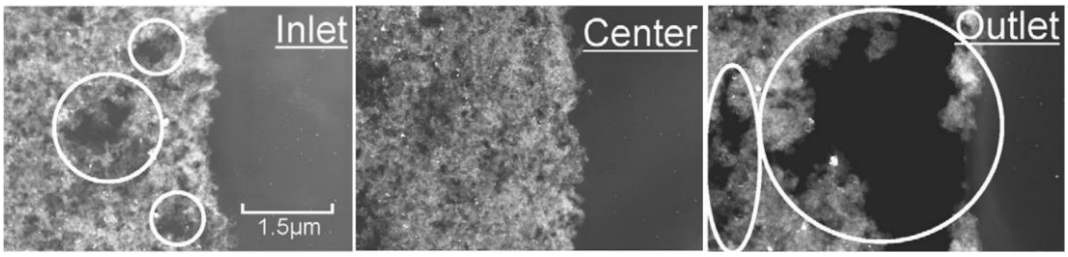

Figure 9 - STEM images near the inlet, centre and outlet of the cathode after carbon corrosion (Ishigami et al., 2011).

In addition to this, electrical impedance spectroscopy (EIS) results have shown that the charge transfer resistance increases while the ohmic resistance remains constant as the potential reversal duration increases or with multiple successive starvation periods (Kang *et al.*, 2010). This was attributed to electric shorting caused by catalyst layer degradation.

2.6. Mitigation strategies

To mitigate or prevent the effects of cell reversal several strategies have been proposed which can be classified into two main categories:

2.6.1. System management strategies

System management mitigates degradation by monitoring the operation parameters which can be adjusted through feedback loops. These parameters include gas flow rates, system temperature, air bleed, gas humidity and pressure drop. With auxiliary equipment, one can detect reversed cell potentials by monitoring cell voltages of individual cells or a group of cells. In addition, with the use of electrode segmentation technology, the current density and temperature distribution of individual cells in a stack can be measured to indicate when individual cells go into potential reversal.

Some of these strategies include gas purging at the anode using recycled exhaust gas or reaction gas at start-up and shut-down to eliminate the hydrogen/air boundary (Yu *et al.*, 2012). Another strategy investigated by Kim *et al.*, (2009) proposed an applied auxiliary load to consume residual oxygen at the cathode and was found to significantly reduce performance decay and loss of electrochemically active surface area in the MEA.

Other variables associated with voltage reversal can also be measured. For example, a specially constructed sensor cell which is more sensitive to conditions leading to cell reversal may be employed. Therefore, instead on monitoring every single cell in the fuel cell stack, only the sensor cell needs to be monitored to prevent widespread effects of the reversal (Wilkinson and St-Pierre, 2003). However, there may be instances where the sensor cell may not be able to detect cell reversal; such as a defective individual cell. Alternatively, the exhaust gas monitors can be used to detect a reversal in the stack by checking for abnormal amounts of gas species that originate from the reactions that occur during cell reversal (such as carbon dioxide and carbon monoxide)(Knights *et al.*, 2003). Unfortunately measuring gas exhaust species only informs of an ongoing cell reversal within a stack and does not identify the specific problem cells nor provide any warning of the impending event.

One of the most effective system management strategies to reduce local fuel starvation is to practice fuel recycling. This fuel recycle loop reduces the fuel utilization of the stack to achieve a set system fuel utilization, by increasing the volume of fuel flowing through the stack. Recycling also allows for relatively high fuel velocities through the anodes even during low current conditions (Perry, Patterson and Reiser, 2006).

Because these auxiliary systems can be quite complex and expensive to install, significant research has also been focused on modification of the materials used in the fuel cell.

2.6.2. Material modifications

Material modifications, unlike system management strategies, aim to prevent and reduce the effects of carbon degradation once an event such as starvation occurs. Herein, materials which are resistant to or inhibit the adverse effects of cell reversal are used. The main material amendments which are researched to counteract potential reversal include (Qin *et al.*, 2016):

- Using corrosion resistant supports,
- Increasing water retention capabilities with materials such as PTFE,
- Addition of an oxygen evolution reaction (OER) catalyst to promote water oxidation instead of carbon corrosion.

Replacing conventional carbon supports with more corrosion resistant materials has been an important mitigation strategy. It was found the using graphitized carbon rather than the non-graphitized carbon support resulted in a 5 times slower degradation rates (Yu *et al.*, 2006). The start-up and shutdown degradation rates were also reduced by 25% when graphitized carbon was implemented in the microporous layers (Owejan, Yu and Makharia, 2007).

With regards to including an OER catalyst in the design of a reversal tolerant anode, several metal oxides have been researched (Ralph, Hudson and Wilkinson, 2006). The results showed that the addition of the OER catalyst can delay the cell potentials from dropping to severe carbon corrosion condition for a period.

2.7. Iridium oxide (IrO_x)

Due to the slow kinetics of the OER, a catalyst is added to increase the reaction rate and subsequently the generation of O_2 through electrolysis. An existing material-based solution to potential reversal is through the addition of an OER catalyst to the anode layer. This prolongs the water electrolysis stage and delays the half-cell potential from exceeding 1.2 V where severe carbon corrosion occurs. In this study, an anode which can withstand cell reversal is referred to as a reversal tolerant anodes (RTA). The key to successful RTAs, which include the addition of a highly active OER catalyst to the anode layer, is that it doesn't affect

the HOR and ORR and is effective under all operating conditions; including high temperatures as well as low and high relative humidity (RH).

In determining the best catalyst for this purpose, ruthenium and iridium were found to be among the most active towards the OER (Cherevko *et al.*, 2015). When compared, the respective oxides of the metals showed lower activities than the metallic forms in the following order:

$$Ru > Ir > RuO_x > IrO_x$$

The activity of the electrocatalyst can be determined through ex-situ electrochemical measurements. This is done by either measuring the current density produced at a given potential (usually 1.55 V or 1.525 V) or by measuring the overpotential at a specific current density (usually 10 mA/cm^2 or 5 mA/cm^2) (Mccrory *et al.*, 2013; Alia *et al.*, 2016). The higher the current generated at given potential, the more active the electrocatalyst is. The mass activities of IrO_x have varied from study to study (15 – 60 A/gIr) and this is mainly because the activity of the catalyst is synthesis dependant (Abbott *et al.*, 2016; Alia *et al.*, 2016).

However, when it comes to the durability of these catalysts under OER conditions, both the metallic Ru and Ir catalysts deactivated faster than their oxide forms having dissolution rates 2-3 orders magnitude higher (Cherevko, 2018). The order of durability is as follows:

$$IrO_x > > Ir > RuO_x >> Ru$$

The durability of the OER catalyst is evaluated by how its activity changes during operational cycling. It was found that the loss in activity is mainly dependant on the potential (Cherevko et al., 2015). At moderate potentials (1.2 V – 1.6 V) there is small amounts of dissolution, but particle growth is the main factor that drives deactivation. At higher anodic potentials (>1.6 V), dissolution of Ir occurs at a much faster rate and therefore becomes the main factor affecting the loss of activity (Alia et al., 2016).

Furthermore, a benchmarking study performed by McCrory *et al.*, (2013) also showed that IrO_x was the best catalyst for the OER as it exhibited the lowest overpotential in both acidic and alkali media among several noble metal oxides. IrO_x therefore provides the most favourable balance between activity and stability under the conditions required for the OER.

Given the low abundance and high price of Ir metal, having a better understanding of the kinetics and mechanism of its electrochemical dissolution is important for improvement on its performance (Kasian *et al.*, 2018). There has been debate over the dissolution mechanism of IrO_x which occurs during the OER, however, due to improvements in X-ray Absorption Spectroscopy (XAS) and X-ray Photoelectron Spectroscopy (XPS) based techniques, the presence of Ir^{3+} and Ir^{5+} intermediates were confirmed which allowed for another mechanism to be proposed (Cherevko, 2018). Figure 10 below shows the dissolution mechanism that is most accepted and the reaction pathways in which the OER occurs.

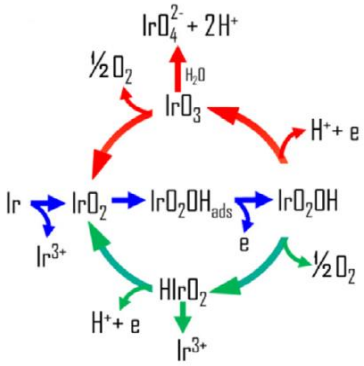

Figure 10 - Most widely accepted dissolution mechanism of IrO_x (Kasian et al., 2018).

The most electrochemically favourable route for the OER was found to be via Ir^{3+}/Ir^{4+} (green path on diagram). At low anodic potentials (< 1.6 V) a small amount of dissolution occurs through the formation of the soluble Ir^{3+} intermediate and at higher anodic potentials (> 1.6 V) the dissolution rate increases and occurs via Ir^{6+} (Cherevko, 2018). Finally, it was found that the rate of dissolution increased with operating temperature

2.8. Catalyst supports

Even though IrO_2 it is a good catalyst for the OER, it is an expensive catalyst, and its nanoparticles which have high specific surface energies are prone to agglomeration which significantly reduce its ECSA. This results in lower catalyst utilization and decreased OER performance during the operation. One way to address this challenge is to utilize catalyst supports, which will increase dispersion and reduce agglomeration of the active electrocatalyst (Oh *et al.*, 2016). Several studies have investigated using various supports (including noble metal oxides and ceramics) and have proven that the anchoring effect from

the metal support interactions increases the stability of the catalyst (Antolini and Gonzalez, 2009).

The ideal catalyst support should have the following properties:

1. High specific surface area to enable high level catalyst dispersion
2. High electrical and thermal conductivity
3. Easily fabricated into electrodes
4. Available at low costs and high purity
5. Good corrosion resistance in PEMFC electrolyte
6. Mechanically stable with reasonable strength

Although some metal oxide and ceramic supports show encouraging results, most possess low surface areas resulting in low catalyst dispersion and consequently, low electrochemical activity (Antolini and Gonzalez, 2009). The use of carbon is also not ideal because it can be easily oxidized to CO_2 under the conditions required for the OER (Oh *et al.*, 2016).

Graphitized carbon supports have been gaining more attention due to its high surface area, chemical stability, corrosion resistance, superior electrical conductivity and low electrical resistivity (Sadhasivam *et al.*, 2016). Graphitic content has also been found to be more robust and resistance towards carbon corrosion. Castanheira *et al.* (2015) showed Pt on reinforced-graphite only had a 25% loss in ECSA compared to the 60% and 80% loss observed by Pt on Vulcan and Pt on high-surface area carbon respectively. Moreover, considering the strong interaction between graphene and nanoparticles with functional groups, it is harder for noble metal catalyst nanoparticles to dissolve or sinter (Guo and Sun, 2012).

Despite this, no conclusive studies using graphitized carbon as a support for IrO_x for the OER in an RTA were found in available literature.

2.9. Fuel starvation accelerated degradation test

To determine the various degradation pathways in MEAs or fuel cell stacks, researchers have developed several accelerated stress tests (AST) to simulate specific conditions which affect fuel cell's lifetime in a reasonable timeframe. During ASTs, different stressors are applied to the fuel cell to determine the durability of the whole cell or a particular component; either

in-situ or ex-situ (Zhang *et al.*, 2009). A study by Zhang *et al.,* (2009) gives a detailed summary of most of the developed AST testing methods and which components they probe for durability. Fuel starvation ASTs have been performed by several researchers to determine the mechanisms, limitations and recovery associated with it (Baumgartner *et al.*, 2008; Liang *et al.*, 2009; Kang *et al.*, 2010; Travassos and Rangel, 2010). These tests can either be carried out by reducing the hydrogen stoichiometry supplied to the cell below 1 while maintaining the air stoichiometry and current density constant or by keeping both gas stoichiometries constant and increasing the load requirement. During these tests, the voltage response over time is measured as illustrated in Figure 11. Depending on the composition of the MEA, it will either fall to a carbon corrosion potential or clamp at the water electrolysis potential for a period.

A measure of an MEA's reversal tolerance is how long the potential can be clamped at the water electrolysis potential before entering severe carbon corrosion potentials. These tests can be coupled with gas chromatography to determine the CO_2 produced when carbon oxidation begins in a potential reversal event.

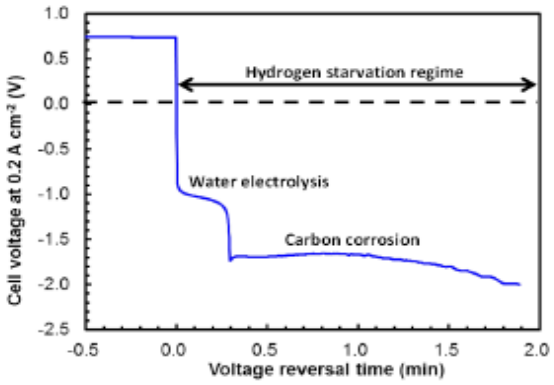

Figure 11 - Voltage vs time curve for fuel starvation AST showing the potentials at which the respective reactions occur.

2.10. Performance evaluation techniques in MEAs

During single cell testing of an MEA, whether for stress tests or normal operation, it is vital to monitor its components, processes and performance. To assess the effects of degradation and loss of performance which occur in an MEA, several diagnostic tools have been developed

to probe various elements of the MEA. These include but are not limited to polarization curves, electrochemical impedance spectroscopy and cyclic voltammograms.

2.10.1. Polarization curves

Polarization curves are obtained by recording the steady state response of the fuel cell and are displayed as voltage against current density plots. In these measurements a current is demanded of the cell and the corresponding voltage is measured. The current density is obtained by dividing the current output by the geometric active area of the MEA which allows for normalization. For fuel cells, the power output (or current) is directly proportional to the geometric active area. The power output of a fuel cell can be directly obtained from a polarization curve.

A typical polarization curve illustrating the performance of a single MEA is shown in Figure 12. Where V_{fc} is the measured fuel cell potential, V_{nernst} is the theoretical potential calculated via the Nernst equation, and V_{ohm}, V_{act} and V_{conc} are the contributions of the ohmic, activation and mass transport losses to the measured potential respectively.

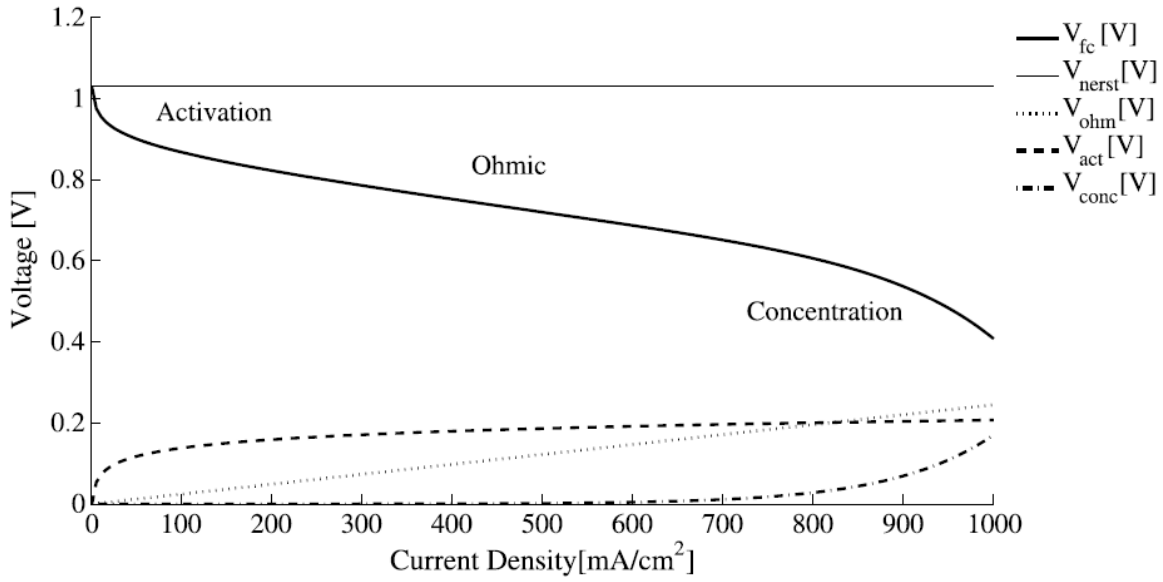

Figure 12 - Polarization curve of single cell MEA (Kunusch, Puleston and Mayosky, 2012).

The cell voltage varies with the electrical load, and this is as a result of electric losses. These losses can be classified as activation, ohmic and concentration (or mass transport) losses.

Activation losses are caused by a portion of the total voltage being used to induce the reaction kinetics of the HOR and ORR. An amount of energy is also needed to transport the electrons to and from the electrodes, this is known as the exchange current density, which is dependent on temperature and gas pressure. The kinetics of the HOR at the anode occurs much faster than that of the ORR at the cathode, therefore much of the activation losses can be attributed to the cathode.

Ohmic losses are due to protonic resistance caused by the polymer electrolyte membrane, and electrical resistance from the electrodes and current collectors. These losses are proportional to the electric current in a wide operational range.

Mass transport losses are due to the finite rate of diffusion of the reactants through the pores of the GDL and catalyst layers. At high current densities this creates a concentration gradient on the catalyst surface as the reactions take place and leads to the voltage drop. In order to reduce mass transport losses, reactant gas pathways should not be blocked or limited. In PEMFCs, it is therefore vital to have an effective transport of the water away from the cathode electrode to reduce flooding which prevents reactant access to catalyst sites.

Combining all these losses, the cell voltage can be written as:

$$V_{fc} = E - V_{act} - V_{ohm} - V_{conc}$$

From polarization curves, the performance of the fuel cell can be compared before and after a potential reversal event.

2.10.2. Electrochemical Impedance Spectroscopy

Electrochemical impedance spectroscopy (EIS) can be used in both in-situ and ex-situ catalyst testing. In ex-situ tests, it provides useful information about the solution and charge transfer resistances.

In MEA tests (in-situ) EIS is a suitable diagnostic tool because it is non-destructive and provides useful information on the dynamic response and status of an MEA. One main advantage of EIS is that it can distinguish between the individual contributions of the interfacial charge transfer and the mass transport resistances in the catalyst layer and the diffusion layer (Asghari, Mokmeli and Samavati, 2010).

It can be measured by either recording the potential response generated by applying an alternating current with different frequencies or recording the current response to a sinusoidal potential at different frequencies. The amplitude is usually kept low so that the potential or current response within the range lies in the linear portion of the polarization curve. An equivalent circuit is an electrical circuit used that can be modelled to the system to extract meaningful data from the different regions in the MEA (Figure 13). The circuit is modelled using resistors (R), capacitors (C), and inductors (L). An MEA does not demonstrate ideal electrochemical behaviour, therefore specialized components such as the Warburg element (Z_w) is used which represents the diffusion and mass transport impedances of the cell (Scribner Associates, 2014). The anode and cathode impedances are denoted by resistors (representing Faradaic resistance of the electrochemical reactions) in parallel with capacitors (representing the double-layer capacitance of the electrolyte-electrode interface).

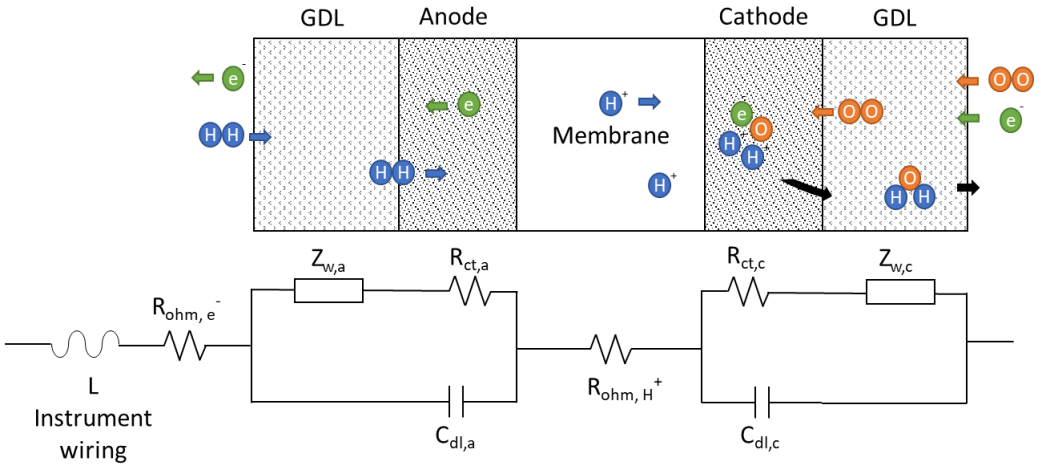

Figure 13 - Equivalent circuit model of PEMFC modelled from Scribner Associates (2014).

The data from the EIS can be plotted as a Nyquist plot for PEMFCs (Figure 14). There are four main regions that are represented on the Nyquist plot which correspond to the potential losses seen in the polarization curves; ohmic, activation and mass transport effects.

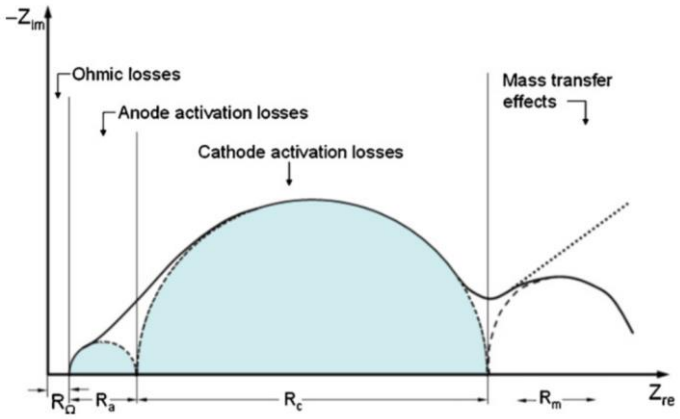

Figure 14 – A typical Nyquist plot for a PEMFC (Zhu, Payne and Tatarchuk, 2007).

The Nyquist plot consists of two semi-circles corresponding to the anode and cathode activation losses, with the first intercept representing the ohmic resistance of the cell.

To capture all the dynamic processes that occur in a single MEA, a frequency range between 0.1 Hz and 10 kHz is typically chosen. At high frequency ranges (> 100 Hz), the fast processes such as the HOR, and ionic and electron conduction are prominent in the impedance spectra. At intermediate frequency ranges (1 Hz to 100 Hz), slower processes such as the ORR are more dominant and the much slower process such as the effects of mass transport are seen at low frequencies (< 1 Hz). As the resistances of the cathode is much larger due to sluggish ORR kinetics, the cathodic activation losses outweigh that of the anode (Asghari, Mokmeli and Samavati, 2010), and therefore present with a larger semi-circle.

2.10.3. Cyclic voltammetry

Cyclic voltammetry can be used for both ex-situ electrochemical evaluations as well as in-situ MEA testing.

In MEA testing, cyclic voltammetry is used to determine the electrochemical surface area (ECSA) of platinum on the cathode. From there, the Pt catalyst changes which occur during degradation studies, such as potential reversal, can be observed (Taniguchi *et al.*, 2008). During cyclic voltammetry, the applied potential is varied, and the current response is measured. For Pt, the region between 0 V and 0.4 V vs RHE is known as the reversible hydrogen adsorption and desorption region. This process is due to the underpotential deposition of a hydrogen monolayer in the negative sweep and release of protons (H^+) in the positive sweep (Climent and Feliu, 2011), according to the following reactions:

$$Pt + H^+ + e^- \rightarrow Pt - H_{ads}$$

$$Pt - H_{ads} \rightarrow Pt + H^+ + e^-$$

The cyclic voltammogram below (Figure 15) is of polycrystalline Pt and shows the reversible hydrogen adsorption and desorption peaks.

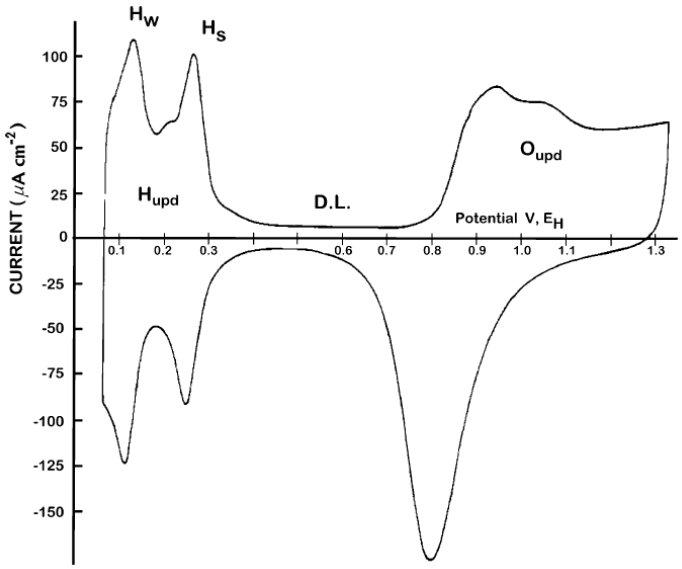

Figure 15 - Cyclic voltammetry for polycrystalline Pt adapted from Climent and Feliu (2011).

The ECSA for Pt can be calculated by integrating under either the adsorption/desorption peaks minus the double layer capacitance, as the hydrogen adsorption charge associated with a platinum surface is known.

$$ECSA = \frac{Q_h}{Pt\ catalyst\ loading\ \times\ Q_m}$$

Where Q_h is the total charge transfer due to hydrogen adsorption, and Q_m is the hydrogen adsorption charge for a smooth polycrystalline platinum surface which is 210 µC/cm^2.

3. Experimental Procedure

The experimental procedures required in this project is outlined in this chapter and consisted of the following major steps;

- Synthesis and characterization of the OER supported catalyst.
- Electrochemical evaluation of the supported catalyst performance and durability.
- Manufacturing and testing of membrane electrode assemblies (MEAs) performance which included the supported catalyst in the anode.
- Subjecting the produced MEAs to cell reversal conditions to determine their durability.

3.1. Preparation of OER catalyst

For the synthesis of the IrO_x support on graphitized Vulcan (GV), the following procedure was used.

100 mg of hexacholoroiridic acid hexahydrate ($H_2IrCl_6 \cdot 6H_2O$ – Sigma Aldrich; 208973-5G) and 30 ml of ethylene glycol (E.G.) were added to a beaker and sonicated for 30 min. Thereafter 450 mg of the GV support was added to the solution and mixed using a magnetic stirrer for 10 min at room temperature followed by sonicated for 30 min. The pH of the solution was adjusted to pH 11 using 1 M NaOH dissolved in E.G. The solution was degassed with argon for 10 min to remove all dissolved oxygen before being placed in a conventional 900 W microwave (Defy DMO 350) for 1 min 45 s to deposit the Ir metal onto the carbon support. The solution was heated at 200 °C to remove excess E.G. The semi-dry Ir/GV powder was washed and centrifuged 3 times with deionized water to remove the NaCl salt byproduct and then dried overnight at 60 °C. The Ir/GV powder was calcined in air to oxidize the Ir nanoparticles to IrO_2 at 420 °C for 30 min.

3.1.1. Microwave assisted polyol deposition

The synthesis method used to generate the IrO_x plays a huge role in the performance and durability of the electrocatalyst. Several methods have been studied such as the Adams fusion method, reactive sputtering, electrochemical techniques and thermal methods, with each

technique having its own drawbacks. For example, electrochemical techniques require intricate pre-treatment processes such as acid or base treatment, gas conditions and humidity control to deposit the nanoparticles on the substrate. Reactive sputtering on the other hand is very slow and difficult to control the reaction conditions (Kim *et al.*, 2015).

One of the main reasons for using a polyol deposition technique was to utilize its cost and time effectiveness in the synthesis of the OER catalyst. This method utilizes poly-alcohols (or polyols – compounds with two or more hydroxide groups) which act as both the solvent and reducing agent to obtain finely divided metals from their respective, oxides, hydroxides and salts. Besides its high reducing capability of noble metals, the polyol medium offers multiple other benefits (Fievet *et al.*, 2018):

- The high boiling point of the solvent allows for synthesis at relatively high temperatures which provides crystallized materials
- Controlled structures and morphologies can be obtained due to the highly viscous nature of the solvent which favours a diffusion-controlled regime for particle growth
- The reducing medium prevents the reduced metal particles from being oxidized
- It minimizes coalescence through its ability to coordinate the particle surface as well as the metal precursors

Ethylene glycol (EG) is the most widely used polyol and was therefore chosen for this synthesis as well. During the reaction, the electrons required for the reduction of the noble metal salt to metallic particles are obtained from the oxidation of the EG.

Recently, microwave-assisted wet chemical synthesis techniques have been used for a variety of organic, inorganic and hybrid materials. The use of microwave irradiation has the benefit of fast and uniform heating of the reaction medium which leads to the formation of nanoparticles with uniform shape and size. The increased heating rate also typically enhances the reaction kinetics and leads to an increase in reaction rate compared to the standard heating methods (Anumol *et al.*, 2011). This has therefore been paired with the polyol method in several studies to synthesize numerous materials.

3.2. Physical characterization of the supported catalyst and MEAs

Several methods were used to characterize the intermediates and products throughout the preparation of the IrO_2 supported catalyst as well as the prepared membrane electrode assemblies (MEAs).

3.2.1. X-Ray Diffraction (XRD)

XRD was performed on a Bruker D8 ADVANCE diffractometer (Co-Ka radiation, 35 kV, 40 mA) to determine the crystallographic structure and chemical composition of the synthesised Ir and GV supported IrO_2 products. The XRD instrument conditions are tabled in Table 1.

Table 1 – The XRD calibration settings used for the material characterization.

Property	Value	Unit
Scanning angle	20 – 100	°
Step size	0.023	°
Temperature	25	°C
Current	40	mA
Generated voltage	35	kV
Scanning time	2773	s
Source	Cobalt	-
Scanning type	Coupled TwoTheta/Theta	-
Scan mode	Continuous PSD fast	-

3.2.2. Transition electron microscopy (TEM)

TEM analysis was performed in the Electron Microscope Unit (EMU) at the University of Cape Town on a FEI/Tecnai T20 TEM with a high-resolution camera and electron energy loss system (EELS). A small amount of the synthesized IrO_x/GV was mixed with acetone and sonicated for 1 min. A few drops of the dispersion were deposited onto a carbon coated copper grid. The acetone was evaporated under a UV- lamp for approximately 5 min. This was performed to evaluate the distribution and particle size of the nanoparticles deposited on the graphitized carbon support.

3.2.3. Thermo-gravimetric analysis (TGA)

Thermogravimetric Analysis was performed on an SDT 560 TGA at the University of Cape Town. A small amount (2 – 10 mg) of sample was place in a ceramic crucible and oxidized in synthetic air at 10 °C per min from 25 °C to 800 °C. TGA was performed on the graphitized carbon support to establish its oxidation temperature and on the synthesized catalyst to determine the Ir loading.

3.2.4. Scanning Electron microscopy (SEM) and Energy Dispersive X-Ray Spectroscopy (EDX)

SEM and EDX were carried out on a Nova NanoSEM 230 at the EMU at the University of Cape Town, using an Oxford X-Max detector and INCA data acquisition software. SEM was used to determine the thickness of the respective MEA layers before and after the accelerated degradation tests. EDX was used to determine the approximate loading of Ir in the sample.

3.2.5. X-ray Photoelectron Spectroscopy (XPS)

XPS analysis was performed at the University of Southern Denmark on a spectrometer from SPECS® and the data analysed using the CasaXPS™ software. The spectroscopic analysis was used on the synthesized catalyst samples before and after oxidation using a Magnesium source. Two scans were taken for each sample – a wide scan at 50 eV and a narrow scan at 25 eV for each peak of interest. XPS analysis would determine the Ir, Pt and O oxidation states present in the synthesized catalyst and in the MEAs before and after testing.

3.3. Electrochemical evaluation of the supported catalyst

Electrochemical evaluations were performed on the synthesised IrO_2/GV to determine the OER performance and durability of the supported catalyst.

Cyclic voltammetry (CV) is perhaps one of most versatile electrochemical analysis techniques due to its ability to rapidly observe the redox behaviour in electrocatalysts over a wide potential range. CV can be used to determine the ECSA, reaction kinetics and reaction mechanisms occurring on the electrode.

To make the ink for electrochemical analysis, 5.0 ± 0.2 mg of the synthesized catalysts was made into a suspension with 25 µl 5% Nafion, 1.25 ml isopropanol (IPA) and 1.25 ml Ultrapure

Milipore water. The inks were sonicated in an ultrasonic bath for 30 s and then horn sonicated for 1 min.

Once the catalyst in the ink was adequately dispersed, 10 µl was drop cast onto a polished glassy carbon electrode with a diameter of 2.5 mm. This was then left to dry in air until all the solvents had evaporated. To ensure consistency and reproducibility, a new ink was made for every batch of tests run and immediately drop cast onto a glassy carbon electrode to mitigate any possible settling in the ink. All glassware (including beakers, electrochemical cell, bubblers etc.) were cleaned using a Nochromix bath. They were soaked overnight in the bath thereafter cleaned thoroughly using ultra pure water (18.2 MΩ.cm). Once cleaned they were submerged in a 5L beaker filled with ultra pure water for storage before use.

All electrochemical measurements were performed on a three-electrode cell using a $Hg/HgSO_4$ reference electrode, a platinum wire counter electrode and the glassy carbon working electrode. The electrolyte used was a 0.1 M $HClO_4$ prepared with ultra pure water and the solution bubbled with Argon gas to remove all dissolved oxygen.

Cyclic voltammetry was performed between 0.0 V to 1.2 V vs. SHE at 100 mV/s for 100 cycles to condition and clean the electrode surface. This was followed by 4 scans in the same potential range at 20 mV/s. The activity was determined by cycling the potential between 1.2 V and 1.65 V at 5 mV/s and a rotational speed of 1600 rpm. In this region, the OER is being probed and the mass activity was measured as the current density at 1.55 V. The electrochemical cell was tilted, and the working electrode rotated to remove any O_2 gas bubbles that form on the electrode surface which block the catalyst surface and affect the measurements. To correct for internal resistance, electrochemical impedance spectroscopy (EIS) measurements were taken between 100 mHz and 100 kHz.

The ECSA was calculated from the electrochemical double-layer capacitance of the catalytic surface. The non-Faradaic capacitive current associated with double layer charging (Mccrory *et al.*, 2013) was measured between 0.42 V and 0.52 V. Since the double layer charging is dependent on the scan rate, different scan rates were used, and their respective currents recorded. The non-Faradaic region was scanned at 10, 25, 50, 100, 250 and 500 mV/s. The ECSA was then determined by dividing the double layer capacitance by the specific capacitance of Ir and then normalizing with respect to the mass of Ir present.

During the durability study, the working electrode was tilted and rotated at 1600 rpm. The potential was cycled 5000 times between 0.6 V and 1.6 V at 500 mV/s. Performance scans were recorded after every 10 cycles till 100 cycles, every 100 cycles till 1000 cycles and finally every 1000 cycles till 5000 cycles were reached. The performance cycles were performed at 5 mV/s between 1.2 V and 1.65 V.

3.4. MEA preparation

The synthesis procedure was scaled up to meet the required amount needed to make a set of MEAs for a full set of testing. The design for the reversal tolerant anode (RTA) MEA was a single layer anode with both the platinum catalyst (GV40 from HyPlat™) and supported OER catalyst evenly dispersed and distributed throughout the layer. The Pt to IrO_x ratios investigated were 1:1 and 1:0.6.

The OER catalyst was weighed to meet the desired loading on the anode layer and added to the Pt/C in a beaker. A water-Aquivion™ and isopropanol mixture was added to the catalyst powders to manufacture the catalyst ink.

The ink was sprayed onto a membrane to generate a catalyst coated membrane (CCM) with the properties stated in Table 2. These were gasketed between two sheets of polyethylene terephthalate (PET) at 76.7 °C (170 °F) and compressed at 3 bar for exactly 1 min so as not to damage the CCMs. The CCM was then placed in between Avcarb MB30 gas diffusion layers, ready for testing.

Table 2 - The properties of the manufactured MEAs.

Property	Value	Units
CCM active area	25	cm^2
Membrane type	Gore M735.18	-
Membrane thickness	25	µm
Ionomer	Aquivion	-
Gas diffusion layer material	Avcarb MB30	-
Gas diffusion layer thickness	205	µm
Cathode Pt loading	0.4	mg/cm^2
Anode Pt loading	0.1	mg/cm^2
Anode Ir loading	0.1 / 0.06	mg/cm^2

3.5. MEA single cell performance testing

The performance of the reversal tolerant anode MEA was tested using three testing protocols with varying humidities (Table 3) to probe various MEA operating conditions. The MEA performances were compared to the commercially available GV40 MEAs (HyPlat™), to determine if the presence of IrO_x/GV catalyst on the anode influenced the performance of the MEA.

Table 3 – Humidity conditions of the different testing protocols.

Protocol	Anode RH	Cathode RH	Cell temperature
1 (High)	75%	80%	80 °C
2 (Mid)	59%	59%	75 °C
3 (Low)	52%	52%	75 °C

All MEA performance tests were performed in a Pragma cell which uses manual compression while degradation tests were in Baltic cell which uses automatic compression on the FuelCon test station. The performance tests were done on MEAs with a 25 cm^2 active area. To maximize the number of tests which could be performed, the MEAs, were cut and gasketed into 10 cm^2 MEAs for the degradation tests. Two test cells were used because the Pragma cell can test MEAs with a minimum active area of 25 cm^2 while the Baltic can test MEAs with smaller active areas such as 10 cm^2.

Before each test, the MEA was conditioned for 12 cycles between 0.3 V and 0.8 V to hydrate the membrane at the operating conditions shown in Table 4.

Table 4 - Steady state conditions

Property	Value	Unit
Cell temperature	80	°C
Anode relative humidity	60	%
Cathode relative humidity	60	%
Anode gas stoichiometry	1.5	-
Cathode gas stoichiometry	7.15	-
Cell compression pressure	4.8	bar
Anode backpressure	1.5	bar
Cathode backpressure	1.5	bar

3.5.1. Hydrogen crossover

Hydrogen crossover measurements were conducted by replacing the humidified air to the cathode with humidified nitrogen while still running hydrogen on the anode. The potential was then stepped from 0 V to 0.9 V in intervals of 0.1 V and the current density measured at each potential step. At each potential step the current that is measured is solely from hydrogen crossing over from the anode to the cathode and therefore gives an indication of the integrity of the membrane. High current densities would indicate possible membrane damage and the formation of pinholes. Hydrogen crossover tests were performed before and after the degradation tests to establish whether fuel starvation damaged the membrane.

3.5.2. Cyclic Voltammetry (CV)

Cyclic voltammograms were performed to assess any change in the ECSA after the fuel starvation AST. Hydrogen and nitrogen were fed to anode and cathode respectively for 30 minutes to purge all oxygen from the system and the relative humidity of both gases was set to 100%. During the measurements the nitrogen valve was closed, and no gas was flowed over the cathode. The potential was then cycled 15 times between 0.04 V and 0.9 V at a rate of 0.05 mV/s and the current response recorded.

3.5.3. Electrochemical Impedance Spectroscopy (EIS)

EIS was performed to understand the dynamic response and status of individual components of the cell. These tests were performed using the built-in TrueData-EIS on the Fuel-Con Evaluator-C test station which has a maximum DC current of 1000 A and a frequency range between 200 µHz and 100 kHz.

The data was recorded by sweeping the AC frequencies over the range of 20 kHz to 0.1 Hz at 0.02 A/cm^2 to determine the anodic and cathodic charge transfer resistances as well as ohmic resistances.

3.6. Cell reversal stress test

To simulate fuel starvation, the humidified H_2 feed was replaced with a humidified N_2 stream, while maintaining air flow through the cathode and a required current density of 0.2 A/cm^2.

This was done by connecting the fuel cell to an external load of 2 V. Several starvation periods were simulated and were repeated multiple times with varying recovery times in between each reversal event (Table *5*). The recovery time was the period between the successive starvation periods where the N_2 was switched back to H_2 and the cell. The relative humidity was kept at 60% for both anode and cathode during both the starvation and recovery periods. And the gases having a flowrate of 1.0 NLPM (normal litres per minute) for nitrogen and air, and 0.33 NLPM for hydrogen. In the indefinite hold test, the cell was starved of hydrogen for an unlimited time to determine how long the OER catalyst could maintain the potential above -1.2 V (which was taken to be the point of failure in the test).

Table 5 - Durability protocols used to probe the reversal tolerance of the MEAs.

	Reversal time (min)	Cell recovery time (min)	No. of reversal events
1	5	30	5
2	5	10	5
3	10	30	5
4	10	10	5
5	30	30	2
6	30	10	2
7	Indefinite	-	1

Before and after AST tests and electrochemical evaluations, SEM analysis was performed on the cross-section of the MEAs to determine any change in catalyst layer thickness.

All fuel starvation ASTs were performed on the FuelCon Evaluator-C and Baltic cell fixture as shown in Figure 16.

A 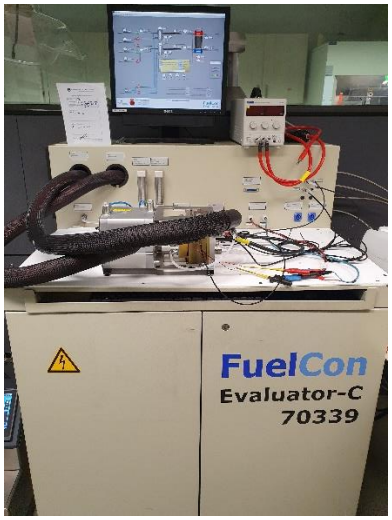

B 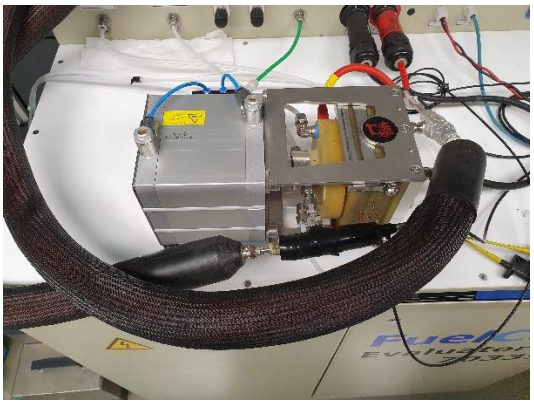

Figure 16 - (A) FuelCon Evaluator-C test station (B) Baltic MEA cell fixture.

4. Synthesis and Physical Characterization of the OER supported catalyst

This chapter discusses the results of the synthesis of the iridium oxide (IrO_x) supported on graphitized vulcan (GV) and the physical characterization performed.

4.1. Characterization of IrO_x on graphitized Vulcan

The techniques used to characterize the synthesized catalyst were performed at various stages during the synthesis procedure to confirm the structure and chemical composition of both intermediate and final products.

4.1.1. X-Ray Diffraction (XRD) and Transmission Electron Microscopy (TEM)

XRD was performed on GV coated with Ir before and after calcination to verify whether Ir was successfully deposited onto the GV support, and if the deposited catalyst was oxidized to IrO_2. Figure 17 (a) shows that the XRD pattern for GV after the microwave assisted deposition of Ir before calcination. The diffraction pattern did not show any peaks corresponding to Ir (PDF 03-065-1686), but only the graphitised carbon support. The sensitivity of XRD is limited by the particle or crystallite size, at around 2 nm. The presence of Ir nanoparticles on the GV was confirmed with TEM analysis, shown in Figure 18 (a). This TEM image shows uniform, spherical Ir nanoparticles well dispersed on the GV support. The particle size distribution (PSD), measured over 250 particles, showed an average particle size of 1.13 nm with 80% of the particles lying in the range of 0.5 – 1.5 nm (Figure 18 (b)). Figure 17 (b) shows the supported catalyst after calcination. the spectra showed peaks that corresponded to crystalline IrO_2 (PDF 00-043-1019). Moreover, no metallic Ir was found to be present in the sample, therefore indicating successful synthesis of the OER catalyst.

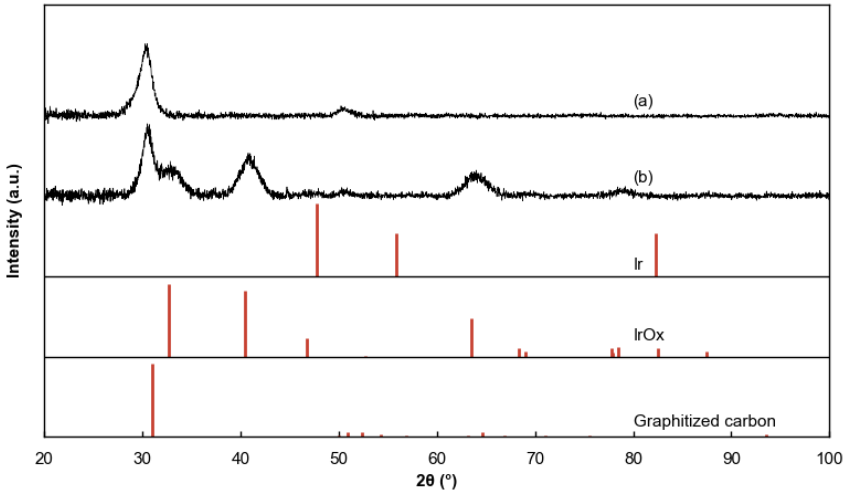

Figure 17 - XRD pattern of synthesized supported catalyst before and after calcination.

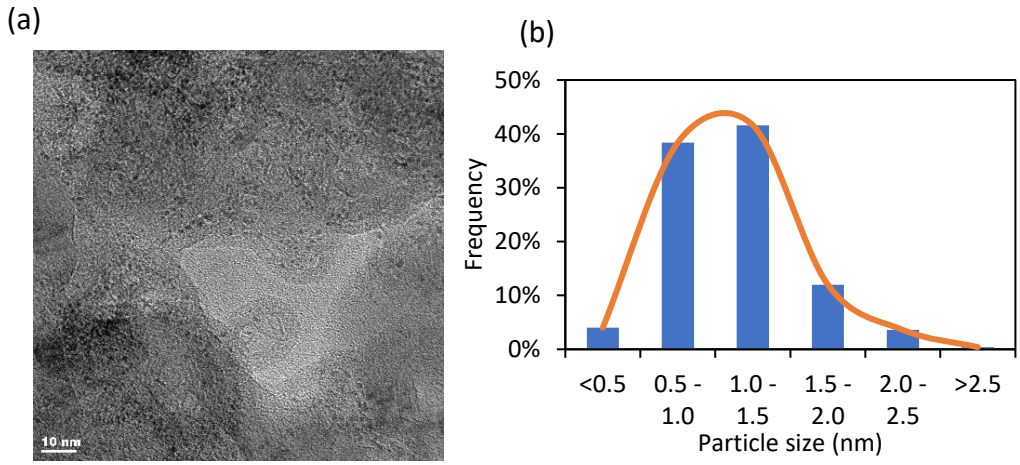

Figure 18 - (a) TEM images of Ir nanoparticles deposited on GV support b) the particle size distribution of Ir nanoparticles deposited onto the GV support before calcination

Due to the difference in mass and density, the Ir and IrOx were easily identified on the carbon support as the darker spots. Images in Figure 19 show that there was a slight increase in the particle size after the calcination and oxidation of the catalyst on GV. This was attributed to the agglomeration of the nanoparticles to form larger, more stable nanoparticles and the possible loss of support during calcination. The PSD in Figure 19 (b) shows that the average particle size increased to 5.9 nm with over 80% of the particles falling in the range of 4 – 9 nm. Results for the respective PSDs can be found in Appendix A.

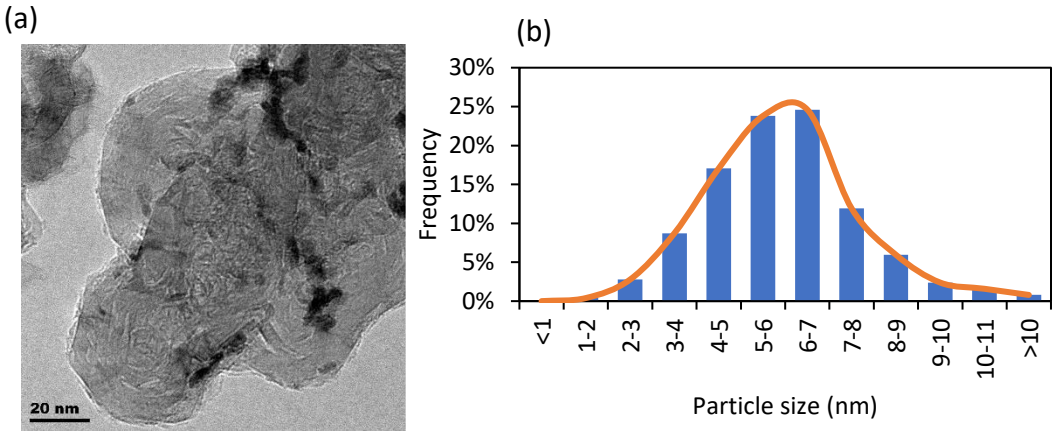

Figure 19 - a) TEM image of IrO_x nanoparticles supported on GV b) Particles size distribution of IrOx nanoparticles deposited on GV.

4.1.2. X-ray Photoelectric Spectroscopy (XPS)

All peak fittings were done using XPSPEAK 4.1 software. The aim of XPS analysis was to identify the oxidation states of the elements present in the IrO_x catalyst supported on GV. A wide scan was conducted at 50 eV which shows the responses from all compounds present in the sample, and can be found in Appendix B. This was followed by a narrow scan at 25 eV for each of the peaks of interest. XPS analysis was performed on Ir deposited onto GV before and after calcination. The Ir and O spectra were analysed; particularly their 4f and 1s orbitals respectively.

The Ir 4f peak consists of a doublet while the O 1s is a singlet. This is due to a phenomenon called spin orbital coupling (*j*); which is a combination of the electron's orbital angular momentum (*l*) and its spin angular momentum (*s*). Where *s* can be $\pm 1/2$ due to electron spin direction. Spin-orbital coupling (*j*) therefore results in the doublets that are present in the p, d and f orbitals. The s orbitals only give singlets because there is no orbital angular momentum as seen in Table 6.

Table 6 - Spin-orbit coupling j values.

Orbital	***l* values**	***j* values**
s	0	1/2
p	1	1/2 3/2
d	2	3/2 5/2
f	3	5/2 7/2

1. Ir 4f components

The peak parameters used for the Ir 4f fittings of the Ir and IrO_x deposited catalysts are shown in Table 7 which are in accordance with previous studies (Pfeifer *et al.*, 2016; Saveleva *et al.*, 2018)

Table 7 - Peak parameters for Ir 4f fitting of the Ir and IrO_x nanoparticles supported on GV.

	Before calcination			**After calcination**		
	BE (eV)	**FWHM (eV)**	**G/L**	**BE (eV)**	**FWHM (eV)**	**G/L**
Ir metallic	60.7	1.2	20	60.7	1.2	20
Ir 4+	61.5	1.5	20	61.5	1.6	20
Ir 3+	62.35	1.5	20	62.3	1.7	20
Ir 4+ sat 1	62.8	2.6	20	62.8	2.82	20
Ir 4+ sat 2	67.9	2	20	68.2	2	20
Ir 3+ sat	63.45	2.6	20	63.9	2.82	20

For all fittings a combination of Gaussian and Lorentzian fittings was used to accommodate various uncertainties inherent to XPS measurements. One factor is lifetime broadening. Due to the uncertainty principle of quantum mechanics, there will always be broadening of XPS peaks from the sample which gives the peak its Lorentzian contribution (Höchst, Steiner and Hüfner, 1980). The other uncertainty is due to instrumentation or experimental resolution. The x-ray emission process follows Heisenberg's uncertainty principle, so any monochromator used will reflect a small number of x-rays with slightly different energy. This gives the spectra its Gaussian contribution. Therefore, the combination of these two results in the overall peak broadening.

The background was fitted with a Shirley background to account for inelastic background scattering of electrons. These arise when an electron collides with another electron on its way out of the sample and losses some energy and results in the tail off after the peak being higher as the binding energy increases (Pfeifer *et al.*, 2016). The higher the intensity of the peak the larger the difference of the background on either side of the peak.

The Ir 4f peaks were fitted with satellite peaks for Ir $^{4+}$ and $^{3+}$ oxidation states. These states stem from energy lost to an electron excitation in the material. Sometimes complex rearrangements of remaining electrons after an electron has been ejected can cause some

energy to be absorbed resulting in a satellite peak. Iridium is one of the elements which has be found to exhibit such behaviour (Pfeifer *et al.*, 2016).

Figure 20 and Figure 21 show the results of the fittings for the Ir catalyst deposited onto GV before and after oxidation and calcination.

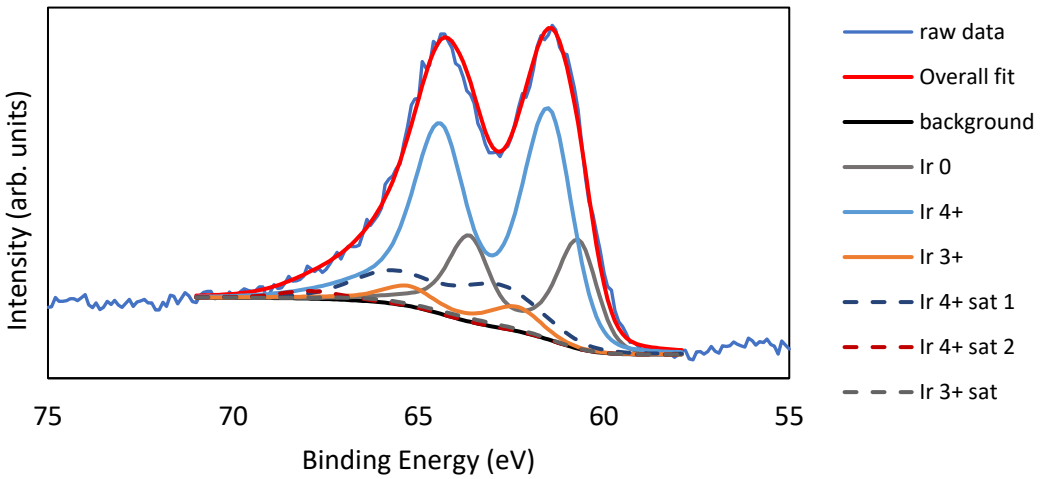

Figure 20 – XPS scan of Ir 4f spectra on supported Ir/GV catalyst before calcination.

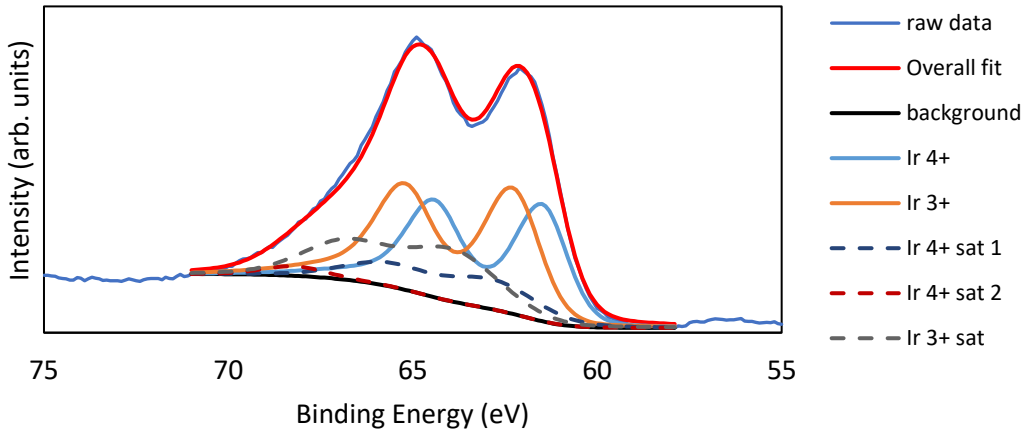

Figure 21 - XPS scan of Ir 4f spectra on supported IrO_x/GV catalyst after calcination.

Figure 22 gives the quantitative understanding of the oxidation states in the Ir 4f fittings. These calculations were based on the area beneath each curve. Although the polyol medium is highly reducing and meant to deposit metallic Ir particles, the deposited Ir was found to contain about 80% Ir^{4+} and Ir^{3+} with only 20% in the metallic form. This result was also observed in multiple studies which deposited Ir nanoparticles on varying supports via the polyol method (Allagui *et al.*, 2013; Choi *et al.*, 2014). It can therefore be suggested that the

oxidation of deposited Ir with a polyol method is a phenomenon inherent to this synthesis procedure. After calcination, all metallic Ir was oxidized to IrO_x in almost equal proportions of Ir^{4+} and Ir^{3+}.

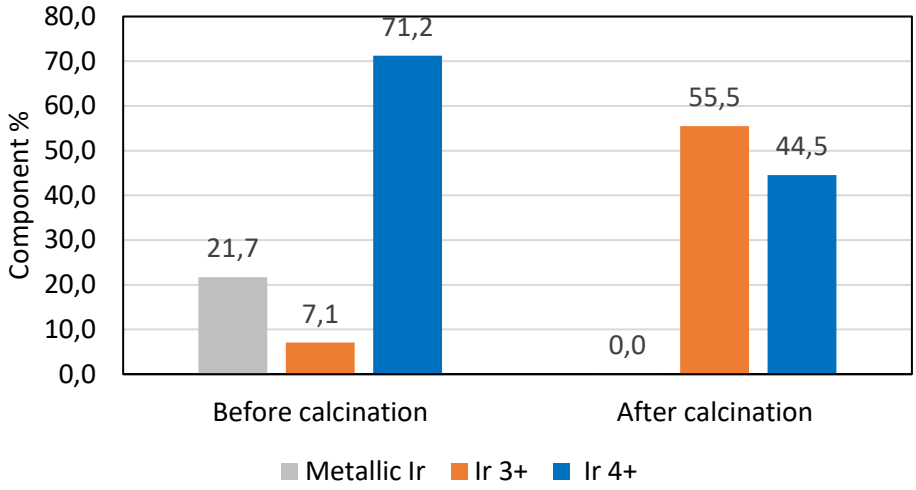

Figure 22 - Ratio of Ir oxidation states present in the synthesized IrO_x/GV catalyst before and after calcination.

2. O 1s components

The oxygen species considered in the fitting were lattice O, surface hydroxide groups as well as aromatic and aliphatic surface bonded carbon O. The fitting parameters used for the catalyst before and after calcination are shown in the Table 8 with the fitted spectra in Figure 23 and Figure 24 respectively.

Table 8 - Fitting parameters for the O 1s species on the synthesized catalyst before and after calcination.

	Before calcination			**After calcination**		
	BE (eV)	**FWHM (eV)**	**G/L**	**BE (eV)**	**FWHM (eV)**	**G/L**
Lattice O	530.1	2.2	20	530.2	2.03	20
M-OH and O-C=O*-C	531.8	2.2	20	531.9	2.03	20
C-O-C and C-OH aliphatic	532.9	2.2	20	532.9	2.03	20
C-O-C and C-OH aromatic	533.8	2.2	20	533.5	2.03	20

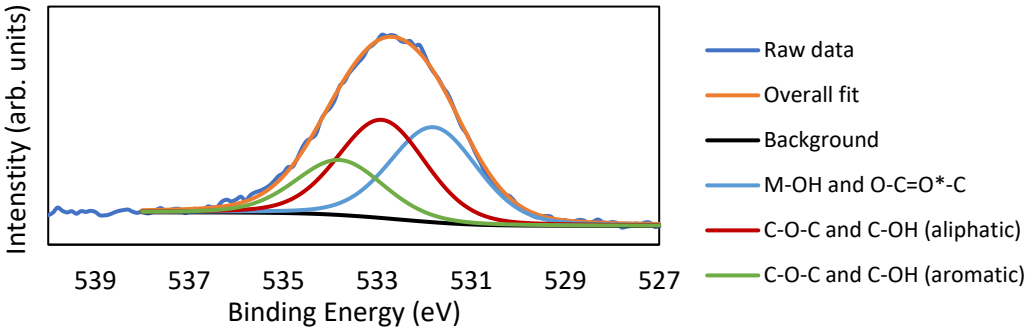

Figure 23 – XPS spectrum of O 1s spectra on synthesized Ir/GV catalyst before calcination.

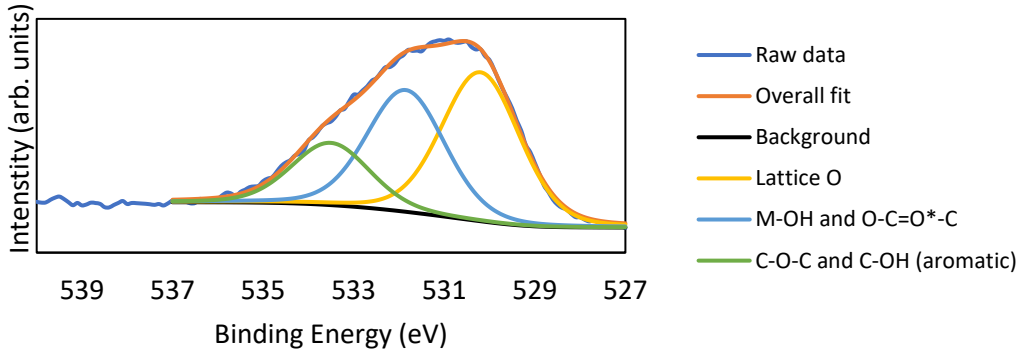

Figure 24 – XPS spectrum of O 1s spectra on synthesized IrO_x/GV catalyst after calcination.

The major difference between the Ir and IrO_x/GV spectra was the significant shift to lower binding energies after calcination. This revealed that the Ir^{4+} and Ir^{3+} oxidation states observed for the synthesised Ir/GV catalyst are a result of O adsorbed or bonded to the surface of the Ir nanoparticles, with no lattice O species. After calcination, crystalline IrO_x was formed as O was included in the lattice of the IrO_x.

Figure 25 provides a quantitative analysis of the oxygen species from the O 1s fittings. After calcination of Ir/GV, approximately 45% of the oxygen in the catalyst was in the IrO_x lattice while the rest remained as surface species. For the surface O species, it is difficult to quantify what fraction belongs to the Ir nanoparticles or the GV support, as XPS analysis can't differentiate between oxygen on the various respective surfaces.

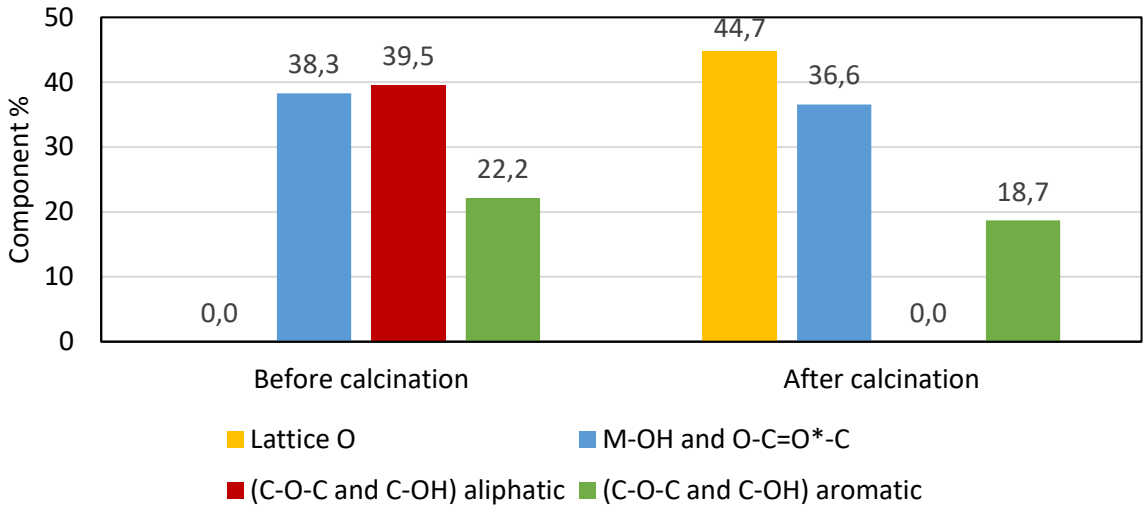

Figure 25 - Ratio of O species on the synthesized IrO_x/GV catalyst before and after calcination.

4.1.3. Thermogravimetric Analysis (TGA)

TGA was performed on the GV support before and after the deposition of the Ir catalyst to determine the thermal stability of the coated and uncoated support. Due to its graphitization, the support was expected to be more resistant to oxidation compared to non-gra phitized carbon blacks (Sadhasivam *et al.*, 2016). The TGA shown in Figure 26, confirmed that the GV is stable in air up to 600 °C before it begins to oxidise. After deposition of Ir, the thermogram showed that the mass loss began at significantly lower temperatures (approx. 350 °C) compared to bare GV. Due to the thermal stability of Ir(~4100 °C), the mass loss is ascribed to carbon oxidation.

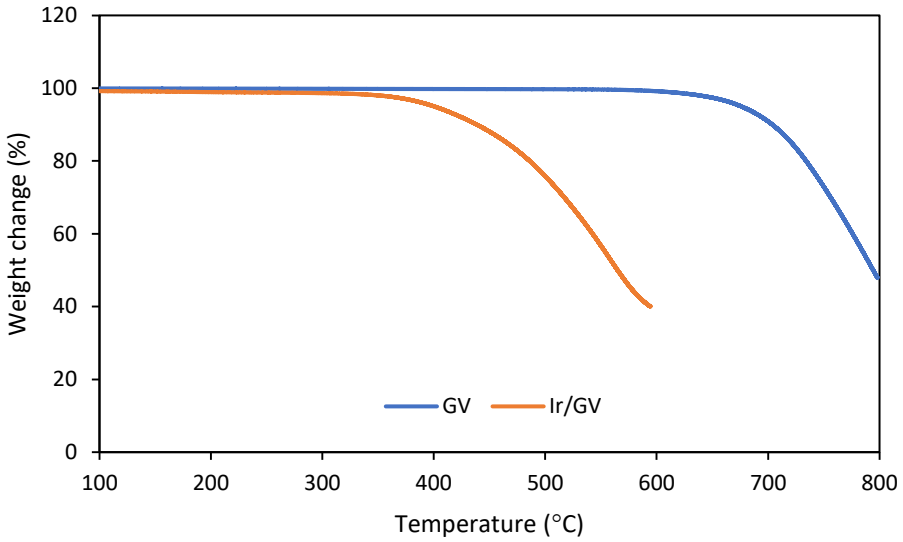

Figure 26 - TGA of bare graphitized Vulcan (GV) and Ir/GV.

TGA was also performed to determine the final loading of IrO_x on the GV support (Figure 27). It is assumed that the carbon support is completely oxidised and that the final mass of IrO_x 56.29 wt%.

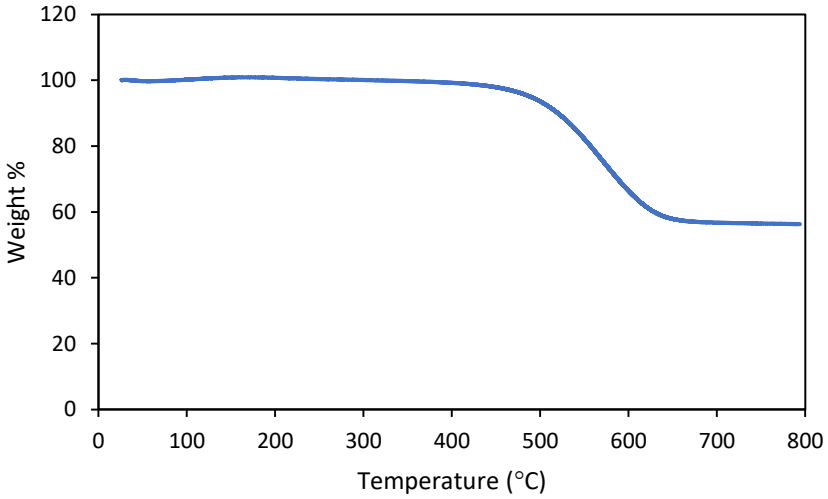

Figure 27 - TGA of IrO_x supported on GV to determine the IrO_x loading.

4.1.4. Electron dispersive X-ray Spectroscopy (EDX)

The EDX analysis given in Table 9 was performed to confirm the loading of the IrO_x supported on GV, obtained from the TGA.

Table 9 – Mean EDX data for synthesized IrO_x supported on GV catalyst.

Element	**C**	**O**	**Ir**
Composition (wt %)	43.39	12.32	44.29

The results gave a combined loading of IrO_x in the sample as 56.61 wt% which agreed with TGA results. Therefore, the loading of Ir and IrO_x in the catalyst was taken as 44 wt% and 56 wt% respectively.

4.1.5. Raman Spectroscopy

The Raman spectra of the bare and catalyst coated GV support is shown in Figure 28. The goal was to determine whether the deposition of IrO_x affected the electronic structure of the support.

Raman spectroscopy allows one to characterize the degree of graphitization and disordered nature of carbon materials. This is done by looking at the two characteristic peaks centred around 1530 cm^{-1} (G-peak) and 1350 cm^{-1} (D-peak) (Zhang *et al.*, 2000; Tai *et al.*, 2006). The intensities of these G-peaks and D-peaks are generally noted as I_D and I_G respectively. This analysis was previously thought to not give any information on the type of carbon bonding; either sp^3 or $sp^{2,}$, however a study by Tai *et al.*, (2006) found that the I_D/I_G ratio correlated to the sp^2/sp^3 ratio in diamond-like carbon films. Therefore, the intensities of the peaks present can give an indication to the type of carbon bonding present in a sample (whether sp^3 or sp^2).

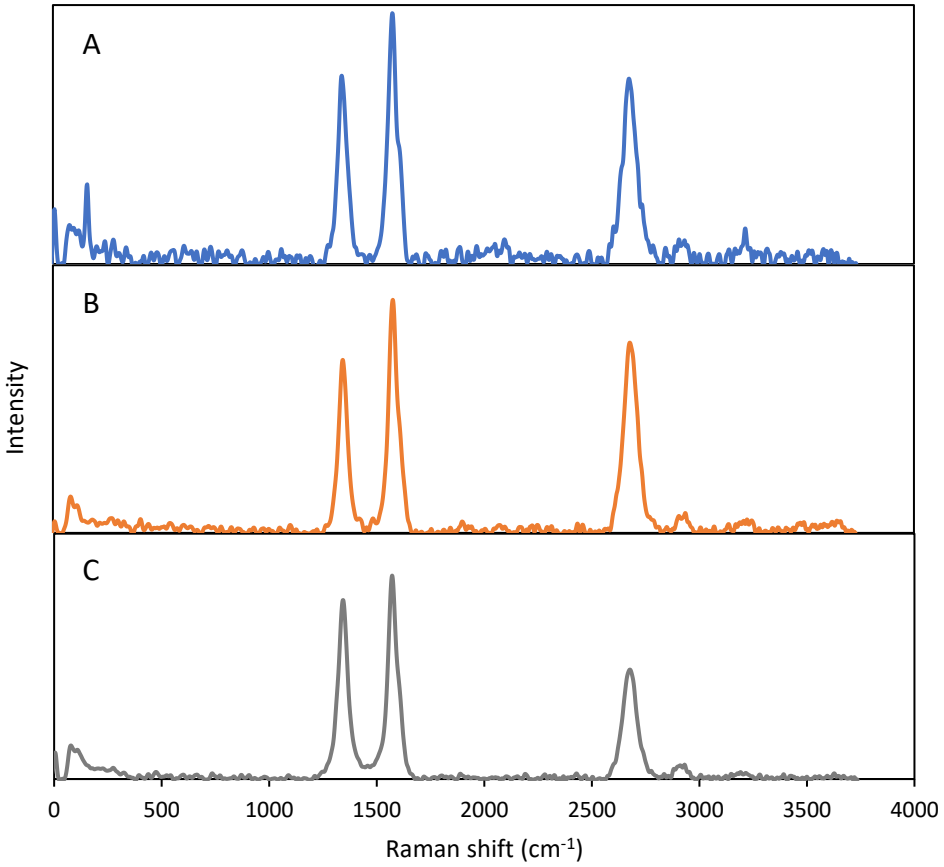

Figure 28 - Raman spectra of (A) GV supports, (B) Ir deposited on GV before calcination (C) IrOx supported on GV.

From the spectra, the I_D/I_G ratio between the two peaks did not change before and after Ir deposition and was found to be approximately 0.7. After calcination to IrO_x, the ratio increased slightly to approximately 0.8 which could have been due to the oxidation of GV support as shown in the TGA results. The GV support contains a significant amount of sp^3 carbon which means the GV support is partially graphitized. Another similarity between the two scans is that the peak at 2700 cm^{-1} is constant in both samples with similar intensities. This peak is commonly known as the G' or 2D peak and is characteristic of graphitic compounds (Hodkiewicz, 2010). Therefore, the graphitic nature of the carbon support was unaffected by the deposition of Ir.

4.2. Analysis of Synthesis procedure

This section evaluates the efficiency of this technique and possible ways for improvement of the OER catalyst synthesis. Table 10 shows the mass balance and yield data from the synthesis which reveals that there was significant mass loss during the synthesis.

Table 10 - Mass balance of the IrO_x/GV catalyst synthesis procedure.

	Value	**Units**
GV added	535	mg
$H_2IrCl_6 \cdot 6H_2O$ added	540	mg
Expected final mass	805	mg
Actual final mass after calcination	433	mg
Expected final Ir loading	33	wt %
Final IrO_x loading by TGA	56	wt %

Based on the characterization results presented, it is evident that the deposited Ir on the GV accelerates the oxidation of the support, most likely from the sp^2 and sp^3 surface carbon atoms which are more susceptible to oxidation compared to highly crystalline bulk carbon atoms. A possible solution to reduce carbon mass loss is to use a carbon support with a higher degree of graphitization to minimize the oxidation of the support.

In summary IrO_x supported on GV was successfully synthesized using microwave assisted polyol deposition. This technique produced Ir nanoparticles within a very narrow size range which then increased after calcination. The final catalyst had a loading of approximately 60 wt% with IrO_x nanoparticles containing both Ir^{4+} and Ir^{3+} oxidation states

5. Electrochemical Characterization of IrOx/GV

This chapter details the electrochemical characterization for the synthesized IrO_x/GV catalyst with respect to its activity and durability towards the oxygen evolution reaction (OER). The activity and durability of the supported catalyst is compared to two commercial catalysts; Iridium on Vulcan (Ir/V) obtained from the FuelCell Store® and iridium oxide on titanium dioxide (IrO_x/TiO_2) from Umicore®. The OER activity and durability of the synthesized catalyst is indicative of the reversal tolerant ability of the MEA made with the catalyst in the anode layer.

5.1. Electrochemical characterization of the IrO_x/GV

To ensure reliable and good results, all experiments were conducted in triplicates. A typical beginning of life cyclic voltammetry (CV) for the synthesized IrO_x/GV is show in Figure 29. This was done to gain insight to the surface properties and oxidation states on the catalyst

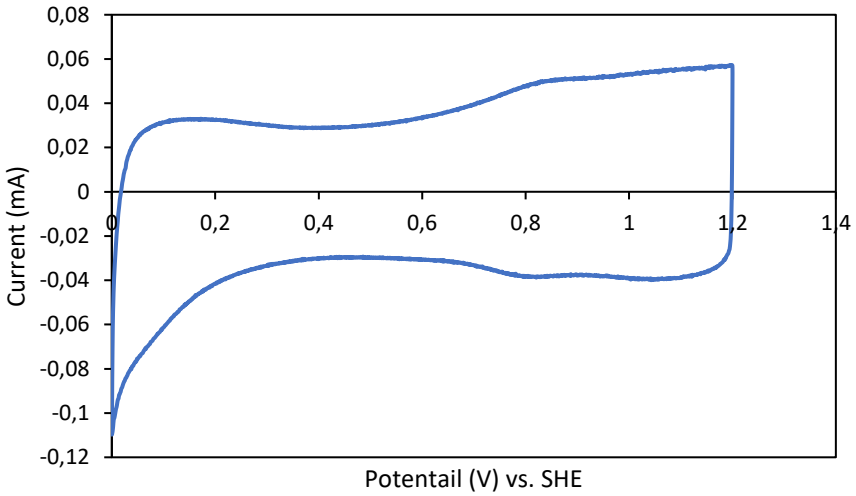

Figure 29 - Cyclic voltammogram of IrO_x on GV at 20 mV/s in 0.1 M $HClO_4$ under Ar saturation.

The voltammogram shows two peaks at approximately 0.05 V and 0.8 V. A study by Jang et al., (2013) identified the various oxidation states of Ir present and correlated them to the peaks present in the CV. The peaks are related to hydrogen adsorption and the Ir(III)/Ir(IV) redox couple respectively (Jang, Hwang and Tak, 2013). These peaks confirm the XPS results presented in section 4.2.2 of the observed Ir^{3+} and Ir^{4+} oxidation states present in the catalyst.

Silva, Perini and Ticianelli, (2017) synthesized amorphous IrO_x and subjected it to various temperatures to obtain varying degrees of crystallinity. They concluded that increasing the temperature increases the crystallinity of the IrO_x which was confirmed by XRD, TEM and electrochemical analysis. Their study showed that crystalline IrO_x can be determined by its CV which exhibit broad less defined peaks compared to the amorphous IrOx. In this current work, similar peak structures were found with the synthesised crystalline IrO_x supported GV.

When benchmarked against the two commercial catalysts (Figure 30), the Ir/V catalyst had a more pronounced peak at ~0.05 V. This is due to the more metallic nature of Ir/V, capable of catalysing hydrogen adsorption and desorption. The IrO_2/TiO_2 catalyst had the lowest charging current of the three which was attributed to the low conductivity of the supported catalyst due to TiO_2 being a semiconductor. However, it exhibited a voltammogram similar to that of the synthesized IrO_x/GV catalyst indicating highly crystallinity.

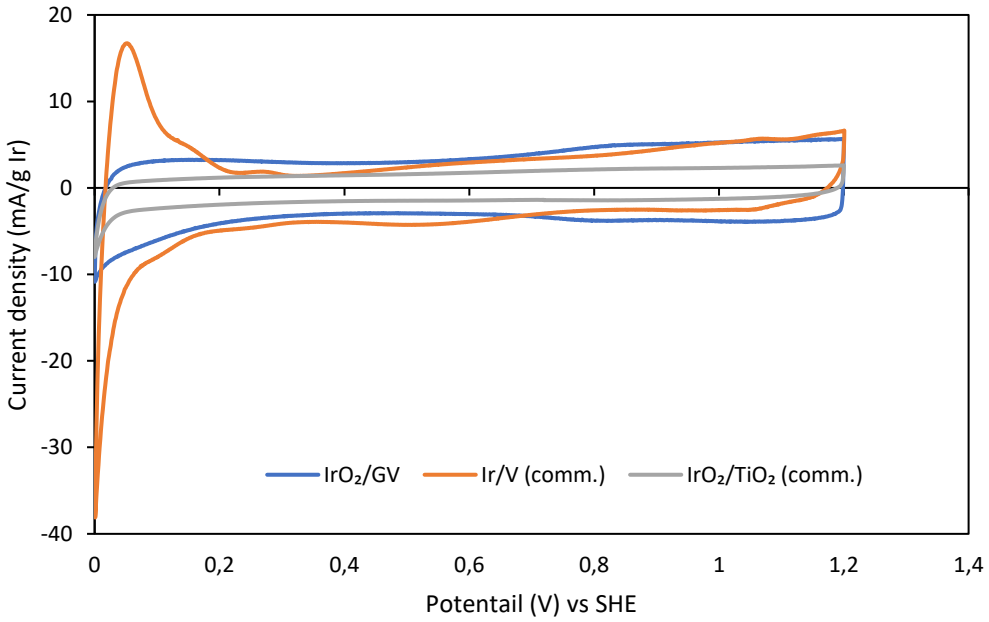

Figure 30 - Mass normalized cyclic voltammograms of synthesized IrO_x/GV and commercial Ir/V and IrO_x/TiO_2 at 20 mV/s in 0.1 M $HClO_4$ under Ar saturation.

5.2. Electrochemical activity of IrO_x/GV

The electrochemical activity of the catalyst was measured by performing cyclic voltammograms at higher potentials (1.2 V – 1.65 V) were the OER reaction occurs. At these

high potentials, the rate of O_2 bubble formation increases, causing a transient state on the electrode surface and noise in the measurements (Alia *et al.*, 2016). To mitigate the impact of bubble formation, the electrode was spun at 1600 rpm and the entire cell tilted to allow easy removal of the bubbles. The CVs were measured at 5 mV/s to minimise the capacitive currents generated which add uncertainty to the measured activity. To further eliminate the capacitive currents which occur on the surface of the electrode, the forward and backward sweeps of the CV were averaged. The oxidative sweep will show an increase with capacitive charging and the reduction, or back sweep, will have a similar, yet opposite negative increase due to the charging current. Once averaged, this was corrected for the solution resistance by EIS analysis, of which the resultant voltammograms are show in Figure 31.

For comparison between catalysts, the activity is determined at a specific potential, generally 1.55 V or 1.525 V. For all activity measurements, the current was measured at 1.55 V.

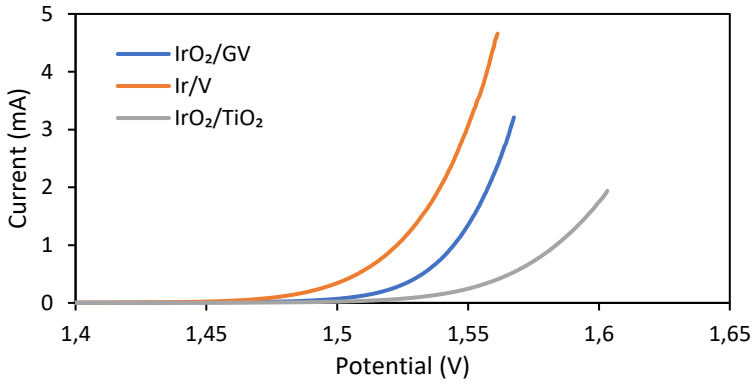

Figure 31 – Averaged, EIS corrected CVs for activity measurements of synthesized IrO_x/GV, and commercial Ir/V and IrO_x/TiO_2 at 5 mV/s in 0.1 M $HClO_4$ under Ar saturation.

The current measured at 1.55 V was normalized for the respective masses of Ir in the catalysts and the volume of ink deposited on the glassy carbon electrode, of which the results can be found in Table 11. These results show that the Ir/V catalyst is the most active followed by the synthesized IrO_x/GV and the commercial IrO_x/TiO_2 respectively. This corresponds with the literature study detailed in section 2.7 where metallic Ir has been found to be more active towards the OER than its respective oxide state. Comparing the two oxide catalysts, the lower activity observed by the IrO_x/TiO_2 catalyst can be partly attributed to the lower conductivity of the TiO_2 support compared to the GV support which is highly conductive (Antolini and Gonzalez, 2009).

Table 11 - Loading and mass activity of synthesized IrO_x/GV and commercial Ir/V and IrO_2/TiO_2 catalysts.

	Ir loading (wt %)	Mass activity at 1.55 V (A/ mg Ir)
Synthesized IrO_x/GV	44	0.141
Commercial Ir/V (FuelCell Store®)	40	0.342
Commercial IrO_x/TiO_2 (Umicore®)	74	0.015

5.3. Electrochemical surface area (ECSA) of IrO_x/GV

The ECSA of the catalyst is the area available on the catalyst surface to promote the OER electrochemical reaction. This is generally smaller compared to the overall surface area of the supported catalyst obtained through BET analysis as the GV support does not take part in the OER. The ECSA was calculated from the electrochemical capacitance of the catalyst surface by measuring the non-Faradaic capacitive current associated with double layer charging. The non-Faradaic potential region is the region associated with the storage of charge on the catalyst surface whereas the Faradaic region is associated with charge transfer between the electrolyte and catalyst (i.e. an electrochemical reaction) (Biesheuvel and Dykstra, 2018). From Figure 29, the non-Faradaic region was taken to be between 0.4 V and 0.55 V.

The CVs taken in the non-Faradaic region at varying scan rates, used for the ECSA calculation are shown in Figure 32.

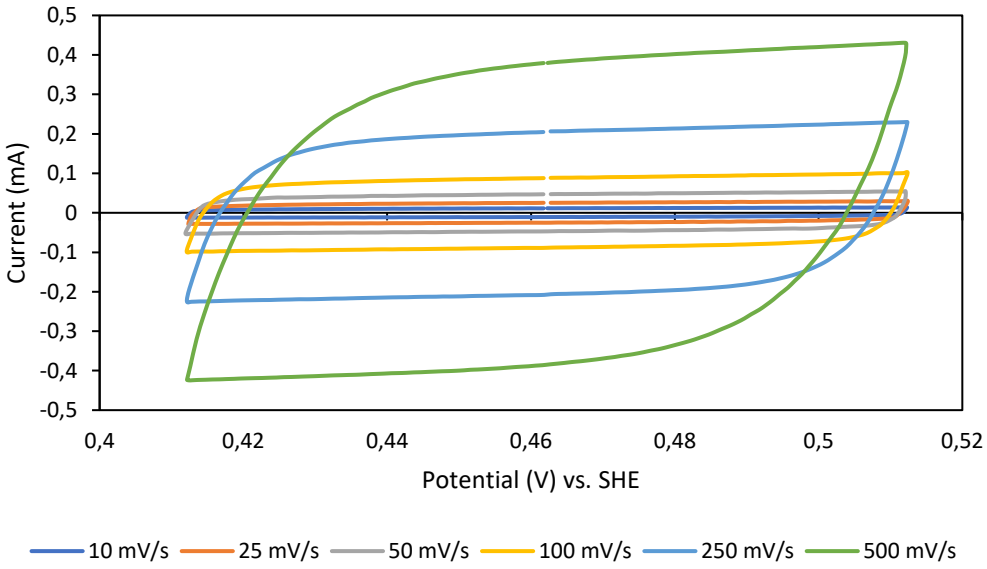

Figure 32 - Cyclic voltammogram of IrO_x/GV determined in the non-Faradaic region at various scan rates.

The charging current was taken at 0.46 V and plotted versus the scan rate used as shown in Figure 33.

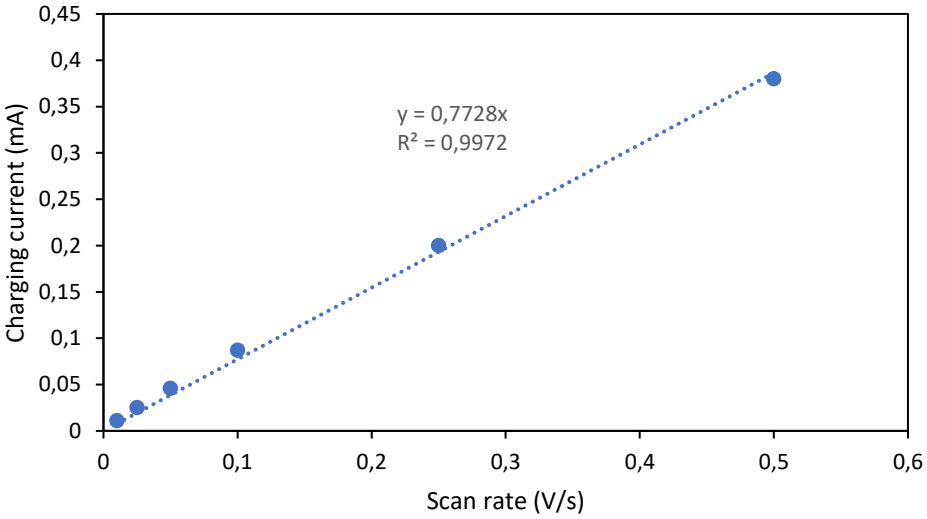

Figure 33 - Plot of scan rate vs charging current at 0.46 V used to determine ECSA.

Using the equation 5.1 and Figure 33, the double layer capacitance was calculated as the gradient of the line.

$$i_c = vC_{DL} \qquad \textit{(Eq. 5.1)}$$

v = scan rate, i_c = charging current, C_{DL} = Double layer capacitance

Gradient = C_{DL} = 0.7728 mF

Given that the specific capacitance (C_s) of IrO_2 has been estimated to be approximately 0.035 mF/cm^2 (Shukla, Sampath and Vijayamohanan, 2000), the mass normalized ECSA was calculated as shown below and was found to be 31.25 m^2/g Ir.

$$ECSA = \frac{C_{DL}}{C_s} = \frac{0.7728\ mF}{0.035\ mF/cm^2} = 3.85\ cm^2$$

$$\therefore mass\ normalized\ ECSA = \frac{Surface\ area}{Mass\ of\ Ir\ on\ electrode}$$

$$= \frac{3.85\ \times 10^{-4}\ m^2}{0.022\ mg^{(1)}\ \times 44\%\ g\ Ir^{(2)}\ \times 1000} = 39.77\ m^2/g\ Ir$$

(1) 0.022 is mass of catalyst deposited on the glassy carbon electrode in mg.
(2) 44% is the Ir loading on the catalyst from EDX analysis

This ECSA value determined is consistent with other ECSA values obtained from literature on Ir based catalysts (Alia *et al.*, 2016). Table 12 shows the comparison of the ECSA of the synthesized and commercial catalyst obtained from the suppliers. The results are in line with the activity measurements where the catalyst with the highest ECSA (Ir/V) exhibits the highest performance.

Table 12 - Comparison of ECSA of synthesized catalyst and commercial catalysts.

	ECSA (m^2/g Ir)
Synthesized IrO_x/GV	40
Commercial Ir/V (FuelCell Store®)	60
Commercial IrO_x/TiO_2 (Umicore®)	15

While a higher mass activity signifies the catalysts ability to promote the desired OER reaction, its durability must also be analysed as stability of the catalyst is key parameter for practical use.

5.4. Electrochemical durability of IrO_x/GV

The electrochemical durability of the supported catalyst is measured by its ability to retain its activity after being cycled in a potential range for an extended period. This is important for its use in an anode of the MEA, as the OER catalyst will be subjected to a wide range of potentials during its operation. Therefore, its ability to maintain its performance over time will play a vital role in the MEA's RTA capabilities. The catalyst was subjected to 5000 potential cycles between 0.6 V and 1.6 V. Figure 34 shows the resulting activity voltammograms taken during the durability study of IrO_x/GV with increasing number of cycles. There was a progressive decrease in activity and a 51% decrease after 5000 cycles.

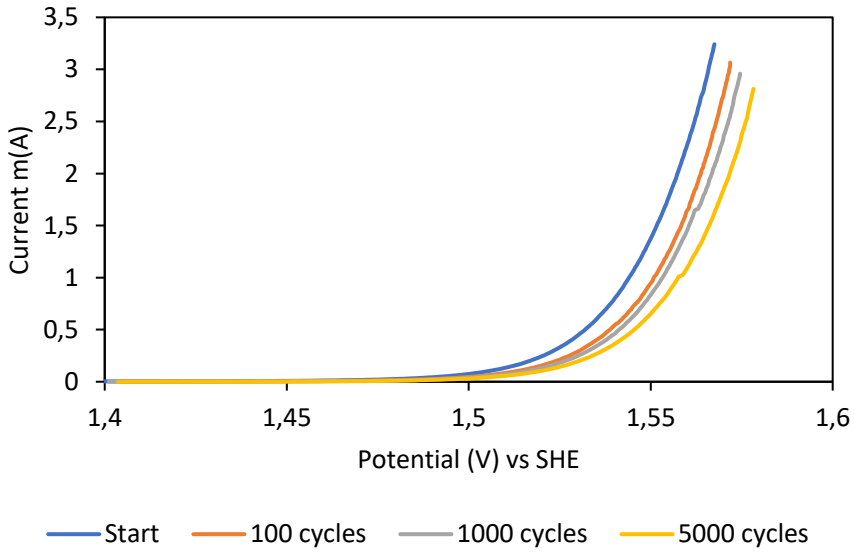

Figure 34 – Corrected voltammograms illustrating the electrochemical activity for IrO_x/GV determined by cyclic voltammograms at increasing cycle intervals of the durability study.

The durability study was also conducted on the two commercial catalysts and the results after 5000 cycles are shown in the Table 13

Table 13 - Durability comparison between synthesized OER catalyst and commercial catalysts.

	Initial Activity (A/ mg Ir)	**Final Activity (A/ mg Ir)**	**Activity loss (%)**
Synthesized IrO_x/GV	0.141	0.070	51
Commercial Ir/V (FuelCell Store®)	0.342	0.095	72
Commercial IrO_x/TiO_2 (Umicore®)	0.015	0.009	44

The decreasing mass activity of the various Ir supported catalysts was plotted as a function of the number of durability cycles in Figure 35. The major mass loss occurred during the first 1000 cycles, thereafter the rate of degradation reduced significantly. Alia *et al.*, (2016) performed similar degradation studies on Ir based catalysts attributed the loss of mass activity to particle agglomeration and ripening. Based on the dissolution mechanism presented in Section 2.7.1., a small portion of performance loss could also be due to Ir^{3+} dissolution. This activity loss was found to be larger in higher surface area catalysts such as the Ir/V (~60 m^2/g Ir) compared to the low surface area IrO_x/TiO_2 catalyst (~15 m^2/g Ir) as they are more prone to these effects. Furthermore, these results are in line with the literature discussion presented in section 2.6.2, where metallic Ir catalysts were found to be more active but had very low durability compared to its oxide catalysts.

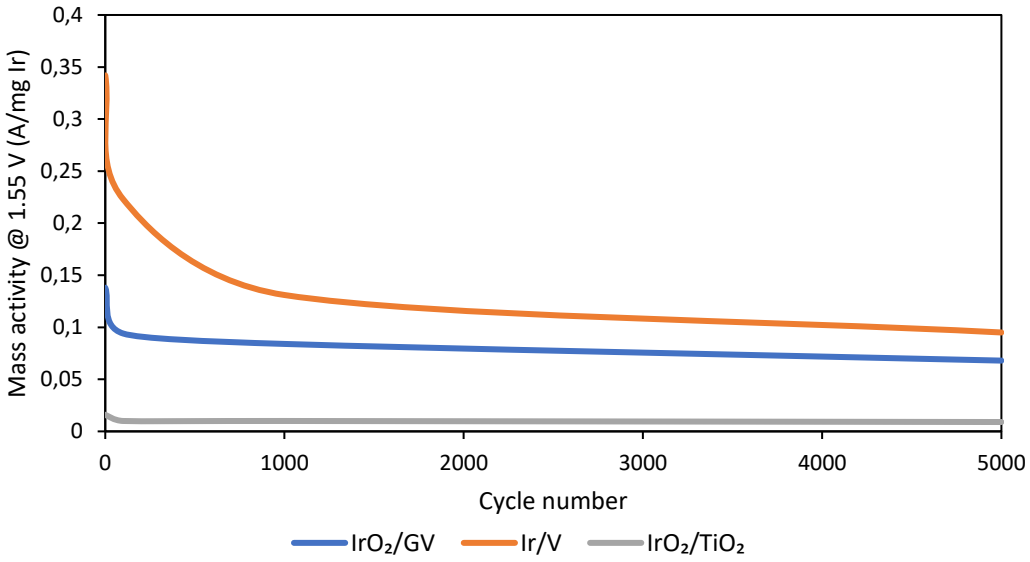

Figure 35 – Electrochemical mass activity vs number of cycles obtained during the durability study of IrO_x/GV, Ir/V and IrO_x/TiO_2.

The synthesized IrO_x/GV catalyst had a mass activity approximately 9 times higher than the commercial IrO_x/TiO_2 catalyst while maintaining a comparable degree of durability. It has been found that Titania supported catalyst have very strong metal-support interactions which provide its high stability, however, Titania is a semi-conductive material (Sakai *et al.*, 2004) which decreases its electrochemical activity. IrO_x/GV exhibited 29% higher durability than the commercial Ir/V thereby giving a good balance between electrochemical activity and durability amongst the benchmarks studied.

6. MEA In-situ Testing and Characterization

This chapter presents in situ performance and reversal tolerance of the MEAs made using the synthesized OER catalyst (IrO_x/GV) in the anode. The MEAs were evaluated electrochemically in a single cell Fuelcon test station using polarization curves, EIS, hydrogen crossover and cyclic voltammetry. The chapter also present physical characterization of the MEAs before and after testing to illustrate the impact of cell reversal on the MEA.

6.1. Electrochemical Analysis

6.1.1. Performance evaluation

The performance polarization curves of the MEAs with supported OER catalyst (at 0.1 mg Ir /cm^2 (1:1 Pt/Ir) and 0.06 mg Ir/cm^2 (1:0.6 Pt/Ir)) was measured under the 3 conditions (high, mid and low humidity) as described in Chapter 3.5. Figure 36 shows the performance curves of the IrO_x/GV MEA compared to a commercial MEA benchmark (40 wt% Pt supported on carbon; no OER catalyst) tested at the same humidity conditions. The MEAs with OER catalysts maintained similar OCV, activation and ohmic loss profiles as the commercial MEA indicating that the OER catalyst would not affect the ORR and HOR reactions during normal operation. A considerable decrease in performance was observed in Figure 36 (F) between 0.6 – 1.4 V, which is likely due to mass transport or back pressure deviations of the gases.

The polarization cures for the high and low Ir loading MEAs were compared independently to determine which humidity condition produced the best performance (Appendix C). For both the high and low Ir loadings, operating the MEA at higher humidity conditions exhibited better performance. This was expected as the MEA needs to be well hydrated to maintain high proton conductivity (Wang *et al.*, 2008).

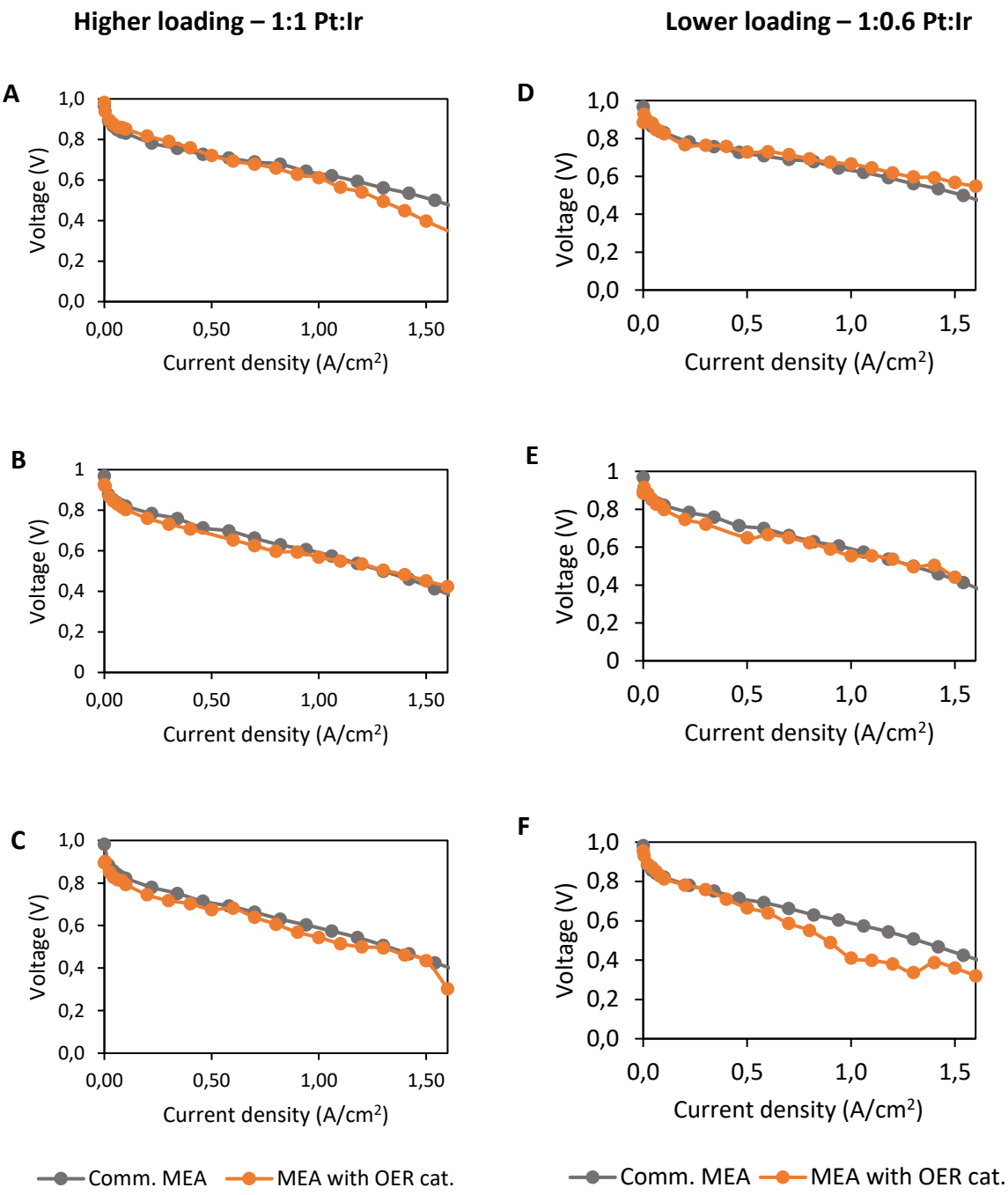

Figure 36 - Performance polarization curves of commercial MEA (grey) and MEAs with IrO_x/GV catalyst (orange) at high-, mid- and low-humidity conditions for higher loading MEAs in (A), (B) and (C) and lower loading MEAs in (D), (E) and (F) respectively.

6.1.2. Polarization curves from potential reversal AST

Potential reversal AST was performed using two protocols; an indefinite long hold test and multiple pulse starvation events. The former displays the MEAs ability to withstand an extended period of starvation while the latter demonstrates the MEAs ability to recover after starvation. All MEAs at each loading were subjected to 7 rounds of testing to ensure consistency in the results.

1. The single hold test event

The results of the long hold test are shown in Figure 37. Once the H_2 gas is switched to N_2, there is a short delay of about 1-2 min before the overall cell potential reverses to negative potentials. This is due to residual H_2 in the gas lines. In Figure 11, it was shown that once the potential is reversed, the OER catalyst can clamp the potential at approximately -0.6 V which is where water oxidation occurs. By maintaining the potential in the water oxidation region, severe carbon corrosion is avoided (potentials less than -1.0 V), although oxidation of the carbon support may still occur at a much slower rate. Figure 37 shows that the presence of the IrO_x/GV catalyst maintained the potential between -0.6 V and -0.8 V for about 15 hours for both loadings of Ir. This is significantly longer compared to a commercial MEA with no OER catalyst which fell below -1.0 V in 200 s. The addition the IrO_x/GV catalyst resulted in an MEA which exhibited superior durability during cell reversal when compared to previous studies. Ralph, Hudson and Wilkinson, (2006) tested RuO_2-IrO_2 OER catalysts in several anode configurations, the best of which took 26 hours to reach -2.0 V. However, the cell using the RuO_2-IrO_2 OER catalysts was not stable and spent majority of its time below -1.0 V which would result in severe degradation. Therefore, the results presented in this study show good performance as the cell potentials were kept in the water electrolysis region for the entire duration of the test.

Both loadings of the synthesized OER catalyst in the MEA were successful in exhibiting reversal tolerance in an MEA AST, thus improving its durability by reducing carbon corrosion.

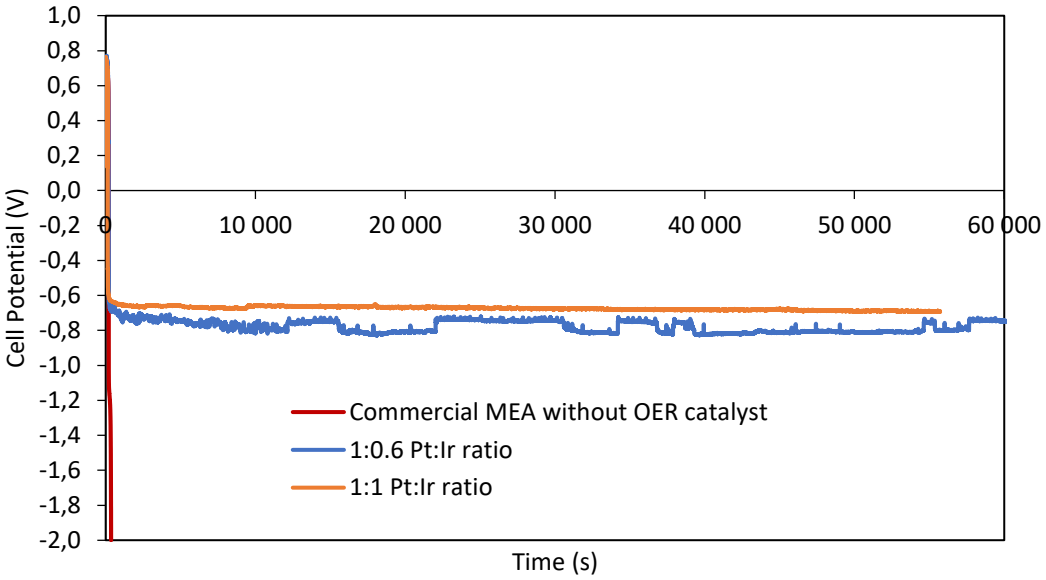

Figure 37 - Cell potentials in long hold test for commercial MEA, and MEAs with 1:1 and 1:0.6 Pt:Ir loadings.

2. The pulsed event tests

For this analysis, the MEAs were starved for a set period, thereafter H_2 gas was fed back to the MEA during a set recovery time. To analyse the effects of repeated starvation, polarization curves were taken after each starvation event. Figure 38 is an example of the voltage response curves for a pulsed cell reversal test in which the MEA was starved for 5 min and then recovered for 10 minutes. The resulting polarization curves after each fuel starvation event is shown in Figure 39. All other polarization and voltage response curves for the other reversal tests are included in Appendix D while a summary of the cell reversal results is presented in Table 14 and Table 15. The results show that the addition of the OER catalyst consistently held the potential in the water electrolysis region through repeated starvation events and for several variations in time. The polarization curves, however, showed a 2 – 18% decrease in performance with the largest difference generally being after the first reversal event.

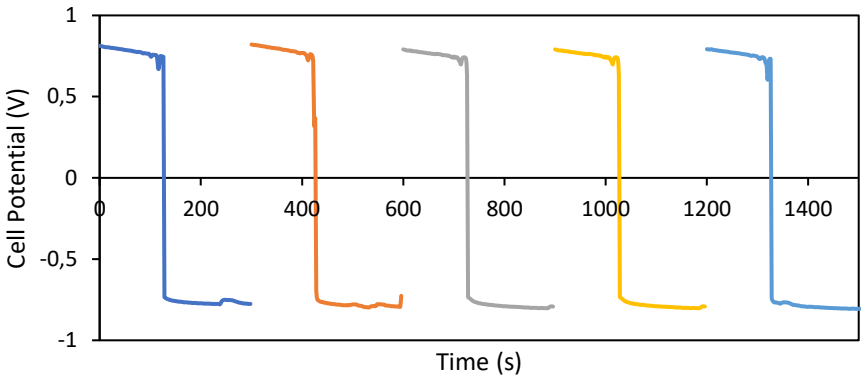

Figure 38 - Cell potential vs time for 5 potential reversal events in which the modified anode experiences 5 min of starvation and 10 min of recovery.

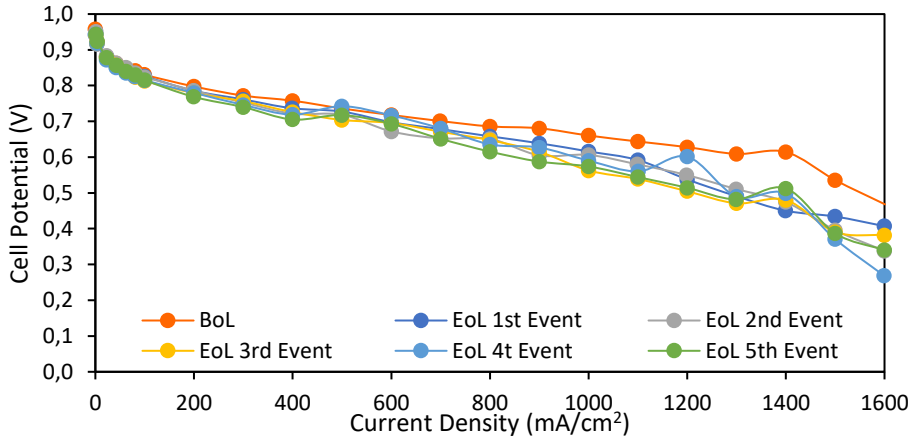

Figure 39 - Polarization curves of the modified anode after each of the 5 potential reversal events for the 5 min starvation and 10 min recovery time.

A quantitative analysis was done by measuring the decrease in cell potential at two current densities (400 mA and 1200 mA; where the ohmic and mass transport losses dominate respectively) after all starvation events relative to the BoL voltage. The results are summarised in Table 14 and Table 15.

Table 14 - Performance summary of MEAs after reversal testing for the IrO_x/GV 1:1 Pt:Ir ratio.

			% drop in cell potential	
Reversal time	Recovery time	no. of reversal events	400 mA	1200 mA
5	10	5	7	18.2
5	30	5	3.2	8.6
10	10	5	1.5	9.1
10	30	5	5.3	15
30	10	2	4.9	13.4
30	30	2	4.8	8.8

Table 15 - Performance summary of MEAs after reversal testing for the IrO_x/GV 1:0.6 Pt:Ir ratio.

			% drop in cell potential	
Reversal time	Recovery time	no. of reversal events	400 mA	1200 mA
5	10	5	18	49.9
5	30	5	4.9	27.9
10	10	5	1.8	33.5
10	30	5	10.2	14
30	10	2	12.2	37
30	30	2	9.9	17.2

Although the cell potential was held between -0.6 V to -0.8 V in all ASTs performed, the performance of the MEAs with higher Ir content had a lower drop in performance at both low and high current densities compared to the MEAs with lower Ir loading. The drop-in performance for lower Ir loaded MEAs is likely due to higher rates of carbon support degradation. Thereby indicating that the amount of OER catalyst is insufficient to promote water electrolysis to an extent in which it completely inhibits carbon degradation.

The open circuit voltage (OCV) was relatively stable after successive periods of fuel starvation in every AST which indicated that activation losses were not increased. This implies the resistances related to the kinetics of the HOR and ORR were unaffected by the fuel starvation events. The loss in performance, most noticeable in the ohmic and mass transport regions, could be due to ionic, electronic and contact resistances in the catalyst and membrane layers (Gharehpetian and Mousavi Agah, 2017). Furthermore, in almost all starvation tests, a higher performance drop was observed for the 10 min recovery times compared to the 30 min, which was especially apparent at higher current densities. This could be because the OER consumes water, therefore increasing recovery time allows for greater rehydration of the catalyst layers, which subsequently reduces degradation in successive starvation events as more water is present for the OER.

The polarization and voltage response curves give the MEA's performance response to fuel starvation but does not provide information to the physical changes which may occur within the MEA. The subsequent analysis therefore provides more insight to the specific causes of this performance drop. All analysis presented from this point on is categorized according to the potential reversal time (i.e. 5, 10, 30 or long hold).

6.1.3. Electrochemical Impedance Spectroscopy (EIS)

EIS was taken before (BoL) and after the AST tests (EoL). Figure 40 shows the Nyquist plots obtained for both Ir loaded MEAs at 0.2 A/cm^2, which is in the activation regime of the polarization curve.

Due to the sluggish kinetics of the ORR, the polarization resistances of the cathode outweigh that of the anode (Asghari, Mokmeli and Samavati, 2010) which is seen as a larger semi-circle in the Nyquist plots for the cathode accompanied by a smaller one to the left (at higher frequencies) for the anode (Section 2.10.2). No visible peak could be isolated for the anode charge transfer resistance, implying that the cathode charge transfer resistances dominated. The charge transfer resistance, determined by the diameter of the semi-circular plots, remained reasonably constant, except for the higher Ir-loaded MEA during the 10 min starvation event (Figure 40 (B)) which showed a decrease. This MEA was compressed several times, due to intermittent power cuts, and it is believed that the repeated compression may have reduced the thickness of the catalyst layer, which according to Travassos and Rangel, (2010), could reduce the charge transfer resistance.

The MEAs showed a significant increase in the ohmic resistance, which could be due to an increase in the membrane resistance and ionomer degradation in both the catalyst and membrane layers (Zhu, Payne and Tatarchuk, 2007). This is seen as the first intercept of the curves with the x-axis shifts to the right. Previous studies found that potential reversal in MEAs (without OER catalysts) does not increase the ohmic resistance but significantly increases the charge transfer resistance (Kang *et al.*, 2010). This is likely due to the loss of catalyst from carbon corrosion. However, addition of the IrO_x/GV OER catalyst did not increase the charge transfer resistance yet suffered an increase in ohmic resistance. One possibility for this is the dehydration of the membrane due to the OER consuming water therefore reducing the membranes ability to conduct protons.

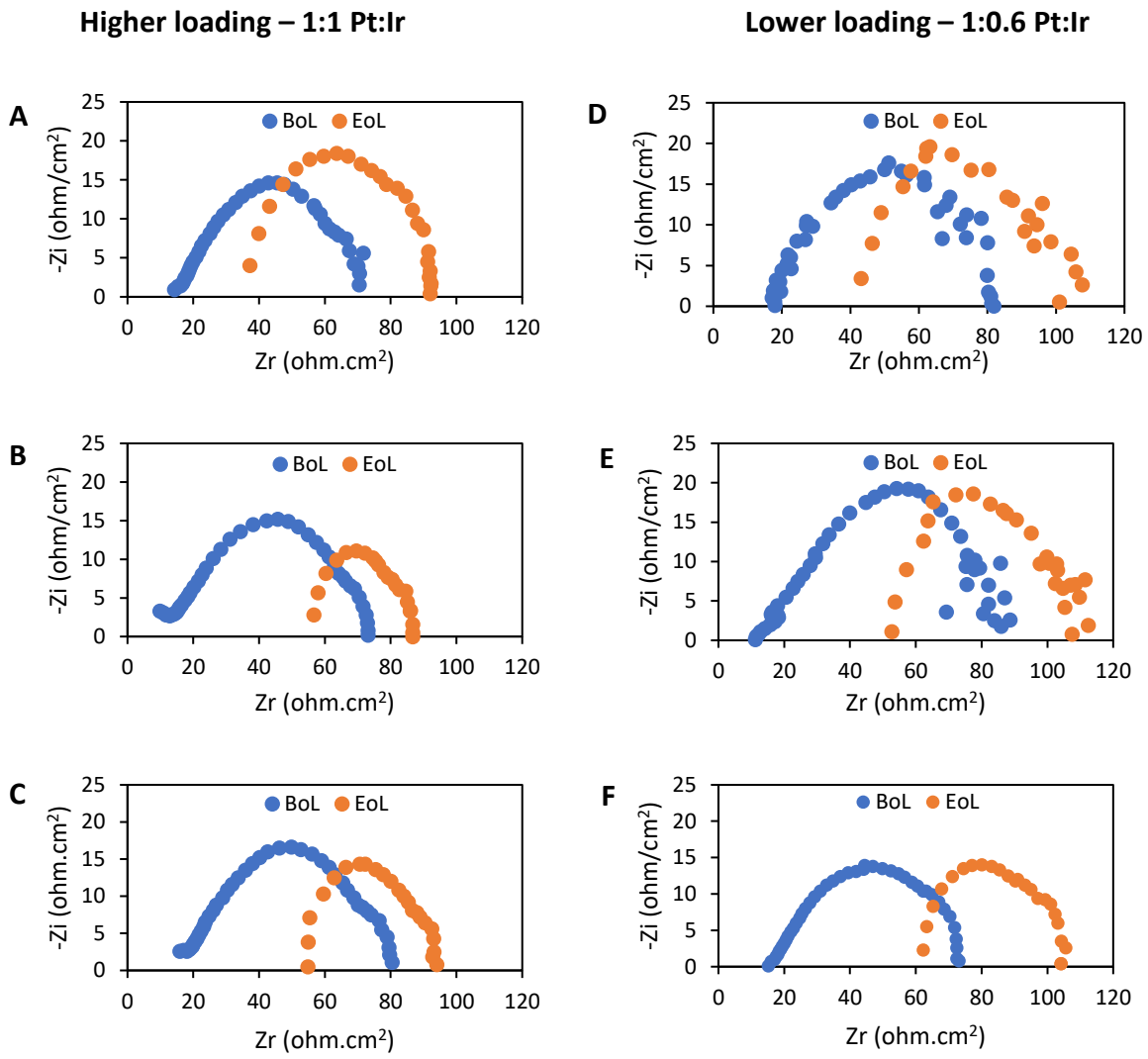

Figure 40 – EIS spectra of 5-, 10- and 30-min ASTs for higher loading MEAs displayed in A, B and C respectively. EIS spectra of 5-, 10- and 30-min ASTs for lower loading MEAs displayed in D, E and F respectively.

The following characterizations were performed on the higher loading MEAs as they exhibited better performance compared to the lower loading MEAs in both the long hold and repeated pulse testing.

6.1.4. Hydrogen crossover

Hydrogen crossover was performed to determine any possible degradation of the membrane during the ASTs resulting in the formation of pinholes. The potential caused by H_2 crossover is shown in Figure 41. The results showed that the increase in the current density was constant

as the potential was stepped up before testing and after all cell reversal tests. When the graph is extrapolated to 0 V, the y-intercept equals the amount of H_2 crossover that takes place in the MEA. The respective intercepts before and after testing were 8.3 and 8.2 mA/cm^2 which corresponds to approximately 0.063 and 0.062 sccm H_2/min·cm^2 respectively. This was obtained through the following sample calculation:

$$no.\ mole\ of\ electrons\ = \frac{Charge}{Faraday's\ constant} = \frac{A\ \times t}{F}$$

$$no.\ mole\ of\ electrons = \frac{8.2\ \times 60}{2\ \times 96485} = 2.55 \times 10^{-6}\ mol\ e^{-}$$

Using the ideal gas equation; $Volume\ of\ H_2 = \frac{nRT}{P}$

$$Volume\ of\ H_2 = \frac{2.55 \times 10^{-6}\ \times 8.314\ \times 298}{101325} = 6.24 \times 10^{-8}\ m^3\ H_2/min$$

$$\therefore\ = 0.0624\ sccm\ H_2/min \cdot cm^2$$

Where sccm = standard cubic centimetres

Since there was no significant change in the amount of H_2 crossover before and after testing, it was concluded that there were no pinholes formed in any of the membranes during the ASTs, and that the physcial integrety of the membrane remains intact.

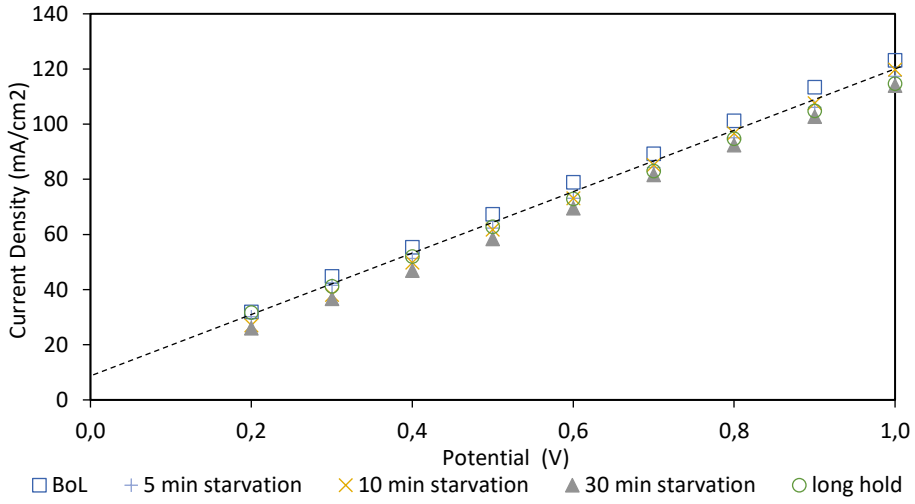

Figure 41 - Current response from potential step for hydrogen crossover measurements performed before and after the cell reversal tests on the modified MEA.

6.1.5. Cyclic voltammetry for ECSA

The CVs, which are typically taken on the cathode of the MEA, were performed to determine the change in ECSA as a result of potential reversal using the principles discussed in section 2.11.3. Generally, a CV taken on an MEA electrode made from Pt/C does not show the clear characteristic voltammogram as seen with polycrystalline Pt in an electrolyte solution, however, they nonetheless provide useful information in assessing the ECSA (Yasuda *et al.*, 2006).

The CVs were obtained after each AST and are shown in Figure 42. The voltammograms show that the shape of the CVs were similar with minor losses of Pt ECSA after fuel starvation AST. Table 16 contains the calculated ECSAs obtained from integrating the area under the hydrogen adsorption peaks.

A marginal decrease in the ECSA after testing was observed, similar to those in a study performed by Taniguchi *et al.*, (2008), which showed that ECSA decreased with potential reversal. However, ECSA reduction has also been observed under normal operation of a fuel cell (Darling and Meyers, 2003; Ferreira *et al.*, 2005; Mayur *et al.*, 2018). Therefore, this reduction might not be solely due to the fuel starvation ASTs but also passivation during operation as there was not a significant decrease in ECSA between the 30 min test and 15-hour long hold.

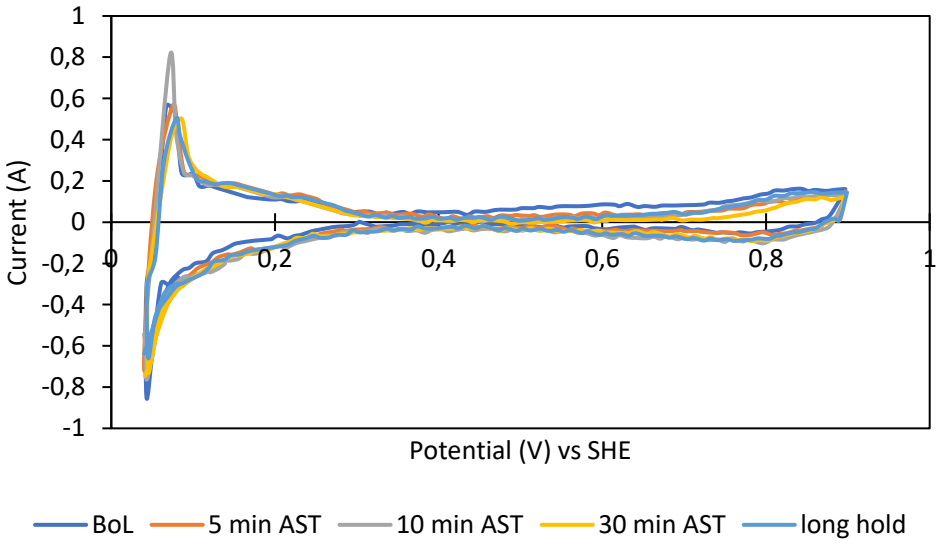

Figure 42 - Cyclic voltammograms determined on the cathode of the modified MEAs after ASTs to determine ECSA.

Table 16 - Calculated ECSAs for the IrO_x/GV modified MEAs after ASTs.

Test	ECSA (m^2/g Pt)
BoL	72.09
5 min AST	71.17
10 min AST	69.32
30 min AST	69.69
long hold	69.00

6.2. Physical Characterization of the Ir loaded MEAs

6.2.1. X-ray Photoelectric Spectroscopy (XPS)

XPS analysis was performed on the MEAs after they had been conditioned for 2 hours, after 30 min of fuel starvation and indefinite starvation. XPS was primarily performed on the active catalyst metals, Ir and Pt, to determine their stability under the highly oxidative conditions of potential reversal. This analysis would provide insight into the change in the oxidation states of the catalysts and suggest possible passivation, oxidation or even dissolution pathways.

1. Ir 4f components

The fitting parameters for the Ir species in the respective MEAs are shown in Table 17 and the ratio of the components are displayed in Figure 43. The XPS data fittings can be found in appendix E. After conditioning of the IrO_x/GV containing MEA, the majority of the Ir was in the Ir^{4+} state which remained unchanged after the 30 min fuel starvation AST. The prevalent Ir^{4+} state of the IrO_x/GV catalyst in the MEA presented a significant shift from the oxidation states present in the synthesized catalyst, which was Ir^{3+} dominated (Figure 22). This result was further found to be in agreement to the work done by Saveleva *et al.*, (2018), where potentials applied to an IrO_x catalyst decreased the contribution of Ir^{3+} species. However, over a long period of time of fuel starvation, the Ir 4f spectra shifted to higher binding energies which resulted in a larger contribution of Ir^{3+} in the MEA. Ir^{3+} is considered to be crucial for high activities (Kasian *et al.*, 2018; Spöri *et al.*, 2019) therefore, a higher ratio of Ir^{3+} would suggest the OER catalyst activity increases slightly.

Table 17 - Fitting parameters for the Ir 4f species on the anode layer of the MEA after conditioning and fuel starvation tests.

	after conditioning		after 30 min		after long hold	
	BE (eV)	FWHM (eV)	BE (eV)	FWHM (eV)	BE (eV)	FWHM (eV)
Ir metallic	60.7	1.2	60.7	1.2	60.7	1.2
Ir 4+	61.5	1.7	61.5	1.6	61.5	1.5
Ir 3+	62.5	1.7	62.35	1.7	62.4	1.5
Ir 4+ sat 1*	62.8	2.6	62.8	2.502	62.8	2.6
Ir 4+ sat 2	67.9	2	67.9	2	68.2	2
Ir 3+ sat	63.45	2.82	63.45	2.502	63.9	2.6

**sat 1 & 2 refer to the satellite peaks of Ir4+*

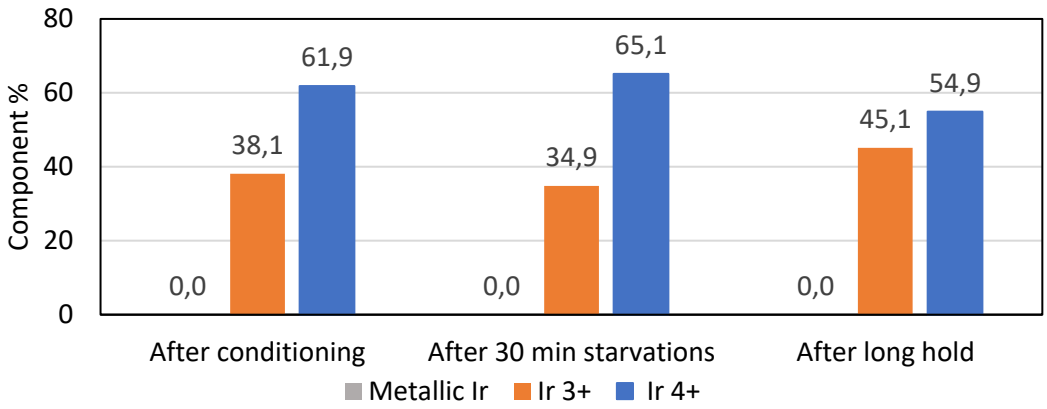

Figure 43 - Ratio of Ir species on the anode layer of MEAs after condition, 30 min and long hold ASTs.

1. Anode Pt 4f components

The XPS fitting parameters for Pt 4f are shown in Table 18 and the ratio of the respective species illustrated in Figure 44. The fitted graphs are in Appendix E. For all fittings, the ratio of Gaussian to Lorentzian contribution was taken to be 20. Before the AST, approximately 75% of the Pt was in its metallic form and after the multiple 30 min potential reversal tests, the ratio of the Pt species was unchanged. However, after the long 15 hr starvation event, the Pt was oxidized with slightly more than 50% remaining in the metallic form and the rest being in either the Pt^{2+} or Pt^{4+} states. The oxidized Pt species are not active when it comes to the HOR and ORR, therefore the passivation of the Pt catalyst during extended starvation events could be a factor which resulted in the MEA's performance reduction and reduced ECSA.

Table 18 - Fitting parameters for the Pt 4f species on the anode layer of the MEA after conditioning and fuel starvation tests.

	after conditioning		after 30 min		after long hold	
	BE (eV)	**FWHM (eV)**	**BE (eV)**	**FWHM (eV)**	**BE (eV)**	**FWHM (eV)**
Pt 0	71.05	1.5	71.05	1.5	71.15	1.5
Pt 2+ (-OH)	72	1.6	72	1.6	72.2	1.6
Pt 2+ (-O)	73.9	1.6	73.9	1.6	73.5	1.6
Pt 4+	75.4	1.6	75.3	1.6	74.9	1.6

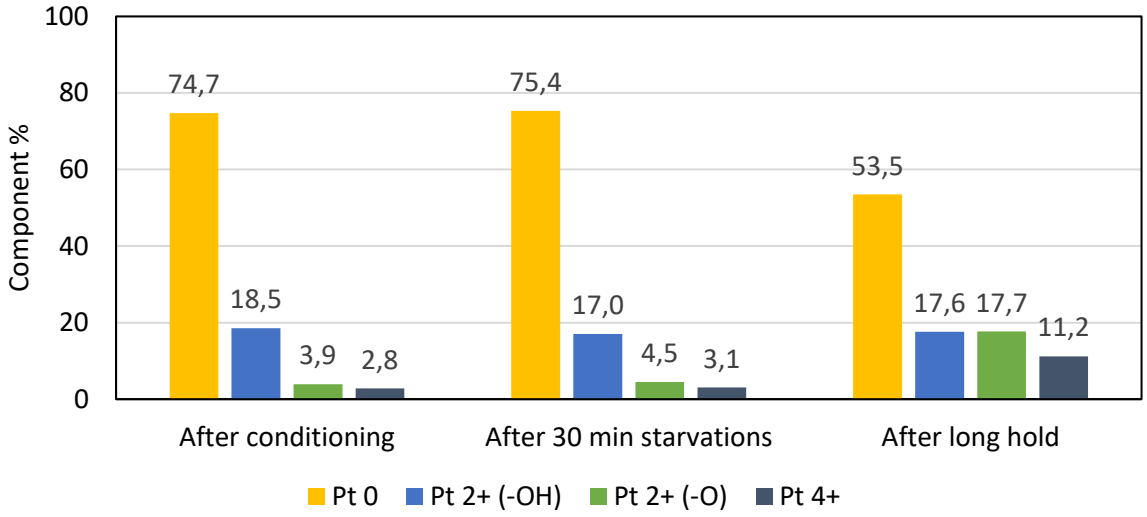

Figure 44 - Ratio of Pt species on the anode layer of MEAs after condition, 30 min and long hold ASTs.

2. Cathode Pt 4f components

According to Figure 45, the Pt on the cathode layer was more oxidized (higher fraction in the Pt^{2+} and Pt^{4+} states) compared to the anode layer after conditioning. This is likely due to the higher availability of oxygen on the cathode side of the MEA. However, the Pt on the cathode was more stable and there were no major changes in oxidation states after the two AST conditions tested. The obtained XPS confirmed that the changed ECSA determined in section 6.1.4 were minor with repeated potential reversal ASTs. The fitted spectra for each MEA can be found in Appendix E.

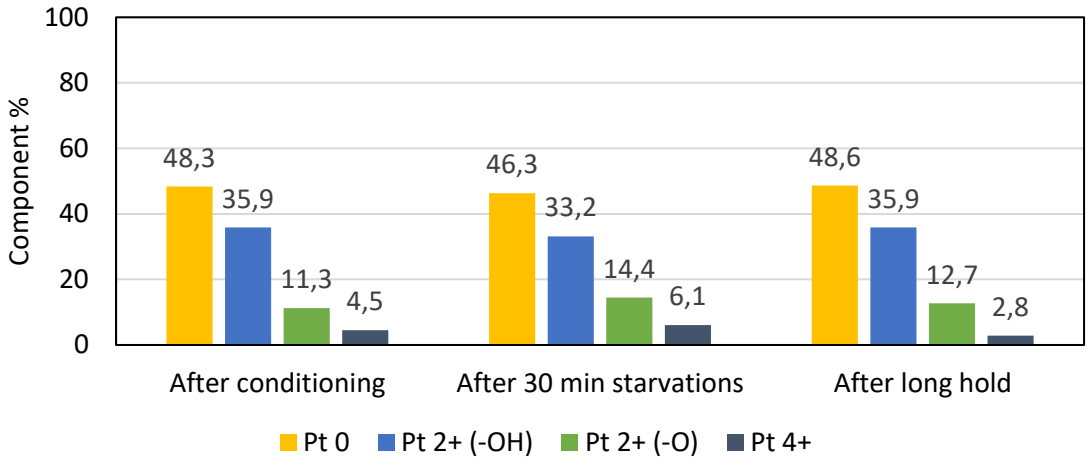

Figure 45 - Ratio of Pt species on the cathode layer of MEAs after conditioning, 30 min and long hold ASTs.

6.2.2. Scanning Electron Microscopy (SEM)

The SEM images were taken on the MEAs after the initial conditioning and then after each starvation event. In Figure 46, the cathode is observed to have a constant thickness (~15 µm) throughout each AST indicating insignificant degradation on the cathode side. Minimal cathode degradation is expected due to the relatively stable ECSAs presented in section 6.1.4 and XPS data in section 6.2.1. The anode and membrane, however, became thinner when subjected to the potential reversal tests for longer periods of time. After ASTs the anode and membrane had a maximum reduction in thickness of approximately 80% and 30% respectively as can be seen in Figure 47.

A study by Travassos and Rangel, (2010) found that thicker catalyst and membrane layers resulted in higher electronic and ohmic resistances compared to thinner layers. But when layer thinning occurs, the catalyst dissolves and reaction pathways are disrupted resulting in higher resistances. This is, however, not seen in the EIS results for the 5-, 10- and 30-min starvation events (Section 6.1.2) as the ORR dominated the charge transfer resistance observed in the MEA. The thinning of the membrane, is most likely due to its dehydration as the OER consumes water, reducing its ability to conduct protons thereby increasing its ohmic resistance.

Therefore, the performance loss of the Ir-loaded MEAs after AST as well as the increase in ohmic resistance observed in EIS, is most likely due to irreversible damage caused by membrane dehydration.

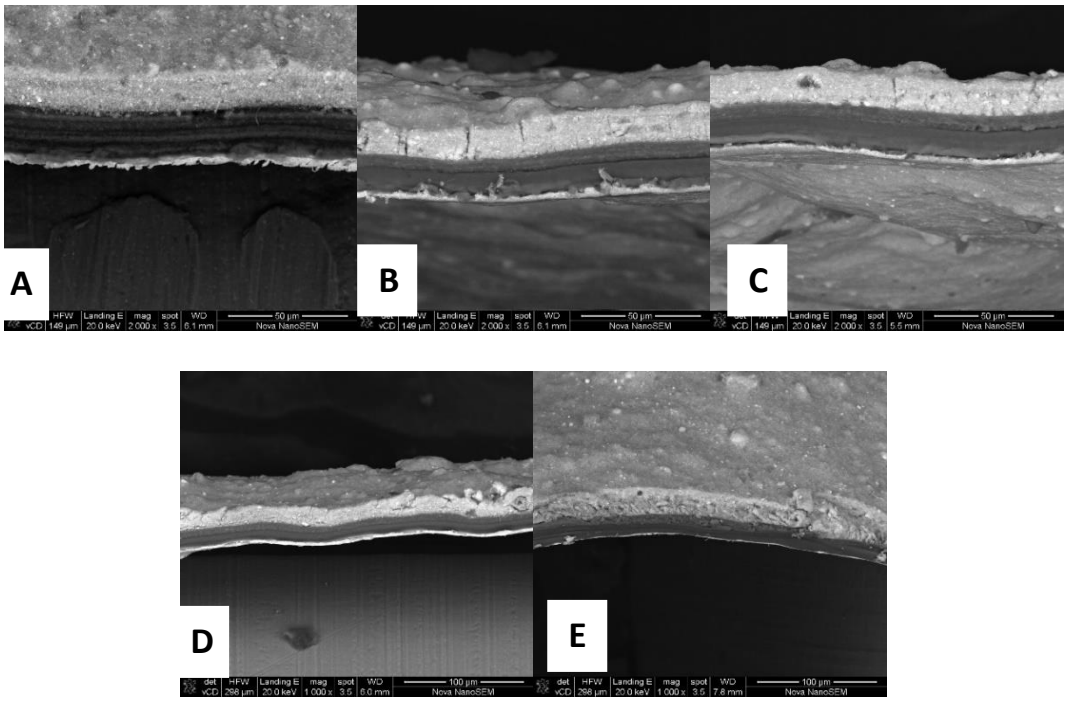

Figure 46 - Cross-sectional images of MEAs after (A) conditioning (B) 5 min AST (C) 10 min AST (D) 30 min AST (E) long hold.

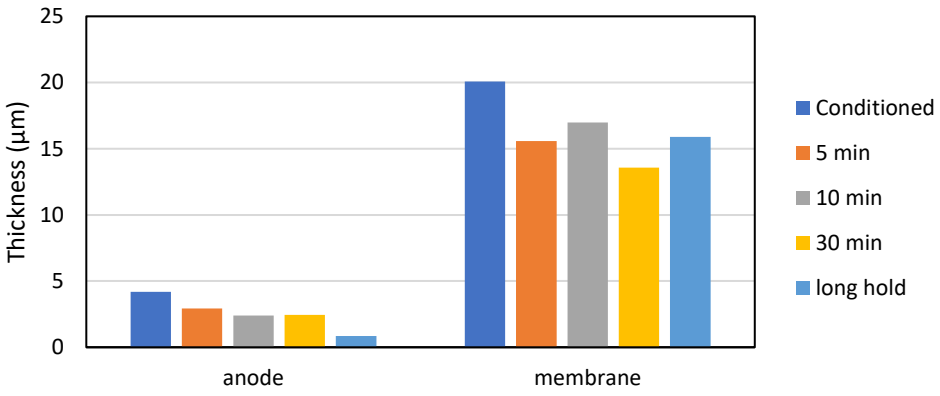

Figure 47 - Thickness of the anode and membrane layers of MEAs before and after potential reversal tests.

7. Conclusion and Recommendations

The aim of this work was to increase the durability of an MEA in the harsh degradative environment during potential reversal caused by fuel starvation by including a GV supported IrO_x catalyst.

The IrO_x/GV catalyst was successfully synthesized using a microwave assisted polyol deposition technique. This produced well dispersed IrO_x nanoparticles with majority of the particles in the size range of 4-8 nm. XRD and XPS analysis confirmed that the catalyst contained no metallic Ir but a combination of Ir^{4+} and Ir^{3+} in the form of lattice O and surface oxide species respectively. The catalyst had a higher loading than originally started with which was due to the partial oxidation of the GV support during calcination. This degradation was confirmed with TGA and was found that the presence of Ir accelerated the oxidation of the support.

An electrochemical benchmarking study was then performed to determine the activity and durability of the OER catalyst with respect to two commercially available catalyst (Ir/Vulcan from FuelCell store® and IrO_x/TiO_2 from Umicore®). The synthesized catalyst had a mass activity of 0.138 A/mg Ir and lost 51% of its activity after 5000 potential cycles. These results showed that the synthesized catalyst had a balance between its mass activity and durability compared to the two commercially available catalysts.

The synthesized catalyst was then included in the anode of an MEAs made with commercial Pt/C at 0.1 mg Ir/cm^2 and 0.06 mg Ir/cm^2. The produced MEAs were reversal tolerant and successfully exhibited the ability to maintain the cell potential in the water electrolysis region and greatly reduce the effects of carbon oxidation. These were evaluated using a long hold test as well as successive pulse starvation tests. Although severe carbon corrosion was avoided, a slow rate of carbon degradation is still observed when the MEA was subjected to fuel starvation. This was confirmed through the decrease in polarization curves after each successive starvation event. The loss in performance was found to be a combination of multiple factors, the first being the thinning of the anode layer and membrane of which the latter led to an increase in ohmic resistance in the cell. The Pt in the anode layer was also found to be susceptible to oxidation and therefore deactivation, when the MEA was subjected to prolonged periods of fuel starvation. The cathode catalyst was stable and unaffected by

the fuel starvation as there was no change in the Pt oxidation states and negligible carbon corrosion.

In summary, this work proved that the addition IrO_x/GV can greatly improve the durability of an MEA for multiple potential reversal events and still maintain reasonable performance. To further improve on these results, it is recommended that a carbon support with higher degrees of graphitization be investigated, or other synthesis methods be considered which do not result in the loss of carbon support in the process. This could help in producing smaller IrO_x nanoparticles which can provide higher mass activities and therefore higher OER performance for a smaller amount of catalyst. Secondly, other factors which contribute to the MEAs degradation such as ionomer and membrane degradation should also be investigated in more detail to provide a better understanding of all mechanisms occurring during potential reversal.

8. References

Abaspour, A., Tadrisi Parsa, N. and Sadeghi, M. (2014) 'A New Feedback Linearization-NSGA-II based Control Design for PEM Fuel Cell', *International Journal of Computer Applications*, 97(10), pp. 25–32. doi: 10.5120/17044-7354.

Abbott, D. F. *et al.* (2016) 'Iridium oxide for the oxygen evolution reaction: Correlation between particle size, morphology, and the surface hydroxo layer from operando XAS', *Chemistry of Materials*, 28(18), pp. 6591–6604. doi: 10.1021/acs.chemmater.6b02625.

Alia, S. M. *et al.* (2016) 'Activity and Durability of Iridium Nanoparticles in the Oxygen Evolution Reaction', *Journal of The Electrochemical Society*, 163(11), pp. F3105–F3112. doi: 10.1149/2.0151611jes.

Allagui, A. *et al.* (2013) 'Ammonia electro-oxidation on alloyed PtIr nanoparticles of well-defined size', *International Journal of Hydrogen Energy*. Elsevier Ltd, 38(5), pp. 2455–2463. doi: 10.1016/j.ijhydene.2012.11.079.

Antolini, E. and Gonzalez, E. R. (2009) 'Ceramic materials as supports for low-temperature fuel cell catalysts', *Solid State Ionics*. Elsevier B.V., 180(9–10), pp. 746–763. doi: 10.1016/j.ssi.2009.03.007.

Anumol, E. A. *et al.* (2011) 'New insights into selective heterogeneous nucleation of metal nanoparticles on oxides by microwave-assisted reduction: rapid synthesis of high-activity supported catalysts', *ACS Nano*, 5(10), pp. 8049–8061. doi: 10.1021/nn202639f.

Appleby, A. J. (1990) 'From Sir William Grove to today: Fuel cells and the future', *Journal of Power Sources*, 29(1–2), pp. 3–280. doi: 10.1016/0378-7753(90)80002-U.

Asghari, S., Mokmeli, A. and Samavati, M. (2010) 'Study of PEM fuel cell performance by electrochemical impedance spectroscopy', *International Journal of Hydrogen Energy*. Elsevier Ltd, 35(17), pp. 9283–9290. doi: 10.1016/j.ijhydene.2010.03.069.

Baumgartner, W. R. *et al.* (2008) 'Polarization study of a PEMFC with four reference electrodes at hydrogen starvation conditions', *Journal of Power Sources*, 182(2), pp. 413–421. doi: 10.1016/j.jpowsour.2008.01.001.

Bellis, M. (2019) *Hydrogen Fuel Cells Innovation for the 21st Century*. Available at: https://www.thoughtco.com/hydrogen-fuel-cells-1991799.

Biesheuvel, P. M. and Dykstra, J. E. (2018) 'The difference between Faradaic and Nonfaradaic processes in Electrochemistry', pp. 1–10. Available at: http://arxiv.org/abs/1809.02930.

Castanheira, L. *et al.* (2015) 'Carbon Corrosion in Proton-Exchange Membrane Fuel Cells: Effect of the Carbon Structure, the Degradation Protocol, and the Gas Atmosphere', *ACS Catalysis*, 5(4), pp. 2184–2194.

Cherevko, S. *et al.* (2015) 'Oxygen and hydrogen evolution reactions on Ru, RuO2, Ir, and IrO2 thin film electrodes in acidic and alkaline electrolytes: A comparative study on activity and stability', *Catalysis Today*. Elsevier B.V., 262, pp. 170–180. doi: 10.1016/j.cattod.2015.08.014.

Cherevko, S. (2018) 'Stability and dissolution of electrocatalysts : Building the bridge between model and " real world " systems', *Current Opinion in Electrochemistry*. Elsevier B.V., pp. 1–8. doi: 10.1016/j.coelec.2018.03.034.

Choi, S. J. *et al.* (2014) 'Bi-functional co-sensitization of graphene oxide sheets and Ir nanoparticles on p-type Co3O4 nanofibers for selective acetone detection', *Journal of Materials Chemistry B*. Royal Society of Chemistry, 2(41), pp. 7160–7167. doi: 10.1039/c4tb00767k.

Climent, V. and Feliu, J. M. (2011) 'Thirty years of platinum single crystal electrochemistry', *Journal of Solid State Electrochemistry*, 15(7–8), pp. 1297–1315. doi: 10.1007/s10008-011-1372-1.

Darling, R. M. and Meyers, J. P. (2003) 'Kinetic model of platinum dissolution in PEMFCs', *Journal of the Electrochemical Society*, 150(11), pp. 1523–1527. doi: 10.1149/1.1613669.

Ferreira, P. J. *et al.* (2005) 'Instability of Pt / C Electrocatalysts in Proton Exchange Membrane Fuel Cells A Mechanistic Investigation', *Journal of The Electrochemical Society*, 152(11), pp. A2256–A2271. doi: 10.1149/1.2050347.

Fievet, F. *et al.* (2018) 'The polyol process: a unique method for easy access to metal nanoparticles with tailored sizes, shapes and compositions', *Chemical Society Reviews*. Royal Society of Chemistry, 47(14), pp. 5187–5233. doi: 10.1039/c7cs00777a.

Gharehpetian, G. B. and Mousavi Agah, S. M. (2017) *Distributed generation systems: Design, operation and grid integration*, *Distributed Generation Systems: Design, Operation and Grid Integration*.

Guo, S. and Sun, S. (2012) 'FePt Nanoparticles Assembled on Graphene as Enhanced Catalyst for Oxygen Reduction Reaction', *Journal of the American Chemical Society*, 134(5), pp. 2492–2495.

Herrmann, F. and Rothfuss, F. (2015) *Introduction to hybrid electric vehicles, battery electric vehicles, and off-road electric vehicles*, *Advances in Battery Technologies for Electric Vehicles*. Elsevier Ltd. doi: 10.1016/b978-1-78242-377-5.00001-7.

Höchst, H., Steiner, P. and Hüfner, S. (1980) 'II. XPS study of 3 d-metal ions dissolved in noble metals', *Zeitschrift für Physik B Condensed Matter*, 38(3), pp. 201–209. doi: 10.1007/BF01315658.

Hodkiewicz, J. (2010) *Characterizing Carbon Materials with Raman Sepctroscopy*.

Hong, B. K. *et al.* (2016) 'On the impact of water activity on reversal tolerant fuel cell anode performance and durability', *Journal of Power Sources*. Elsevier B.V, 328, pp. 280–288. doi: 10.1016/j.jpowsour.2016.07.002.

Hu, J. *et al.* (2009) 'Modelling and simulations of carbon corrosion during operation of a Polymer Electrolyte Membrane fuel cell', *Electrochimica Acta*, 54(23), pp. 5583–5592. doi: 10.1016/j.electacta.2009.04.073.

Ishigami, Y. *et al.* (2011) 'Corrosion of carbon supports at cathode during hydrogen/air replacement at anode studied by visualization of oxygen partial pressures in a PEFC - Start-up/shut-down simulation', *Journal of Power Sources*. Elsevier B.V., 196(6), pp. 3003–3008.

doi: 10.1016/j.jpowsour.2010.11.092.

Jang, I., Hwang, I. and Tak, Y. (2013) 'Attenuated degradation of a PEMFC cathode during fuel starvation by using carbon-supported IrO2', *Electrochimica Acta*. Elsevier Ltd, 90, pp. 148–156.

Jia, F. *et al.* (2016) 'Mechanisms of reverse current and mitigation strategies in proton exchange membrane fuel cells during startups', *International Journal of Hydrogen Energy*. Elsevier Ltd, 41(15), pp. 6469–6475. doi: 10.1016/j.ijhydene.2016.03.037.

Jourdani, M., Mounir, H. and El Marjani, A. (2014) 'Compilation of factors affecting durability of proton exchange membrane fuel cell (PEMFC)', *Proceedings of 2014 International Renewable and Sustainable Energy Conference, IRSEC 2014*. IEEE, pp. 542–547. doi: 10.1109/IRSEC.2014.7059906.

Kang, J. *et al.* (2010) 'Accelerated test analysis of reversal potential caused by fuel starvation during PEMFCs operation', *International Journal of Hydrogen Energy*. Elsevier Ltd, 35(8), pp. 3727–3735. doi: 10.1016/j.ijhydene.2010.01.071.

Kasian, O. *et al.* (2018) 'The Common Intermediates of Oxygen Evolution and Dissolution Reactions during Water Electrolysis on Iridium', *Angewandte Chemie International Edition*, 57, pp. 2488–2491. doi: 10.1002/anie.201709652.

Kim, D. *et al.* (2015) 'Fabrication of iridium oxide nanoparticles supported on activated carbon powder by flashlight irradiation for oxygen evolutions', *Materials Science & Engineering B*. Elsevier B.V., 201, pp. 29–34. doi: 10.1016/j.mseb.2015.06.004.

Kim, J. *et al.* (2008) 'Direct Relationship between Carbon Corrosion and Cathode Potential during Fuel Starvation in PEMFC', *ECS Transactions*, 16(2), pp. 961–968. doi: 10.1149/1.2981936.

Kim, J. H. *et al.* (2009) 'Development of a durable PEMFC startup process by applying a dummy load: I. Electrochemical study', *Journal of the Electrochemical Society*, 156(8), pp. 955–961. doi: 10.1149/1.3148222.

Knights, S. D. *et al.* (2003) 'Fuel cell anode structures for voltage reversal tolerance'. United States of America.

Kunusch, C., Puleston, P. and Mayosky, M. (2012) 'PEM Fuel cell systems', in *Advances in Industrial Control*, pp. 13–31. doi: 10.1007/978-1-4471-2431-3.

Liang, D. *et al.* (2009) 'Study of the cell reversal process of large area proton exchange membrane fuel cells under fuel starvation', *Journal of Power Sources*, 194(2), pp. 847–853. doi: 10.1016/j.jpowsour.2009.06.059.

Longo, S. *et al.* (2017) *Life Cycle Assessment of Solid Oxide Fuel Cells and Polymer Electrolyte Membrane Fuel Cells: A Review*, *Hydrogen Economy: Supply Chain, Life Cycle Analysis and Energy Transition for Sustainability*. Elsevier Ltd. doi: 10.1016/B978-0-12-811132-1.00006-7.

Mayur, M. *et al.* (2018) 'Lifetime prediction of a polymer electrolyte membrane fuel cell under automotive load cycling using a physically-based catalyst degradation model', *Energies*, 11(8), pp. 1–21. doi: 10.3390/en11082054.

Mccrory, C. C. L. *et al.* (2013) 'Benchmarking Heterogeneous Electrocatalysts for the Oxygen Evolution Reaction', *Journal of the American Chemical Society*, 135, pp. 16977–16987. Available at: https://pubs-acs-org.proxy.lib.umich.edu/doi/suppl/10.1021/ja407115p/suppl_file/ja407115p_si_001.pdf.

Oh, H. S. *et al.* (2016) 'Electrochemical Catalyst-Support Effects and Their Stabilizing Role for IrOx Nanoparticle Catalysts during the Oxygen Evolution Reaction', *Journal of the American Chemical Society*, 138(38), pp. 12552–12563. doi: 10.1021/jacs.6b07199.

Owejan, J. E., Yu, P. T. and Makharia, R. (2007) 'Mitigation of Carbon Corrosion in Microporous Layers in PEM Fuel Cells J.E.Owejan', *ECS Transactions*, 11(1), pp. 1049–1057.

Park, S., Lee, J. W. and Popov, B. N. (2012) 'A review of gas diffusion layer in PEM fuel cells: Materials and designs', *International Journal of Hydrogen Energy*. Elsevier Ltd, 37(7), pp. 5850–5865. doi: 10.1016/j.ijhydene.2011.12.148.

Park, Y. *et al.* (2015) 'Effects of short-side-chain per fl uorosulfonic acid ionomers as binders on the performance of low Pt loading fuel cell cathodes', *Journal of Power Sources*. Elsevier B.V, 275, pp. 384–391. doi: 10.1016/j.jpowsour.2014.10.149.

Patterson, T. W. and Darling, R. M. (2006) 'Damage to the Cathode Catalyst of a PEM Fuel Cell Caused by Localized Fuel Starvation', *Electrochemical and Solid-State Letters*, 9(4), pp. A183–A185. doi: 10.1149/1.2167930.

Perry, M. L., Patterson, T. and Reiser, C. (2006) 'Systems Strategies to Mitigate Carbon Corrosion in Fuel Cells', *ECS Transactions*, 3(September), pp. 783–795. doi: 10.1149/1.2356198.

Pfeifer, V. *et al.* (2016) 'The electronic structure of iridium and its oxides', *Surface and Interface Analysis*, 48(5), pp. 261–273. doi: 10.1002/sia.5895.

Qin, C. *et al.* (2016) 'Proton Exchange Membrane Fuel Cell Reversal: A Review', *Catalysts*, 6(12), p. 197. doi: 10.3390/catal6120197.

Ralph, T. R., Hudson, S. and Wilkinson, D. P. (2006) 'Electrocatalyst stability in PEMFCs and the role of fuel starvation and cell reversal tolerant anodes', *ECS Transactions*, 1(8), pp. 67–84.

Reiser, C. A. *et al.* (2005) 'A Reverse-Current Decay Mechanism for Fuel Cells', *Electrochemical and Solid-State Letters*, 8(6), p. A273. doi: 10.1149/1.1896466.

Sadhasivam, T. *et al.* (2016) 'Graphitized carbon as an efficient mesoporous layer for unitized regenerative fuel cells', *International Journal of Hydrogen Energy*. Elsevier Ltd, 41(40), pp. 18226–18230. doi: 10.1016/j.ijhydene.2016.08.092.

Sakai, N. *et al.* (2004) 'Electronic Band Structure of Titania Semiconductor Nanosheets Revealed by Electrochemical and Photoelectrochemical Studies', *Journal of the American Chemical Society*, 126(18), pp. 5851–5858. doi: 10.1021/ja0394582.

Saveleva, V. A. *et al.* (2018) 'Operando Evidence for a Universal Oxygen Evolution Mechanism on Thermal and Electrochemical Iridium Oxides', *Journal of Physical Chemistry Letters*, 9(11), pp. 3154–3160. doi: 10.1021/acs.jpclett.8b00810.

Scribner Associates (2014) *Electrochemical Impedance Spectroscopy (EIS): A Powerful and Cost- Effective Tool for Fuel Cell Diagnostics*. doi: 10.1016/0013-4686(90)80007-B.

Sedighizadeh, M. and Rezazadeh, A. (2007) 'Comparison between Batteries and Fuel Cells for Photovoltaic System Backup', *International Journal of Energy and Power Engineering*, 1(12), pp. 1832–1836. doi: 10.5281/zenodo.1061743.

Shukla, A. K., Sampath, S. and Vijayamohanan, K. (2000) 'Electrochemical supercapacitors: Energy storage beyond batteries', *Current Science*, 79(12), pp. 1656–1661.

Silva, G. C., Perini, N. and Ticianelli, E. A. (2017) 'Effect of temperature on the activities and stabilities of hydrothermally prepared IrO x nanocatalyst layers for the oxygen evolution reaction', *Applied Catalysis B, Environmental*. Elsevier B.V., 218, pp. 287–297. doi: 10.1016/j.apcatb.2017.06.044.

Siracusano, S. *et al.* (2014) 'Performance analysis of short-side-chain Aquivion perfluorosulfonic acid polymer for proton exchange membrane water electrolysis', *Journal of Membrane Science*. Elsevier, 466, pp. 1–7. doi: 10.1016/j.memsci.2014.04.030.

Spiegel, C. *et al.* (2007) *Designing and Building Fuel Cells Library of Congress Cataloging-in-Publication Data*.

Spöri, C. *et al.* (2019) 'Experimental Activity Descriptors for Iridium-Based Catalysts for the Electrochemical Oxygen Evolution Reaction (OER)', *ACS Catalysis*, pp. 6653–6663. doi: 10.1021/acscatal.9b00648.

Tai, F. C. *et al.* (2006) 'Correlation between ID/IG ratio from visible Raman spectra and sp2/sp3 ratio from XPS spectra of annealed hydrogenated DLC film', *Materials Transactions*, 47(7), pp. 1847–1852. doi: 10.2320/matertrans.47.1847.

Taniguchi, A. *et al.* (2004) 'Analysis of electrocatalyst degradation in PEMFC caused by cell reversal during fuel starvation', *Journal of Power Sources*, 130(1–2), pp. 42–49. doi: 10.1016/j.jpowsour.2003.12.035.

Taniguchi, A. *et al.* (2008) 'Analysis of degradation in PEMFC caused by cell reversal during air starvation', *International Journal of Hydrogen Energy*, 33(9), pp. 2323–2329. doi: 10.1016/j.ijhydene.2008.02.049.

Travassos, M. A. and Rangel, C. M. (2010) 'Polarity Reversal in PEM Fuel Cells by Fuel Starvation', pp. 48–52.

Tüber, K., Pócza, D. and Hebling, C. (2003) 'Visualization of water buildup in the cathode of a transparent PEM fuel cell', *Journal of Power Sources*, 124(2), pp. 403–414. doi: 10.1016/S0378-7753(03)00797-3.

USA Department of Energy (no date) *Types of fuel cells*. Available at: https://www.energy.gov/eere/fuelcells/types-fuel-cells (Accessed: 18 July 2019).

Vaghari, H. *et al.* (2013) 'Recent advances in application of chitosan in fuel cells', *Sustainable Chemical Processes*, 1(1), p. 16. doi: 10.1186/2043-7129-1-16.

Wang, X. D. *et al.* (2008) 'Effect of humidity of reactants on the cell performance of PEM fuel cells with parallel and interdigitated flow field designs', *Journal of Power Sources*, 176(1), pp.

247–258. doi: 10.1016/j.jpowsour.2007.10.065.

Wee, J. H. (2007) 'Applications of proton exchange membrane fuel cell systems', *Renewable and Sustainable Energy Reviews*, 11(8), pp. 1720–1738. doi: 10.1016/j.rser.2006.01.005.

Wilkinson, D. P. and St-Pierre, J. (2003) 'Durability', in *Handbook of Juel Cells - Fundamentals, Technology and Applications*, pp. 611–626.

Yasuda, K. *et al.* (2006) 'Platinum dissolution and deposition in the polymer electrolyte membrane of a PEM fuel cell as studied by potential cycling', *Physical Chemistry Chemical Physics*, 8(6), pp. 746–752. doi: 10.1039/b514342j.

Yu, P. T. *et al.* (2006) 'The Impact of Carbon Stability on PEM Fuel Cell startup and shutdown voltage degradation', *ECS Transactions*, 3(1), pp. 797–809.

Yu, Y. *et al.* (2012) 'A review on performance degradation of proton exchange membrane fuel cells during startup and shutdown processes: Causes, consequences, and mitigation strategies', *Journal of Power Sources*, 205, pp. 10–23. doi: 10.1016/j.jpowsour.2012.01.059.

Zhang, S. *et al.* (2000) 'A phenomenological approach for the Id/Ig ratio and sp3 fraction of magnetron sputtered a-C films', *Surface and Coatings Technology*, 123(2–3), pp. 256–260. doi: 10.1016/S0257-8972(99)00523-X.

Zhang, S. *et al.* (2009) 'A review of accelerated stress tests of MEA durability in PEM fuel cells', *International Journal of Hydrogen Energy*, 34(1), pp. 388–404. doi: 10.1016/j.ijhydene.2008.10.012.

Zhu, W. H., Payne, R. U. and Tatarchuk, B. J. (2007) 'PEM stack test and analysis in a power system at operational load via ac impedance', *Journal of Power Sources*, 168(1 SPEC. ISS.), pp. 211–217. doi: 10.1016/j.jpowsour.2007.02.071.

Appendices

8.1. Appendix A: Particle size distribution data

Table A1 - PSD data for Ir/GV catalyst before calcination.

Class	Frequency	%
<0.5	10	4.0%
0.5 - 1.0	96	38.4%
1.0 - 1.5	104	41.6%
1.5 - 2.0	30	12.0%
2.0 - 2.5	9	3.6%
>2.5	1	0.4%

Table A2 - PSD data for IrOx/GV catalyst.

Class	Frequency	%
<1	0	0.0%
1-2	1	0.4%
2-3	7	2.8%
3-4	22	8.7%
4-5	43	17.1%
5-6	60	23.8%
6-7	62	24.6%
7-8	30	11.9%
8-9	15	6.0%
9-10	6	2.4%
10-11	4	1.6%
>10	2	0.8%

8.2. Appendix B: XPS wide scans

Figure B1 - Graphitized Vulcan support wide scan.

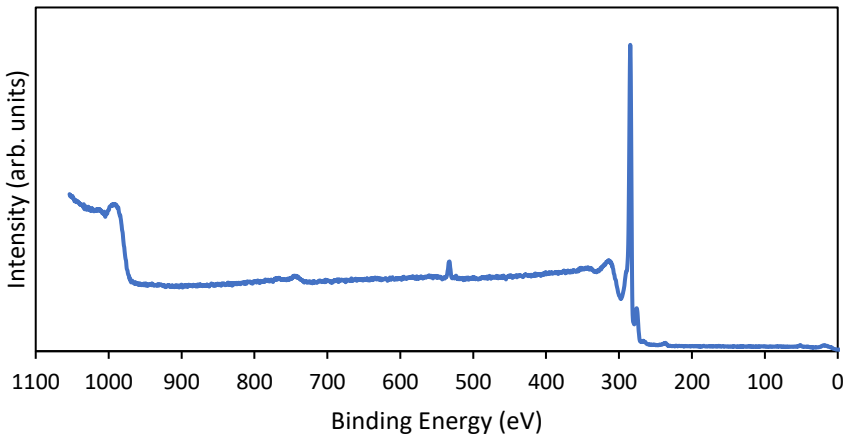

Figure B2 – Synthesized Ir/GV catalyst wide scan before calcination.

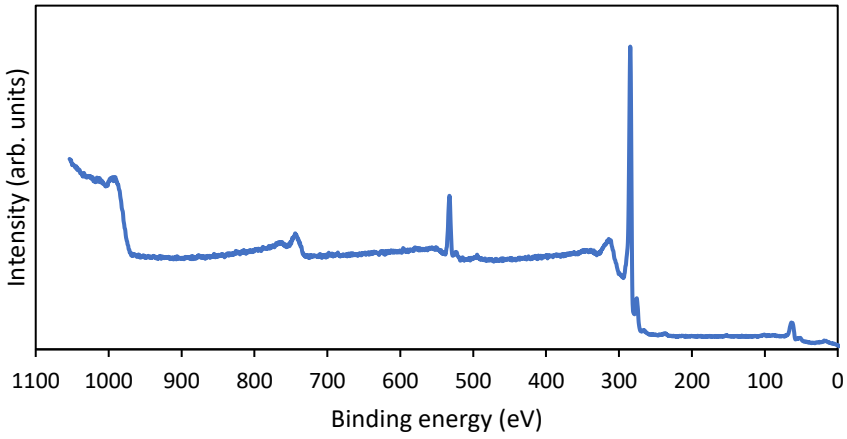

Figure B3 - IrO_x/GV synthesized catalyst wide scan.

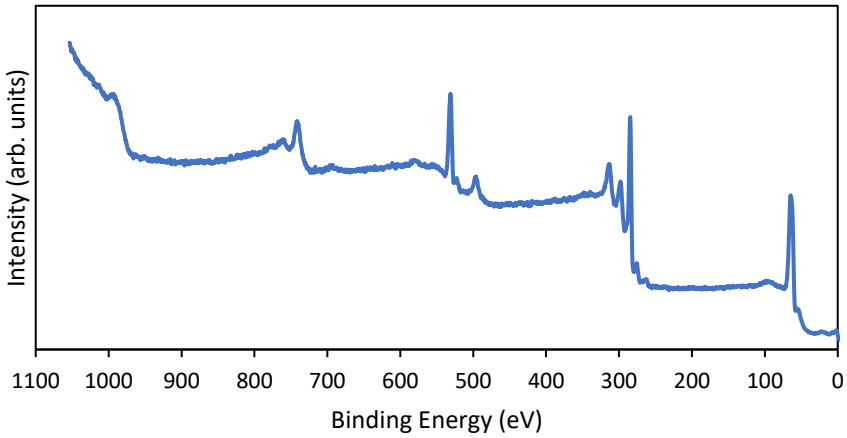

Figure B4 - Anode side of MEA after conditioning.

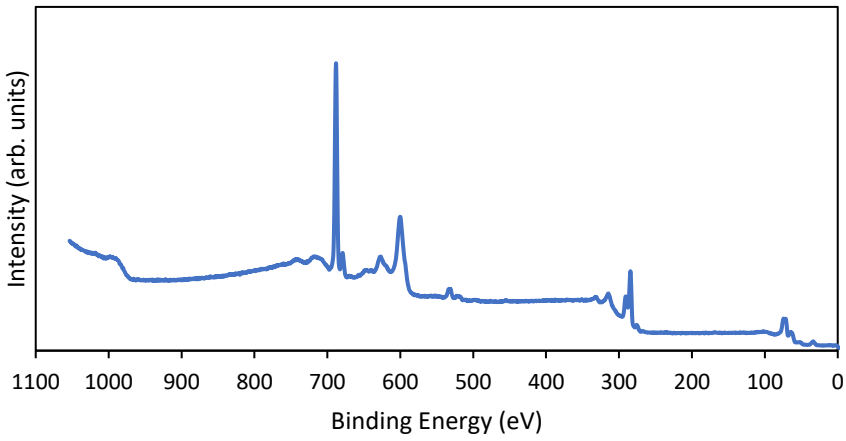

Figure B5 - Anode side of MEA after 30 min fuel starvation AST.

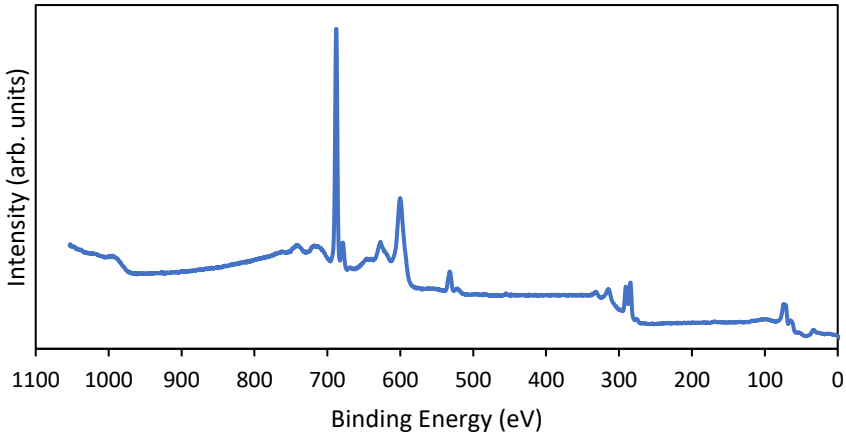

Figure B6 - Anode side of MEA after long hold AST.

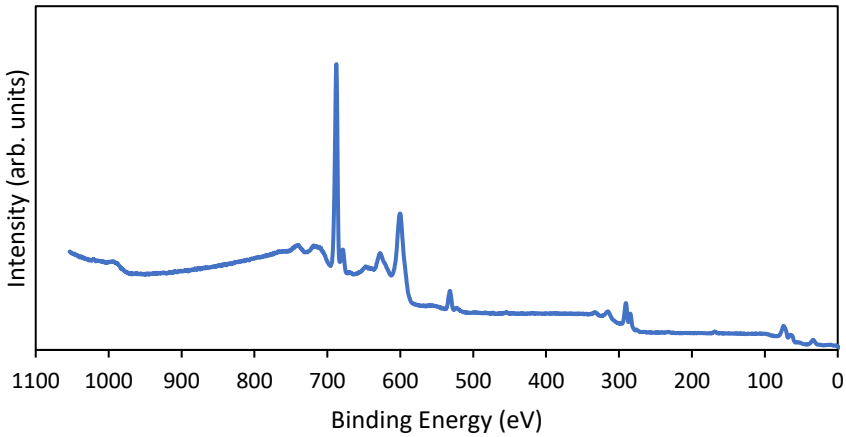

Figure B7 - Cathode side of MEA after conditioning.

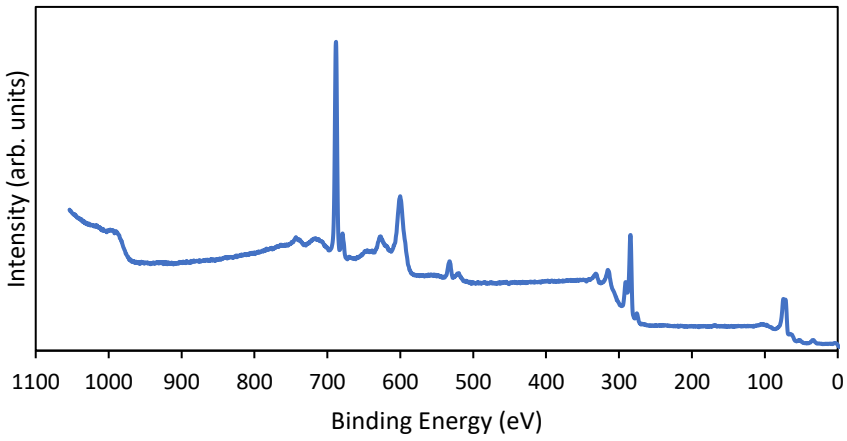

Figure B8 - Cathode side of MEA after 30 min fuel starvation AST.

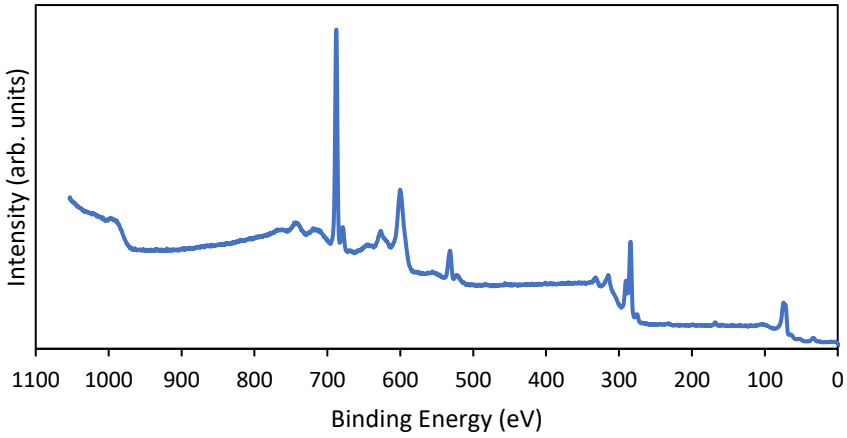

Figure B9 - Cathode side of MEA after long hold AST.

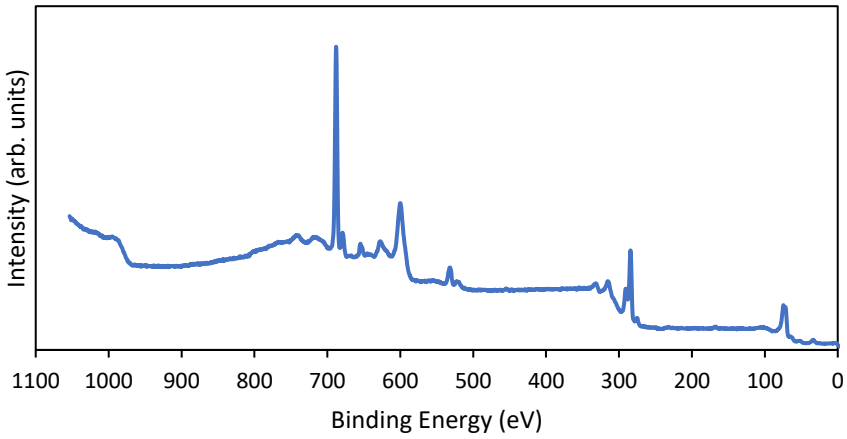

8.3. Appendix C: Comparison of performance polarization curves at varying relative humidities

Figure C1 - Polarization curves at varying operating conditions for performance analysis of 1:1 Pt:Ir ratio MEAs.

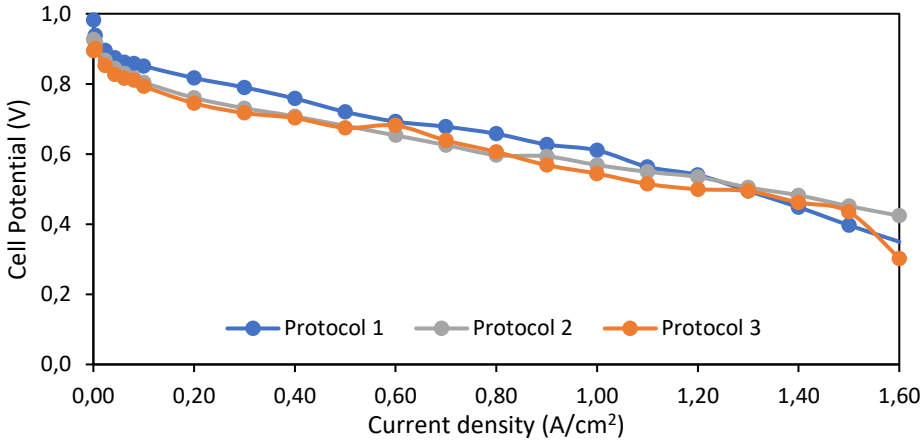

Figure C2 - Polarization curves at varying operating conditions for performance analysis of 1:0.6 Pt:Ir ratio MEAs.

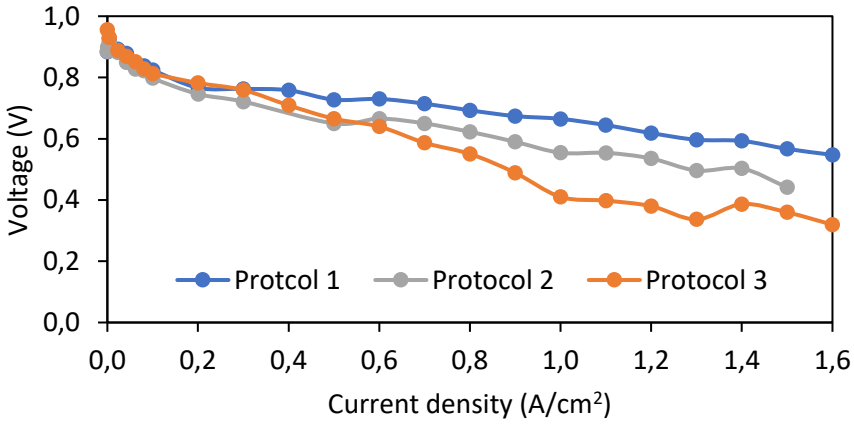

8.4. Appendix D: RTA AST potential response curves and polarization curves

Figure D1 - Voltage response for high loading MEA (1:1 Ir:Pt) in 5 min starvation and 10 min recovery AST

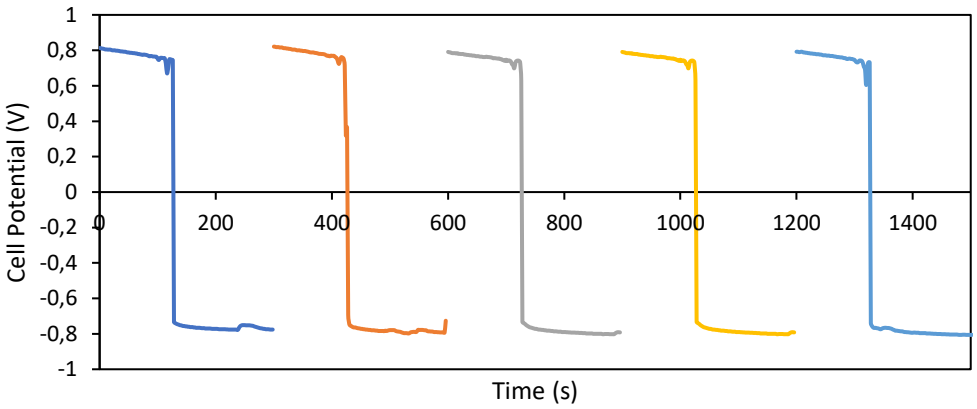

Figure D2 - Polarization curves for high loading MEA (1:1 Ir:Pt) in 5 min starvation and 10 min recovery AST

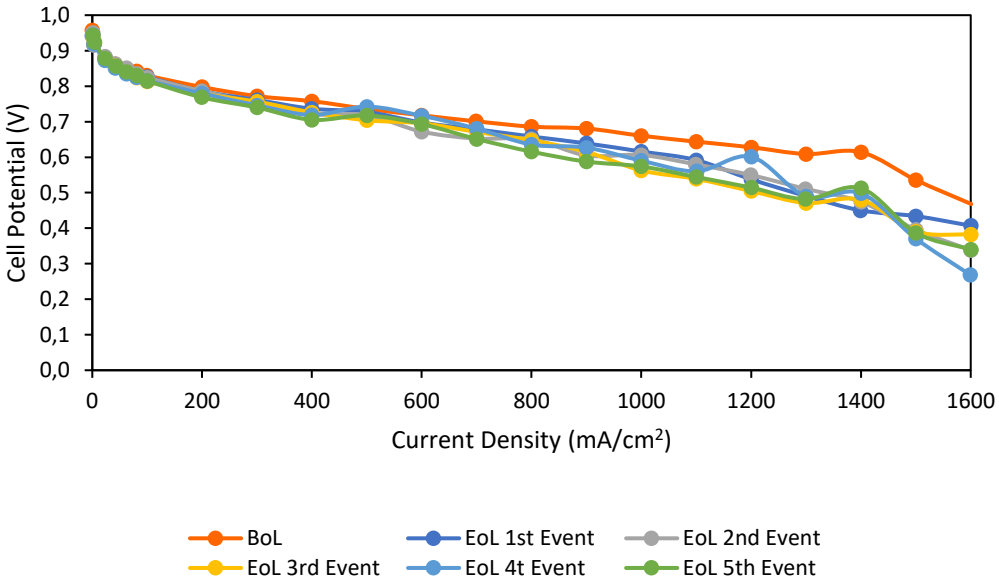

Table D1 – Evaluation of performance drop at 400 and 1200 mA after each RTA event relative to its BoL

	400 mA		**1200 mA**	
	Value	% drop	Value	% drop
BoL	0.758	-	0.628	-
1st event	0.737	2.8	0.538	14.3
2nd event	0.722	4.7	0.55	12.4
3rd event	0.726	4.2	0.505	19.6
4th event	0.719	5.1	0.601	4.3
5th event	0.705	7.0	0.514	18.2

Figure D3 - Voltage response for high loading MEA (1:1 Ir:Pt) in 5 min starvation and 30 min recovery AST

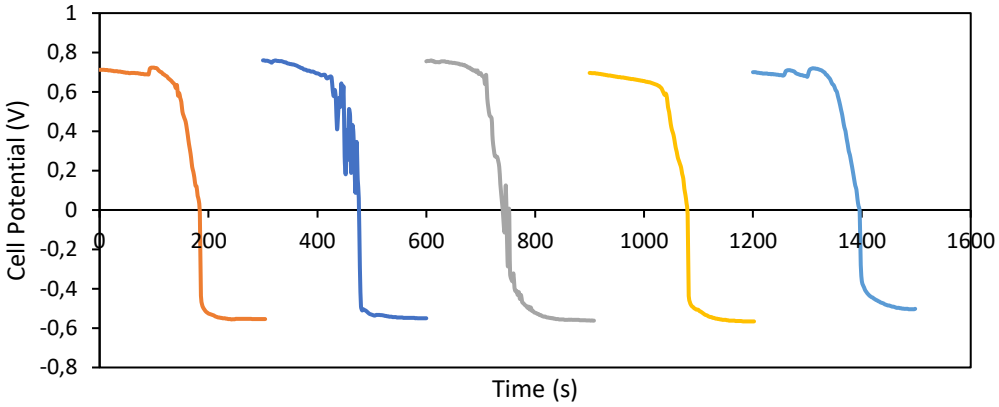

Figure D4 - Polarization curves for high loading MEA (1:1 Ir:Pt) in 5 min starvation and 30 min recovery AST

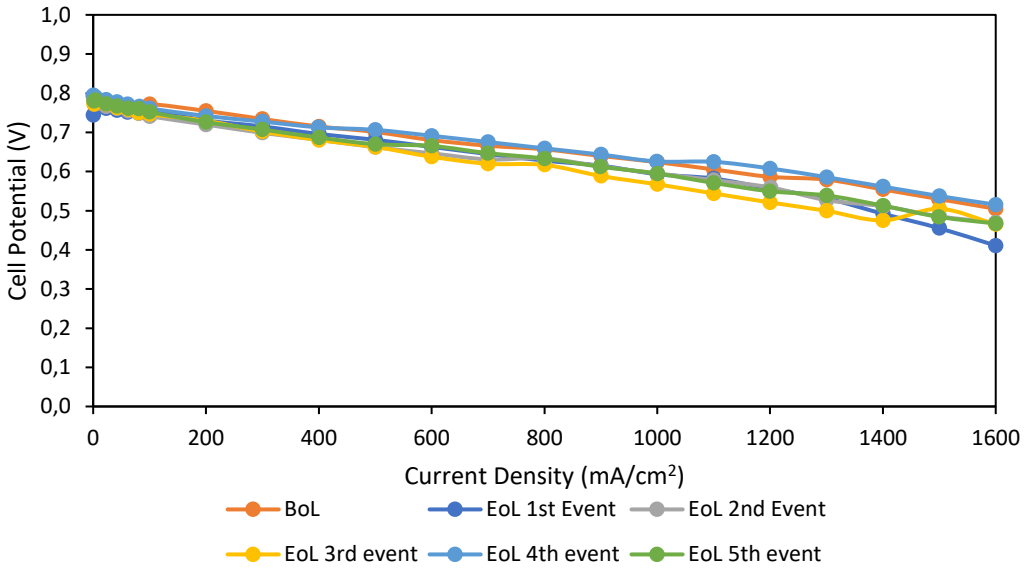

Table D2 – Evaluation of performance drop at 400 and 1200 mA after each RTA event relative to its BoL

	400 mA		1200 mA	
	Value	% drop	Value	% drop
BoL	0.71	-	0.602	-
1st event	0.696	2.0	0.556	7.6
2nd event	0.681	4.1	0.559	7.1
3rd event	0.68	4.2	0.521	13.5
4th event	0.713	-0.4	0.608	-1.0
5th event	0.687	3.2	0.55	8.6

Figure D5 - Voltage response for high loading MEA (1:1 Ir:Pt) in 10 min starvation and 10 min recovery AST

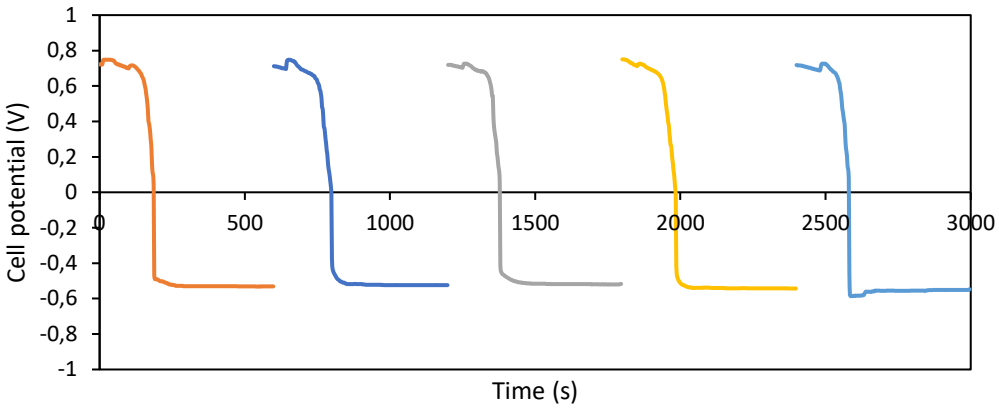

Figure D6 - Polarization curves for high loading MEA (1:1 Ir:Pt) in 10 min starvation and 10 min recovery AST

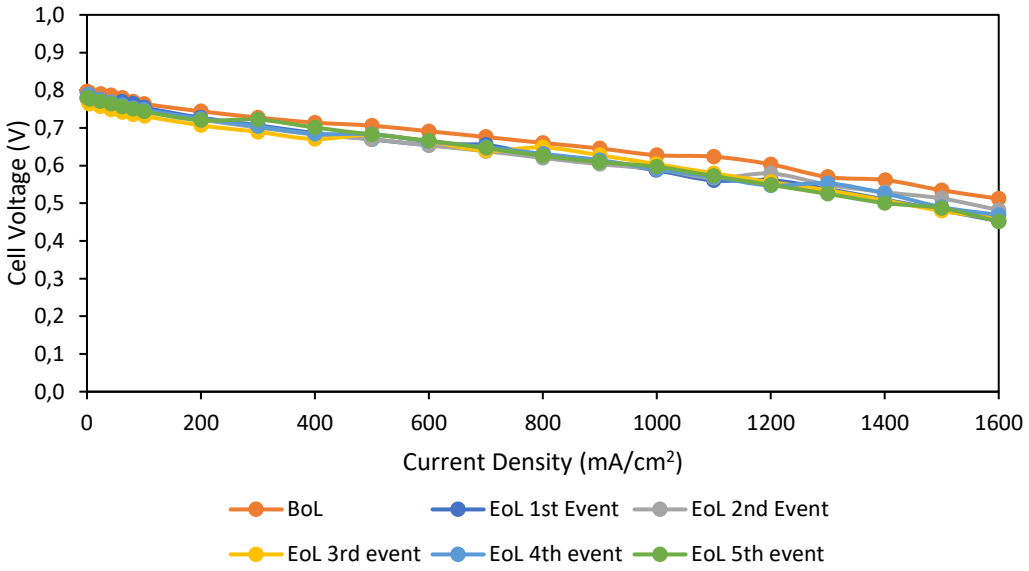

Table D3 – Evaluation of performance drop at 400 and 1200 mA after each RTA event relative to its BoL

	400 mA		1200 mA	
	Value	% drop	Value	% drop
BoL	0.7114	-	0.603	-
1st event	0.686	3.6	0.562	6.8
2nd event	0.682	4.1	0.579	4.0
3rd event	0.67	5.8	0.556	7.8
4th event	0.684	3.9	0.547	9.3
5th event	0.701	1.5	0.548	9.1

Figure D7 - Voltage response for high loading MEA (1:1 Ir:Pt) in 10 min starvation and 30 min recovery AST

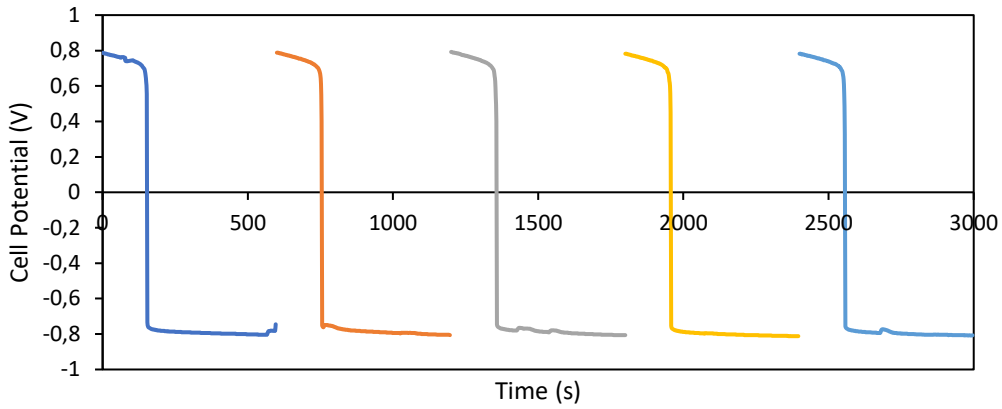

Figure D8 - Polarization curves for high loading MEA (1:1 Ir:Pt) in 10 min starvation and 30 min recovery AST

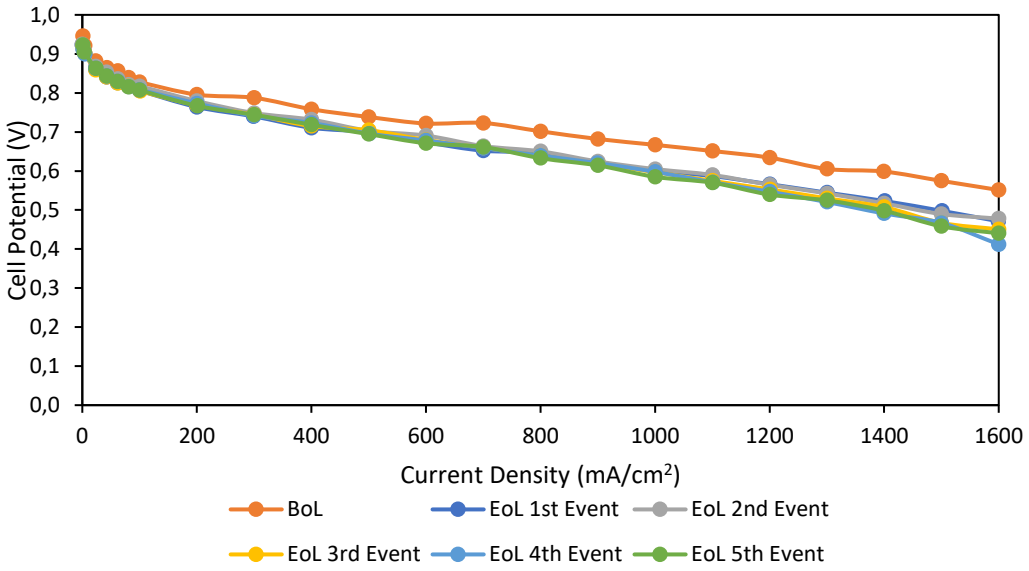

Table D4 – Evaluation of performance drop at 400 and 1200 mA after each RTA event relative to its BoL

	400 mA		1200 mA	
	Value	% drop	Value	% drop
BoL	0.758	-	0.634	-
1st event	0.711	6.2	0.566	10.7
2nd event	0.732	3.4	0.564	11.0
3rd event	0.715	5.7	0.553	12.8
4th event	0.723	4.6	0.547	13.7
5th event	0.718	5.3	0.539	15.0

Figure D9 - Voltage response for high loading MEA (1:1 Ir:Pt) in 30 min starvation and 10 min recovery AST

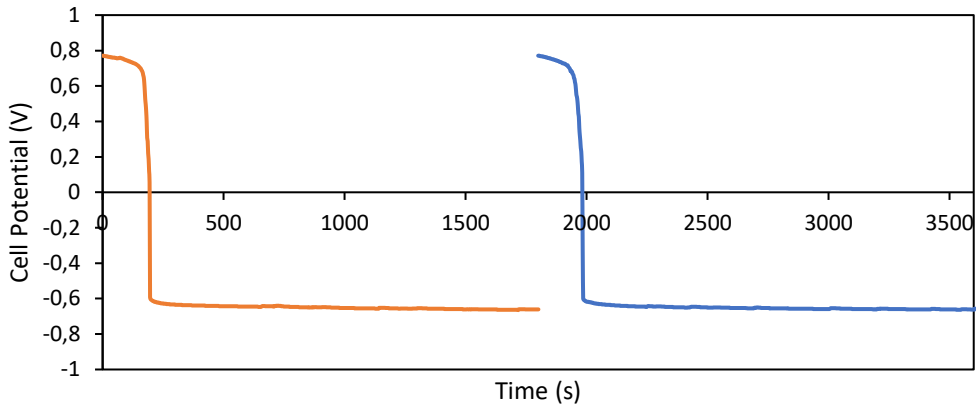

Figure D10 - Polarization curves for high loading MEA (1:1 Ir:Pt) in 30 min starvation and 10 min recovery AST

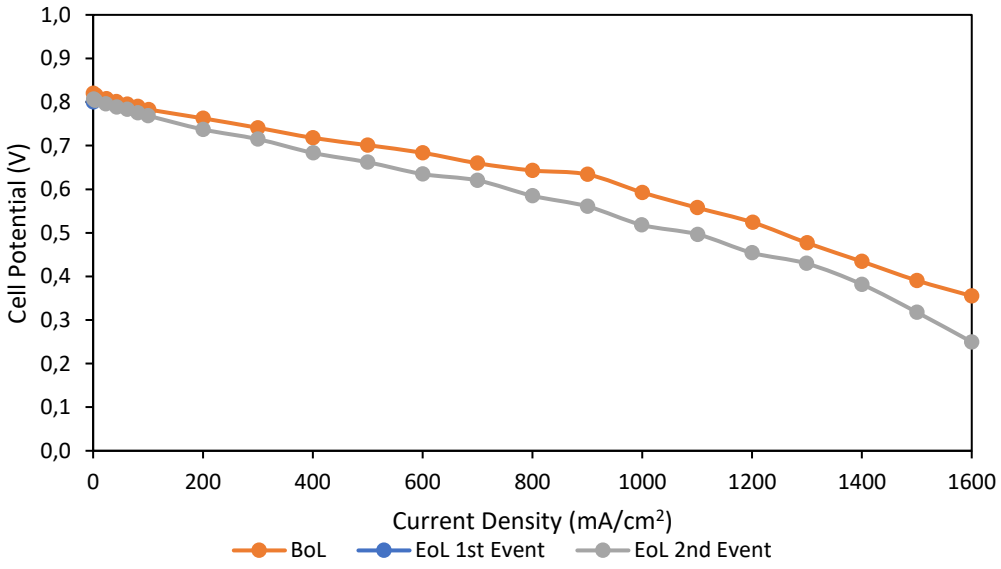

Table D5 – Evaluation of performance drop at 400 and 1200 mA after each RTA event relative to its BoL

	400 mA		1200 mA	
	Value	% drop	Value	% drop
BoL	0.718	-	0.524	-
1st event	-	-	-	-
2nd event	0.683	4.9	0.454	13.4

Figure D11 - Voltage response for high loading MEA (1:1 Ir:Pt) in 30 min starvation and 30 min recovery AST

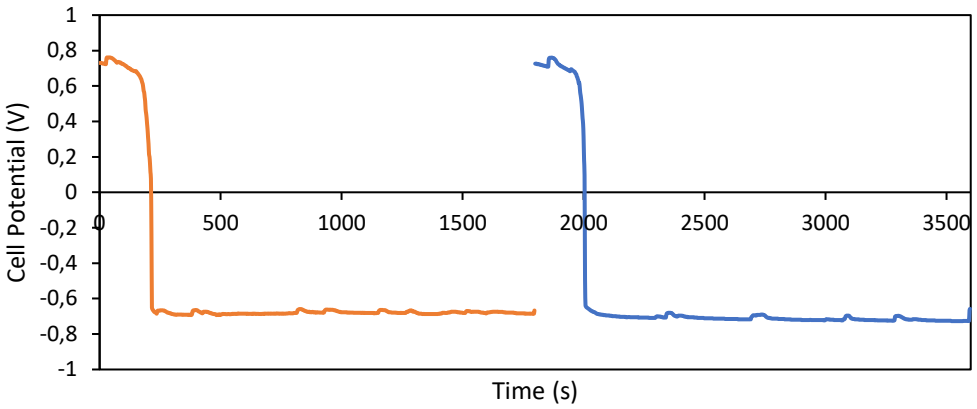

Figure D12 - Polarization curves for high loading MEA (1:1 Ir:Pt) in 30 min starvation and 30 min recovery AST

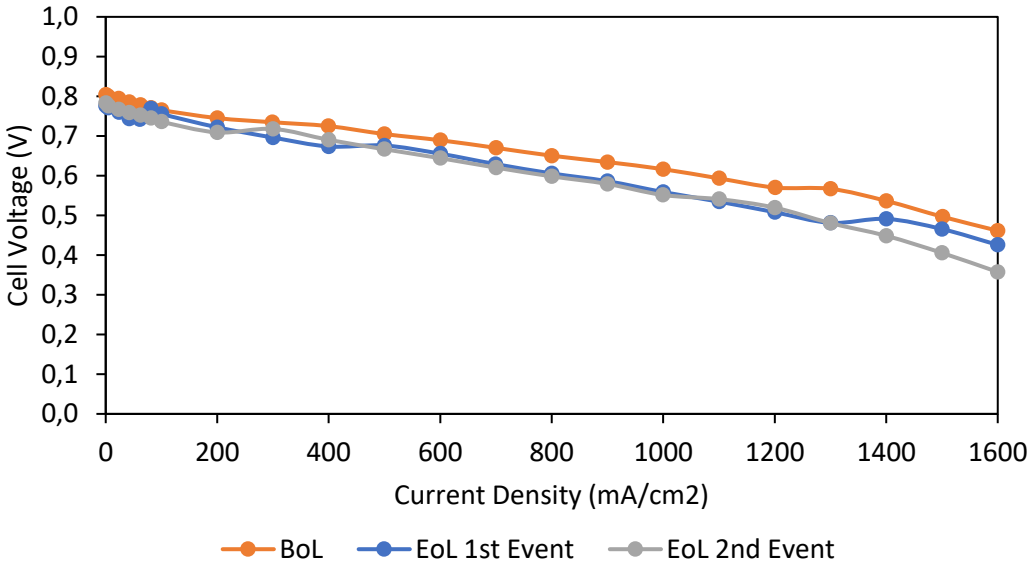

Table D6 – Evaluation of performance drop at 400 and 1200 mA after each RTA event relative to its BoL

	0.4 A		1.2 A	
	Value	% drop	Value	% drop
BoL	0.725	-	0.57	-
1st event	0.674	7.0	0.508	10.9
2nd event	0.69	4.8	0.52	8.8

Figure D13 - Voltage response for low loading MEA (0.6:1 Ir:Pt) in 5 min starvation and 10 min recovery AST

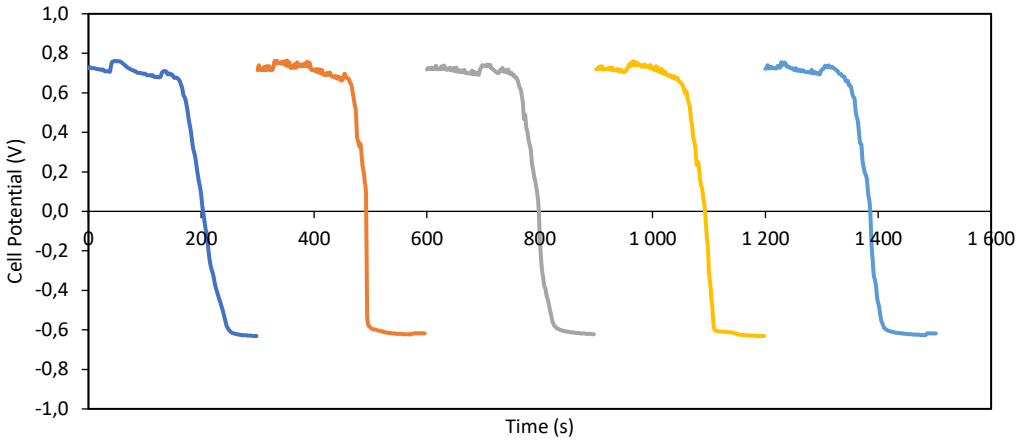

Figure D14 - Polarization curves for low loading MEA (0.6:1 Ir:Pt) in 5 min starvation and 10 min recovery AST

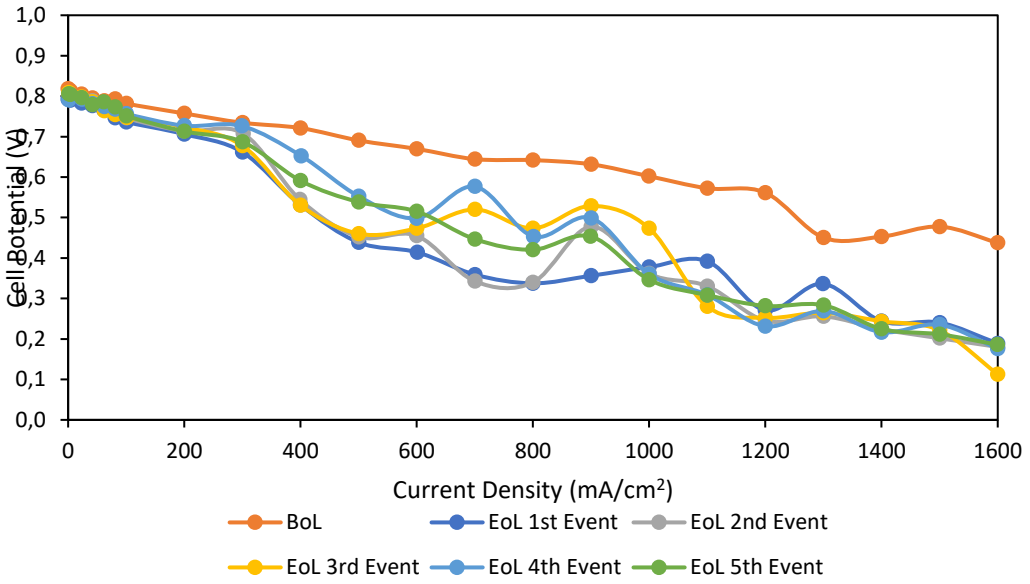

Table D7 – Evaluation of performance drop at 400 and 1200 mA after each RTA event relative to its BoL

	400 mA		1200 mA	
	Value	% drop	Value	% drop
BoL	0.721233	-	0.5616	-
1st event	0.531	26.4	0.271	51.8
2nd event	0.544	24.5	0.245	56.4
3rd event	0.531	26.4	0.252	55.1
4th event	0.653	9.5	0.231	58.8
5th event	0.591	18.0	0.282	49.9

Figure D15 - Voltage response for low loading MEA (0.6:1 Ir:Pt) in 5 min starvation and 30 min recovery AST

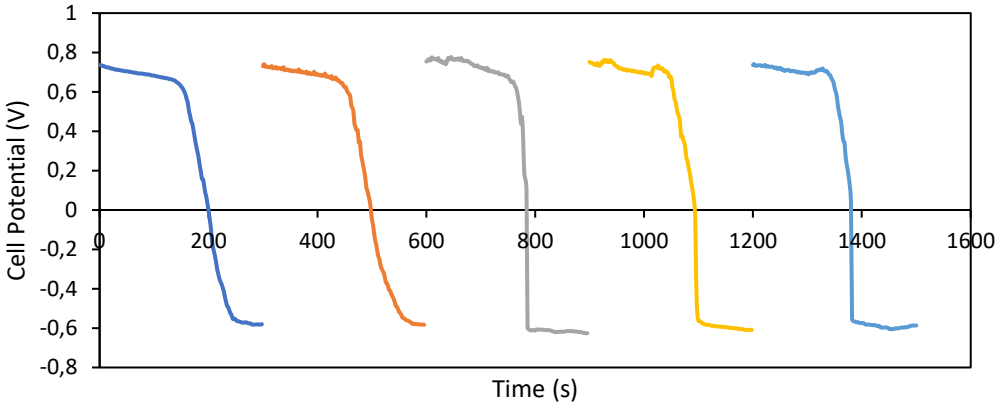

Figure D16 - Polarization curves for low loading MEA (0.6:1 Ir:Pt) in 5 min starvation and 30 min recovery AST

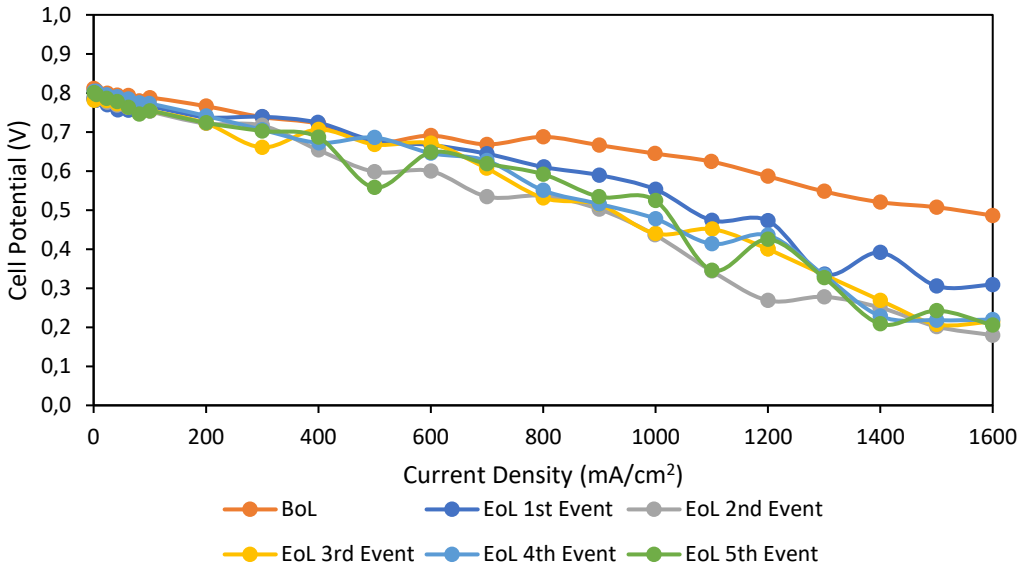

Table D8 – Evaluation of performance drop at 400 and 1200 mA after each RTA event relative to its BoL

	400 mA		1200 mA	
	Value	% drop	Value	% drop
BoL	0.721	-	0.587	-
1st event	0.724	-0.4	0.473	19.4
2nd event	0.654	9.3	0.269	54.2
3rd event	0.706	2.1	0.4	31.9
4th event	0.672	6.8	0.436	25.7
5th event	0.686	4.9	0.425	27.6

Figure D17 - Voltage response for low loading MEA (0.6:1 Ir:Pt) in 10 min starvation and 10 min recovery AST

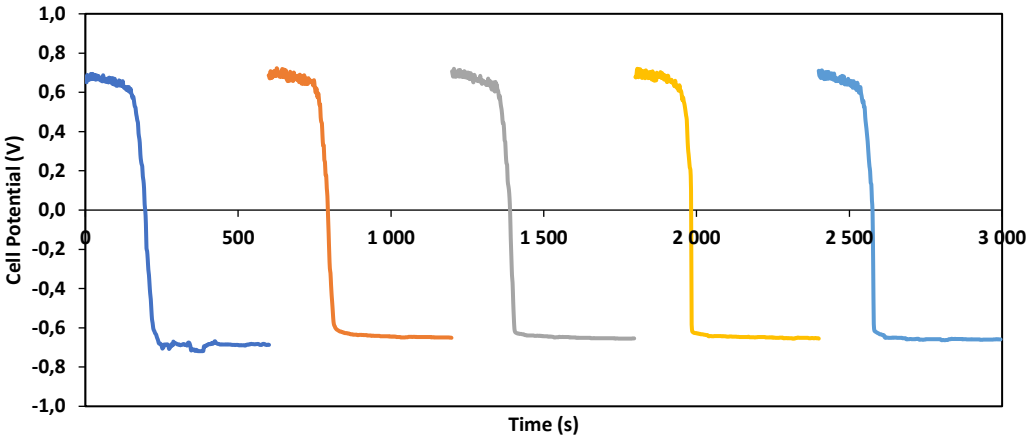

Figure D18 - Polarization curves for low loading MEA (0.6:1 Ir:Pt) in 10 min starvation and 10 min recovery AST

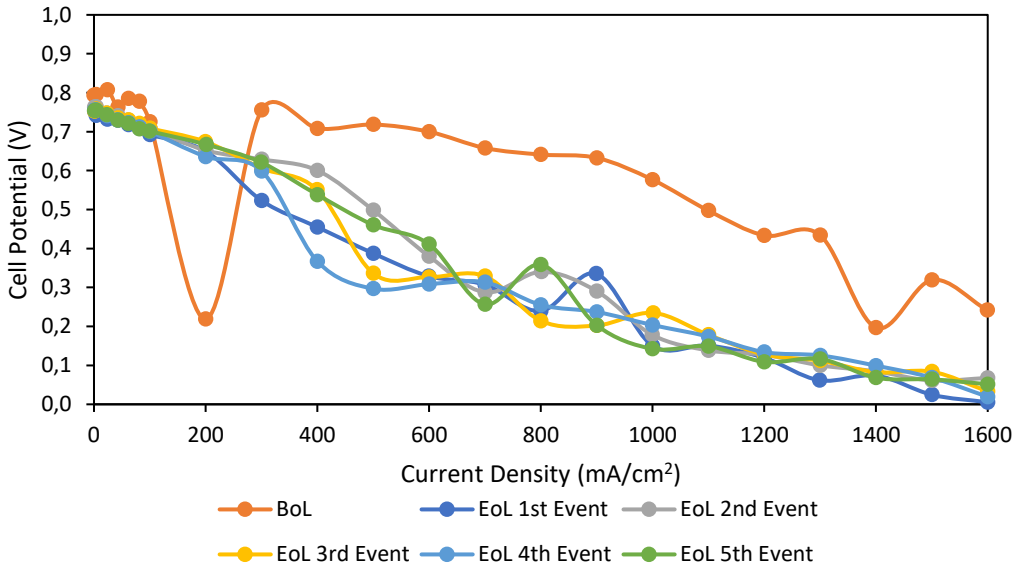

Table D9 – Evaluation of performance drop at 400 and 1200 mA after each RTA event relative to its BoL

	400 mA		1200 mA	
	Value	% drop	Value	% drop
BoL	0.708167	-	0.4335	-
1st event	0.455	35.8	0.119	72.5
2nd event	0.600	15.2	0.127	70.6
3rd event	0.551	22.2	0.128	70.5
4th event	0.367	48.2	0.134	69.1
5th event	0.538	24.0	0.109	74.9

Figure D19 - Voltage response for low loading MEA (0.6:1 Ir:Pt) in 10 min starvation and 30 min recovery AST

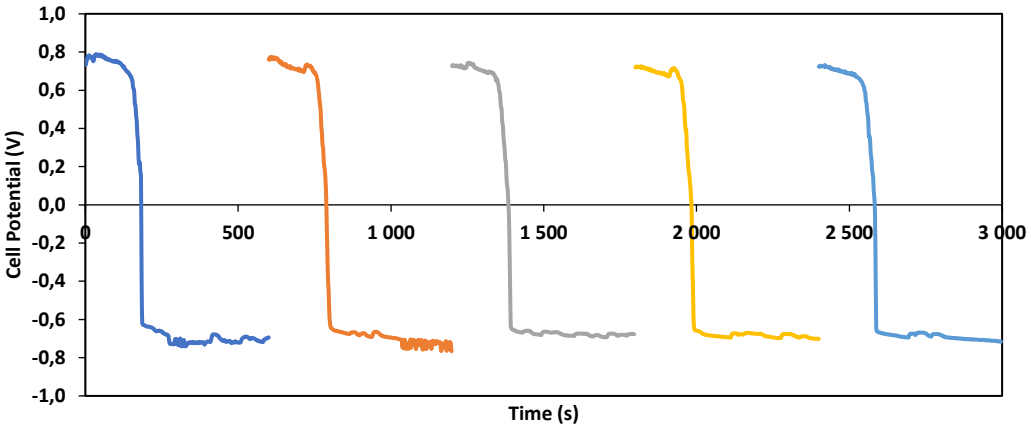

Figure D20 - Polarization curves for low loading MEA (0.6:1 Ir:Pt) in 10 min starvation and 30 min recovery AST

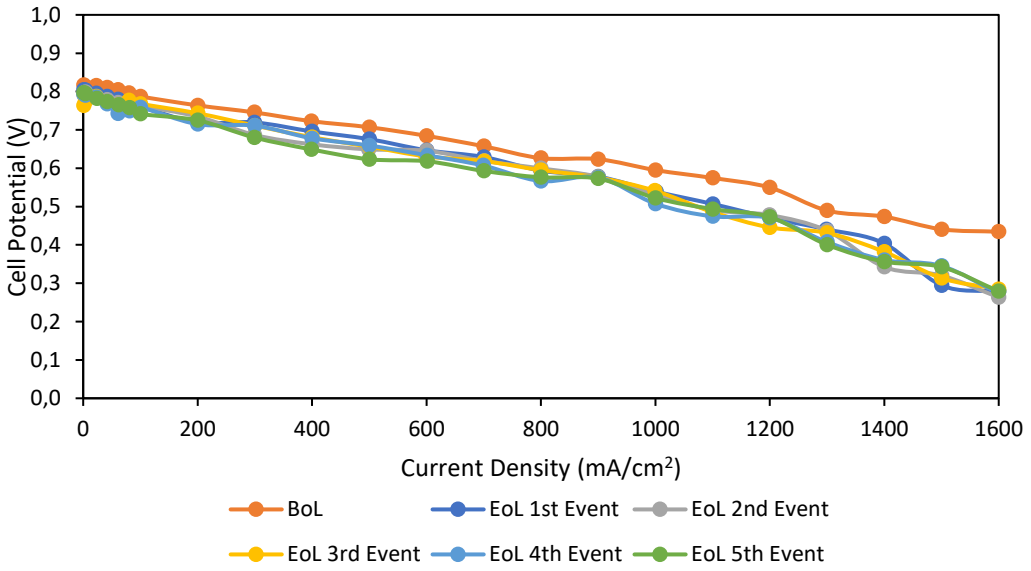

Table D10 – Evaluation of performance drop at 400 and 1200 mA after each RTA event relative to its BoL

	400 mA		1200 mA	
	Value	% drop	Value	% drop
BoL	0.7227	-	0.5495	-
1st event	0.696	3.7	0.471	14.3
2nd event	0.662	8.3	0.478	13.0
3rd event	0.681	5.8	0.446	18.9
4th event	0.678	6.2	0.470	14.4
5th event	0.649	10.2	0.473	14.0

Figure D21 - Voltage response for low loading MEA (0.6:1 Ir:Pt) in 30 min starvation and 10 min recovery AST

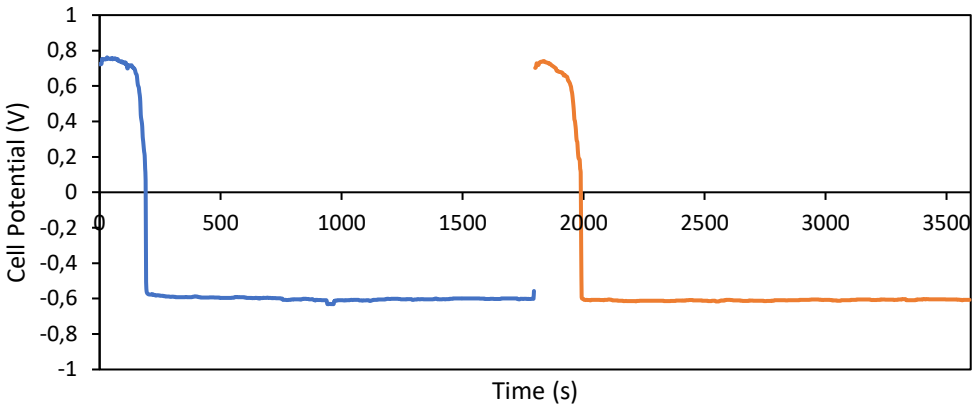

Figure D22 - Polarization curves for low loading MEA (0.6:1 Ir:Pt) in 30 min starvation and 10 min recovery AST

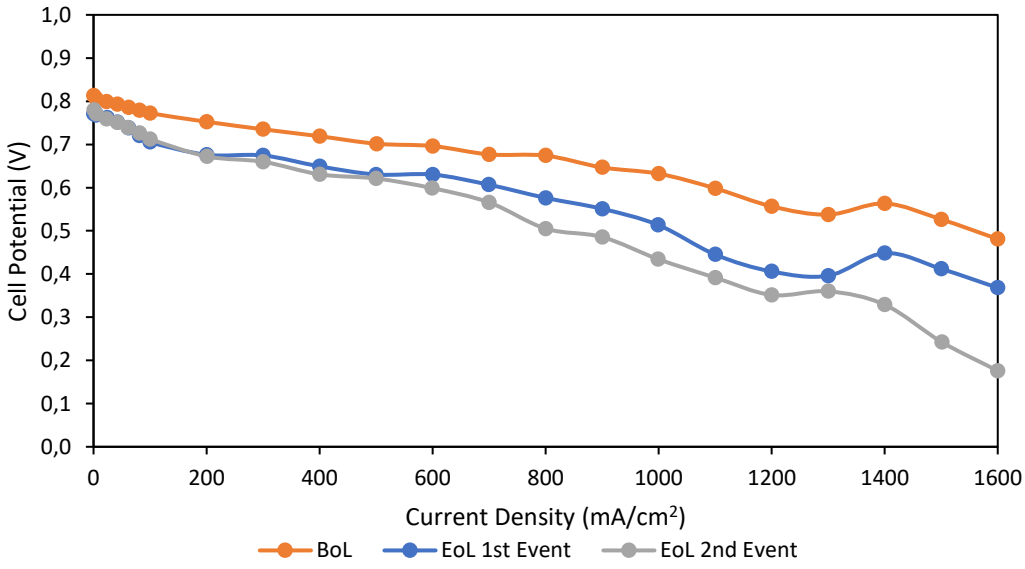

Table D11 – Evaluation of performance drop at 400 and 1200 mA after each RTA event relative to its BoL

	400 mA		1200 mA	
	Value	% drop	Value	% drop
BoL	0.719	-	0.557	-
1st event	0.649	9.7	0.406	27.1
2nd event	0.631	12.2	0.351	37.0

Figure D23 - Voltage response for low loading MEA (0.6:1 Ir:Pt) in 30 min starvation and 30 min recovery AST

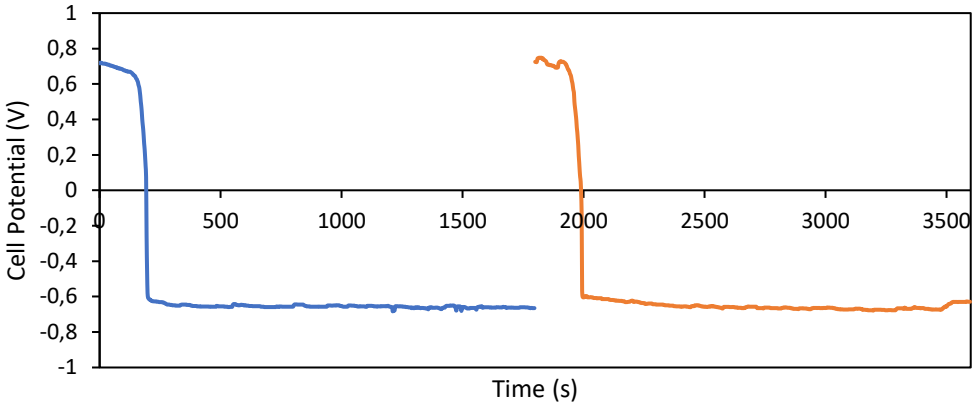

Figure D24 - Polarization curves for low loading MEA (0.6:1 Ir:Pt) in 30 min starvation and 30 min recovery AST

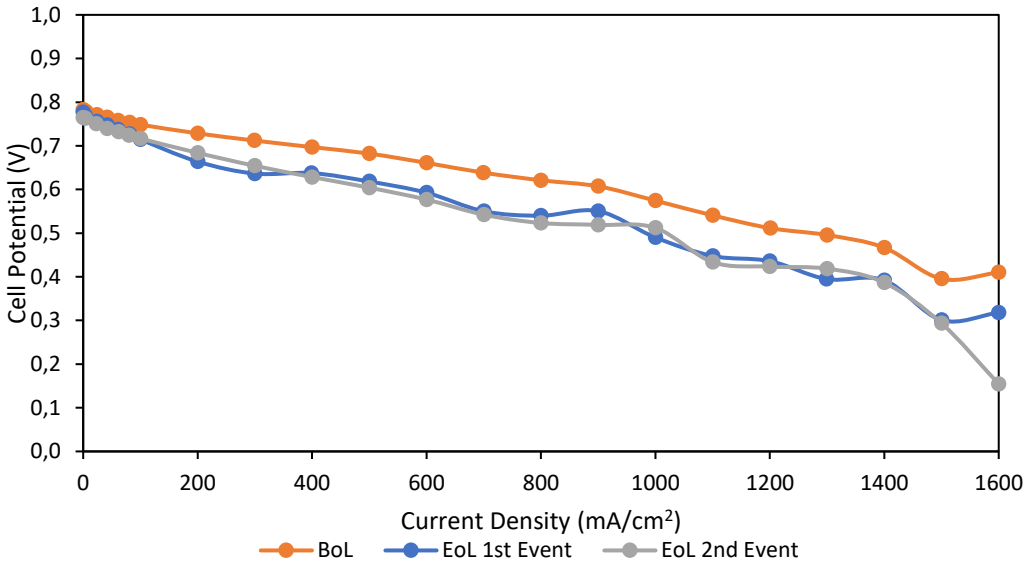

Table D12 – Evaluation of performance drop at 400 and 1200 mA after each RTA event relative to its BoL

	400 mA		1200 mA	
	Value	% drop	Value	% drop
BoL	0.697	-	0.511	-
1st event	0.638	8.5	0.436	14.7
2nd event	0.628	9.9	0.423	17.2

8.5. Appendix E: Fitted XPS spectra of MEAs before and after ASTs

Ir Fittings

Figure E1 - XPS fitting of Ir 4f spectra on anode side of MEA after conditioning.

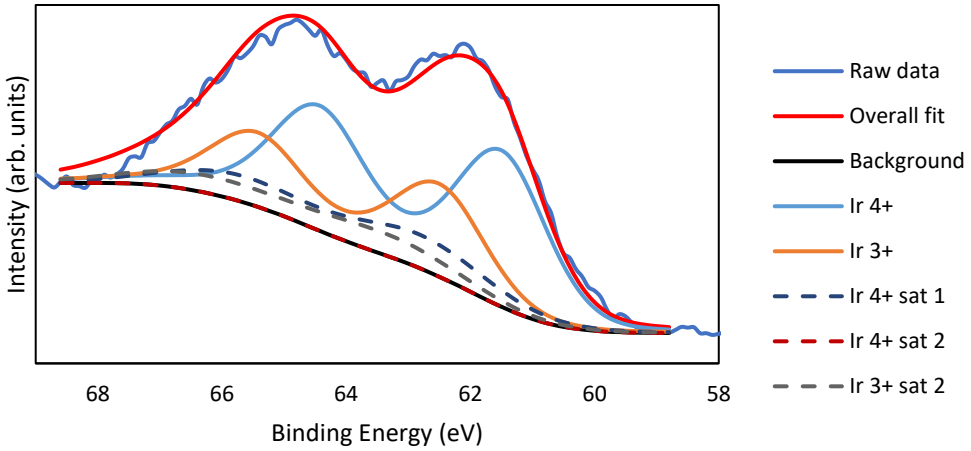

Figure E2 - XPS fitting of Ir 4f spectra on anode side of MEA after 30 min potential reversal AST.

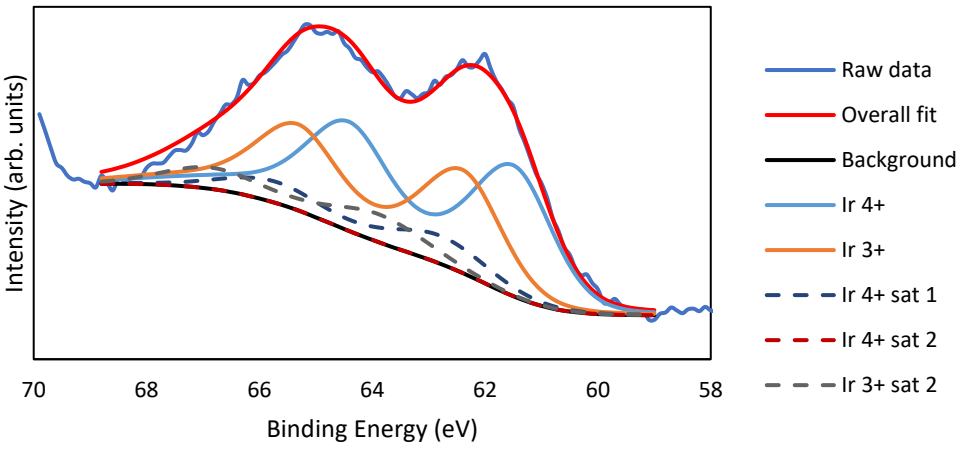

Figure E3 - XPS fitting of Ir 4f spectra on anode side of MEA after long hold AST.

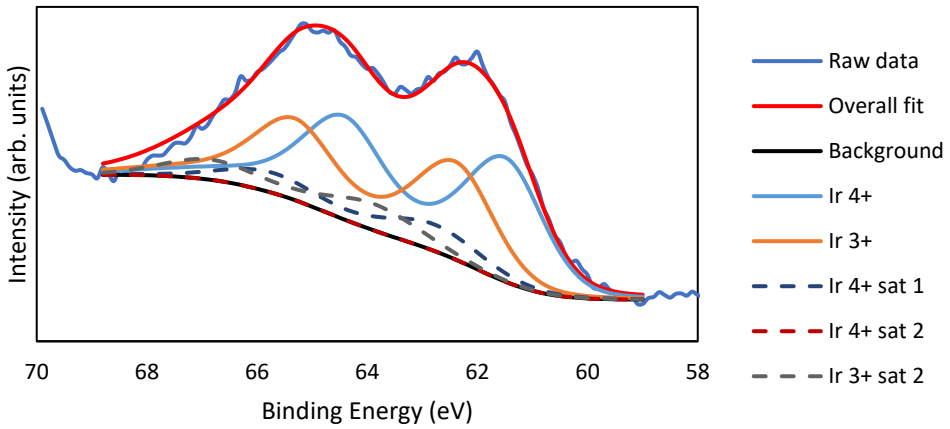

Pt Fittings

Figure E4 - XPS fitting of Pt 4f spectra on anode side of MEA after conditioning.

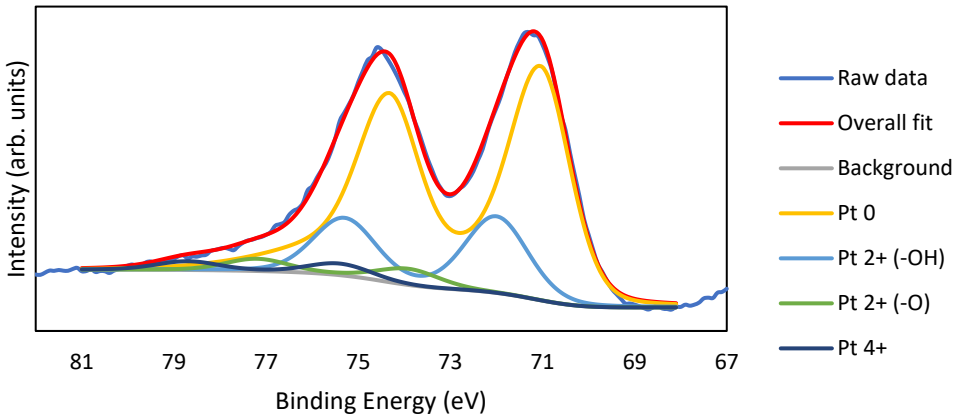

Figure E5 - XPS fitting of Pt 4f spectra on anode side of MEA after 30 min potential reversal AST.

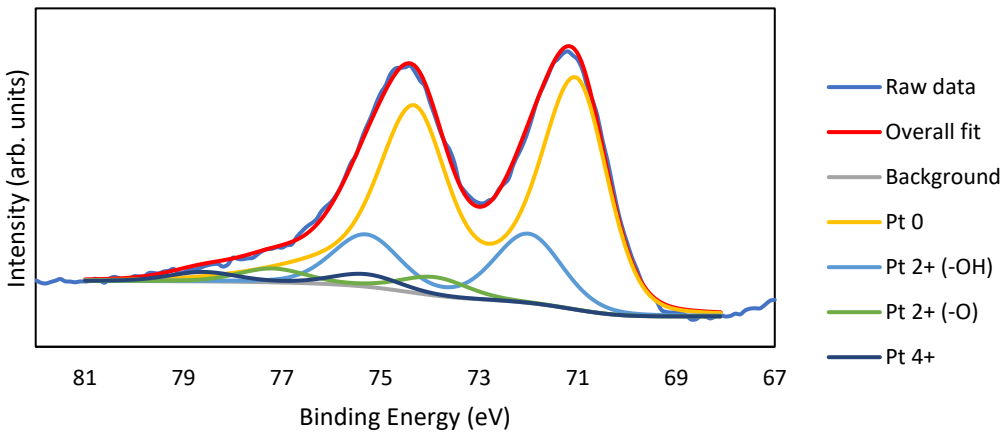

Figure E6 - XPS fitting of Pt 4f spectra on anode side of MEA after long hold AST.

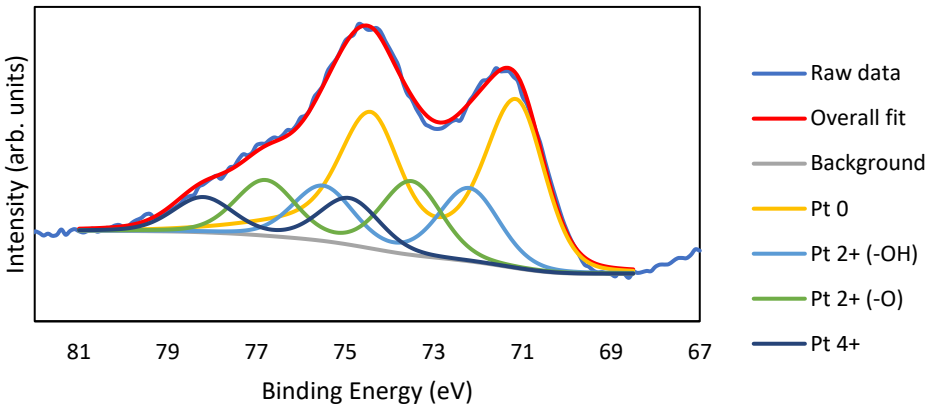

Figure E7 - XPS fitting of Pt 4f spectra on cathode side of MEA after conditioning.

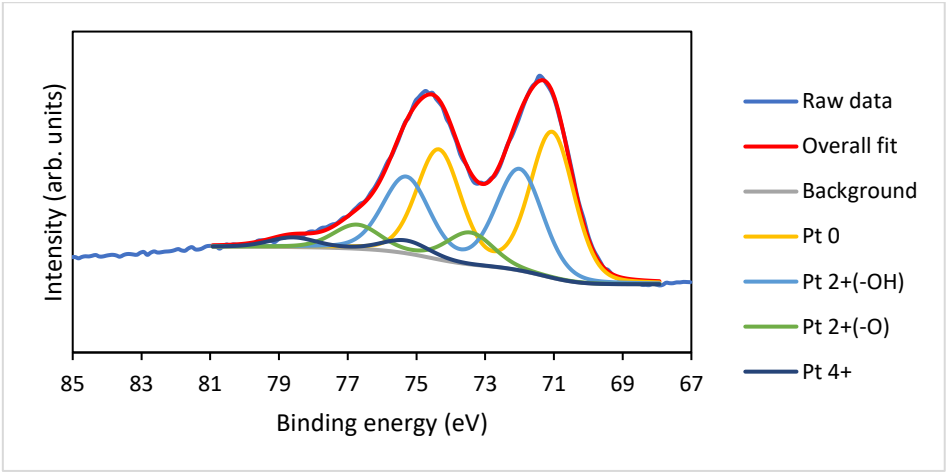

Figure E8 - XPS fitting of Pt 4f spectra on cathode side of MEA after 30 min potential reversal AST.

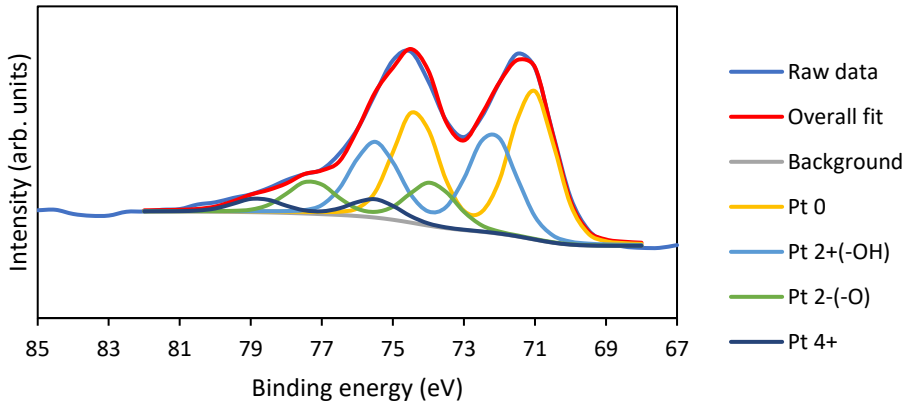

Figure E9 - XPS fitting of Pt 4f spectra on cathode side of MEA after long hold AST.